

ISSN 2071-4726
2071-0305

Инженерно-строительный журнал

НАУЧНОЕ ИЗДАНИЕ

№4(88) 2019





ПОЛИТЕХ
Санкт-Петербургский
политехнический университет
Петра Великого

Инженерно-строительный институт
Центр дополнительных профессиональных программ
195251, г. Санкт-Петербург, Политехническая ул., 29,
тел/факс: 552-94-60, www.stroikursi.spbstu.ru,
stroikursi@mail.ru

**Приглашает специалистов организаций, вступающих в СРО,
на курсы повышения квалификации (72 часа)**

| Код | Наименование программы | Виды работ* |
|---------------------------------------|--|--|
| Курсы по строительству | | |
| БС-01-04 | «Безопасность и качество выполнения общестроительных работ» | п.1,2, 3, 5, 6, 7, 9, 10, 11, 12, 13, 14 |
| БС-01 | «Безопасность и качество выполнения геодезических, подготовительных и земляных работ, устройства оснований и фундаментов» | 1,2,3,5 |
| БС-02 | «Безопасность и качество возведения бетонных и железобетонных конструкций» | 6,7 |
| БС-03 | «Безопасность и качество возведения металлических, каменных и деревянных конструкций» | 9,10,11 |
| БС-04 | «Безопасность и качество выполнения фасадных работ, устройства кровель, защиты строительных конструкций, трубопроводов и оборудования» | 12,13,14 |
| БС-05 | «Безопасность и качество устройства инженерных сетей и систем» | 15,16,17,18,19 |
| БС-06 | «Безопасность и качество устройства электрических сетей и линий связи» | 20,21 |
| БС-08 | «Безопасность и качество выполнения монтажных и пусконаладочных работ» | 23,24 |
| БС-12 | «Безопасность и качество устройства мостов, эстакад и путепроводов» | 29 |
| БС-13 | «Безопасность и качество выполнения гидротехнических, водолазных работ» | 30 |
| БС-14 | «Безопасность и качество устройства промышленных печей и дымовых труб» | 31 |
| БС-15 | «Осуществление строительного контроля» | 32 |
| БС-16 | «Организация строительства, реконструкции и капитального ремонта. Выполнение функций технического заказчика и генерального подрядчика» | 33 |
| Курсы по проектированию | | |
| БП-01 | «Разработка схемы планировочной организации земельного участка, архитектурных решений, мероприятий по обеспечению доступа маломобильных групп населения» | 1,2,11 |
| БП-02 | «Разработка конструктивных и объемно-планировочных решений зданий и сооружений» | 3 |
| БП-03 | «Проектирование внутренних сетей инженерно-технического обеспечения» | 4 |
| БП-04 | «Проектирование наружных сетей инженерно-технического обеспечения» | 5 |
| БП-05 | «Разработка технологических решений при проектировании зданий и сооружений» | 6 |
| БП-06 | «Разработка специальных разделов проектной документации» | 7 |
| БП-07 | «Разработка проектов организации строительства» | 8 |
| БП-08 | «Проектные решения по охране окружающей среды» | 9 |
| БП-09 | «Проектные решения по обеспечению пожарной безопасности» | 10 |
| БП-10 | «Обследование строительных конструкций и грунтов основания зданий и сооружений» | 12 |
| БП-11 | «Организация проектных работ. Выполнение функций генерального проектировщика» | 13 |
| Э-01 | «Проведение энергетических обследований с целью повышения энергетической эффективности и энергосбережения» | |
| Курсы по инженерным изысканиям | | |
| И-01 | «Инженерно-геодезические изыскания в строительстве» | 1 |
| И-02 | «Инженерно-геологические изыскания в строительстве» | 2,5 |
| И-03 | «Инженерно-гидрометеорологические изыскания в строительстве» | 3 |
| И-04 | «Инженерно-экологические изыскания в строительстве» | 4 |
| И-05 | «Организация работ по инженерным изысканиям» | 7 |

*(согласно приказам Минрегионразвития РФ N 624 от 30 декабря 2009 г.)

**По окончании курса слушателю выдается удостоверение о краткосрочном повышении
квалификации установленного образца (72 ак. часа)**

Для регистрации на курс необходимо выслать заявку на участие, и копию диплома об образовании по телефону/факсу: 8(812) 552-94-60, 535-79-92, , e-mail: stroikursi@mail.ru.

Инженерно-строительный журнал

НАУЧНОЕ ИЗДАНИЕ

ISSN 2071-4726, 2071-0305

Свидетельство о государственной регистрации: ПИ №ФС77-38070, выдано Роскомнадзором

Специализированный научный журнал. Выходит с 09.2008.

Включен в Перечень ведущих периодических изданий ВАК РФ

Периодичность: 8 раз в год

Учредитель и издатель:

Санкт-Петербургский политехнический университет Петра Великого

Адрес редакции:

195251, СПб, ул. Политехническая, д. 29, Гидрокорпус-2, ауд. 245

Главный редактор:

Екатерина Александровна Линник

Научный редактор:

Николай Иванович Ватин

Выпускающий редактор:

Анастасия Крупина

Редакционная коллегия:

д.ф.-м.н., доцент Р.А. Абдикаримов;
 д.т.н., проф. В.В. Бабков;
 к.т.н., проф. А.И. Боровков;
 д.т.н., проф. Н.И. Ватин;
 PhD, проф. М. Вельжкович;
 к.т.н., М.Р. Гарифуллин;
 д.т.н., проф. Э.К. Завадскас;
 д.ф.-м.н., проф. М.Н. Кирсанов;
 D.Sc., проф. М. Кнежевич;
 д.т.н., проф. В.В. Лалин;
 д.т.н., проф. Б.Е. Мельников;
 д.т.н., академик М.М. Мирсаидов;
 д.т.н., проф. Ф. Неправишта;
 д.т.н., проф. Р.Б. Орлович;
 Dr. Sc. Ing., professor
 Л. Пакрастиньш;
 Dr.-Ing. Habil., professor
 X. Пастернак;
 д.т.н., проф. А.В. Перельмутер;
 д.т.н., проф. М.Р. Петриченко;
 д.т.н., проф. В.В. Сергеев;
 д.ф.-м.н., проф. М.Х. Стрелец;
 д.т.н., проф. О.В. Тараканов;
 д.т.н., проф. Б.Б. Телтаев;
 д.т.н., проф. В.И. Травуш;
 д.т.н., проф. Д. Унгерман;
 д.т.н., проф. С.В. Федосов

Дата выхода: 18.07.2019

Содержание

| | |
|--|----|
| Ле Т., Лалин В.В., Браташов А.А. Статический учет высших мод колебаний в задачах динамики конструкций | 3 |
| Шахов С.А., Рогова Е.В. Факторы, влияющие на ультразвуковую дезагрегацию порошков | 14 |
| Логанина В.И., Петухова Н.А., Федюк Р.С., Тимохин Р.А. Полистирольная краска с пониженным содержанием летучих соединений | 25 |
| Соловьев С.Ю., Храпунов Е.Ф. Моделирование средних ветровых нагрузок на сооружения | 42 |
| Чжао Ц., Чен П., Вей Ю., Ван Д. Факторы, влияющие на процесс восстановления самовосстанавливающегося бетона | 52 |
| Колчунов В.И., Демьянов А.И. Неординарная задача о раскрытии трещин в железобетоне | 60 |
| Нгуен Ч.Ч., Лыу С.Б. Уменьшение разницы температур в монолитном бетоне за счет поверхностной изоляции | 70 |

© ФГАОУ ВО СПбПУ, 2019

© Иллюстрация на обложке: Илья Смагин

Контакты:E-mail: mce@spbstu.ruWeb: <http://www.engstroy.spbstu.ru>

Magazine of Civil Engineering

SCHOLAR JOURNAL

ISSN 2071-4726, 2071-0305

Peer-reviewed scientific journal

Start date: 2008/09

8 issues per year

Publisher:Peter the Great St. Petersburg
Polytechnic University**Indexing:**Scopus, Russian Science Citation
Index (WoS), Compendex, DOAJ,
EBSCO, Google Academia, Index
Copernicus, ProQuest, Ulrich's Serials
Analysis System**Corresponding address:**245 Hydro Building, 29
Polytechnicheskaya st., Saint-
Petersburg, 195251, Russia**Editor-in-chief:**

Ekaterina A. Linnik

Science editor:

Nikolay I. Vatin

Technical editor:

Anastasia Krupina

Editorial board:R.A. Abdikarimov, D.Sc., associate
professor

V.V. Babkov, D.Sc., professor

A.I. Borovkov, PhD, professor

M. Veljkovic, PhD, professor

M. Garifullin, PhD, postdoctorant

E.K. Zavadskas, D.Sc., professor

M.N. Kirsanov, D.Sc., professor

M. Knezevic, D.Sc., professor

V.V. Lalin, D.Sc., professor

B.E. Melnikov, D.Sc., professor

M.M. Mirsaidov, D.Sc., professor

F. Nepravishhta, D.Sc., professor

R.B. Orlovich, D.Sc., professor

L. Pakrastinsh, Dr.Sc.Ing., professor

H. Pasternak, Dr.-Ing.habil.,
professor

A.V. Perelmuter, D.Sc., professor

M.R. Petrichenko, D.Sc., professor

V.V. Sergeev, D.Sc., professor

M.Kh. Strelets, D.Sc., professor

O.V. Tarakanov, D.Sc., professor

B.B. Teltayev, D.Sc., professor

V.I. Travush, D.Sc., professor

S.V. Fedosov, D.Sc., professor

Date of issue: 18.07.2019

Contents

| | |
|---|----|
| Le, T.Q.T, Lalin, V.V., Bratashov, A.A. Static accounting of highest modes in problems of structural dynamics | 3 |
| Shakhov, S.A., Rogova, E.V. Factors affecting the ultrasonic disaggregation of powders | 14 |
| Loganina, V.I., Petukhova, N.A., Fediuk, R.S., Timokhin, R.A. Polystyrene paint with reduced contents of volatile compounds | 25 |
| Solovev, S.Yu., Khrapunov, E.F. Modeling of the mean wind loads on structures | 42 |
| Zhao, Q., Cheng, P., Wei, Y., Wang, J. Factors effecting the recovery process of self-repairing concrete | 52 |
| Kolchunov, V.I., Dem'yanov, A.I. The modeling method of discrete cracks and rigidity in reinforced concrete | 60 |
| Nguyen, T.C., Luu, X.B. Reducing temperature difference in mass concrete by surface insulation | 70 |

© Peter the Great St. Petersburg Polytechnic University. All rights reserved.

© Illustration – Ilya Smagin

E-mail: mce@spbstu.ruWeb: <http://www.engstroy.spbstu.ru/eng/index.html>



DOI: 10.18720/MCE.88.1

Static accounting of highest modes in problems of structural dynamics

T.Q.T Le*, V.V. Lalin, A.A. Bratashov

Peter the Great St. Petersburg Polytechnic University, St. Petersburg, Russia

* E-mail: quangtrung1690@gmail.com

Keywords: structural dynamics, spectral method, vibration modes, highest modes, static accounting, spatial structures

Abstract. The calculation of building structures for dynamic effects is usually performed according to the method of decomposition by its own forms of vibrations. However, the problem is that such a method gives an exact solution of the dynamic problem with full consideration of the entire spectrum of modes. Moreover, when solving practical problems with the use of software systems, dynamic calculations are performed approximately taking into account a limited number of the first natural modes of oscillation. The contribution to the dynamic response of the structure of unaccounted higher forms of oscillations, as a rule, is not evaluated at all. The results show that the error of such a solution to a dynamic problem can be significant. Consequently, this paper is devoted to the method of static registration of higher forms of oscillations in problems of the dynamics of building structures. The description of the main provisions of the method is given, examples of its implementation in the calculation of spatial structures under the action of an external harmonic load are given. With the help of a computational program complex, the displacements of nodes and internal forces in the elements of the structures under consideration are determined. Various parameters of the dynamic effect and the number of vibration modes taken into account were set. The adopted method of static accounting for higher forms of oscillations requires solving one dynamic problem and two auxiliary static problems. An important circumstance of the approach is that one of the static problems should be solved by the method of decomposition in its own forms of vibrations. The approach proposed in the article allows to significantly reduce the computational costs of dynamic calculation in comparison with the classical approach. This result can be of great importance when solving problems for complex dynamic effects and for structures that are not uniform in hardness.

1. Introduction

Buildings and structures in the process of their construction and operation are affected by various dynamic loading, such as wind load, earthquake, operation of process equipment, impact loads, emergency destruction of a structural element, and so on. Many studies are devoted to the development of constructive solutions for buildings and their elements, methods for calculating under the dynamic loads [1–15]. It depends on the reasons, that led to the oscillations of the structure, its work can be viewed as a superposition of oscillations according to its modes [16–24]. Traditionally, in the dynamic calculation of building structures, only the first few modes of natural oscillations are taken into account, since the contribution of precisely these terms to displacements and internal efforts is the main one. It is rather difficult to take into account the other modes, since the resources of computing devices are limited, and there is no need to include in the calculation higher modes with low energy value. This fact is confirmed by large in number (numerous) studies, for example, in the works [25–28].

However, in some cases, the calculation of buildings and structures on the dynamic load may require consideration of the contribution of higher modes of oscillations. The need for this may arise, for example, when calculating a structure for seismic load [29–34]. In these books are considered the applied and prospective approaches to the calculation of dynamic interaction, the basic principles of seismic design and key aspects of calculations. In the article [35], a study of the vibrations of a building structure was carried out

Le, T.Q.T, Lalin, V.V., Bratashov, A.A. Static accounting of highest modes in problems of structural dynamics. Magazine of Civil Engineering. 2019. 88(4'). Pp. 3–13. DOI: 10.18720/MCE.88.1.

Ле Т., Лалин В.В., Браташов А.А. Статический учет высших мод колебаний в задачах динамики конструкций // Инженерно-строительный журнал. 2019. № 4(88). С. 3–13. DOI: 10.18720/MCE.88.1.



This open access article is licensed under CC BY 4.0 (<https://creativecommons.org/licenses/by/4.0/>)

and it was concluded that, as the frequency increases, the more rigid and (or) less significant parts of the system will be included in the oscillatory process corresponding to highest modes, while some parts of the structure can be excluded from movement. All these facts lead to the destruction of the elements and, as a result, of the whole system.

In the conditions of a real design process, when continuous changes are made to the project, editing the design scheme and recalculating it can take a significant amount of time and resources. Therefore, there are important and topical questions to reduce the number of modes taken into account in the calculation without losing accuracy of the result, as well as the contribution of the discarded modes to the local high-frequency oscillations of individual elements. Thus, the work [36] is devoted to the analysis of the accuracy of determining the response of a structure to a dynamic effect when taking into account a limited number of modes.

In the article [37], a concept was entered, according to which it is proposed to add an estimate of the total response for all high-frequency modes, determined from a static load, to the standard dynamic calculation. It is noted that with an increase in the number of modes taken into account, the convergence of the result in efforts is lower than in displacements, therefore the inclusion of highest modes can significantly affect local efforts.

The question of estimating the contribution of the rejected tones of vibrations for mechanical systems was also considered in [38], where the authors propose to add to the calculation the correction obtained when solving the auxiliary task of statics. This has greatly reduced the number of modes taken into account to achieve the required accuracy.

In addition, the issue of introducing a quasistatic correction to the dynamic calculation to improve the convergence of the results was considered in [39, 40]. The authors proposed to introduce as an addition the quasistatic component of unrecorded modes of oscillations, which is defined as the difference between the solution of the quasistatic problem and the quasistatic component of the modes of oscillations taken into account in the calculation.

The method of static accounting for the highest vibration modes was proposed in [41–43] for determining the natural vibration frequencies. In our work, it is extended to problems of forced oscillations and involves solving a dynamic problem by the method of spectral expansion in a series of modes with a small number of modes taken into account, as well as solving auxiliary static problems in an exact and approximate formulation.

The purpose of this work is to solve the problem of the dynamics of forced oscillations, taking into account the contribution of the highest modes. The following tasks are solved:

1. The theoretical description of the method under consideration and the formulation of auxiliary problems.
2. Construction of design schemes of spatial structures and determination of their stress-strain state from the action of dynamic and static loads.
3. Comparison of the results obtained in solving the problem of dynamics by the classical method and the method of static accounting for the contribution of the highest modes of oscillations.

2. Methods

Let us consider the standard way to solve a dynamic task. Let the system undergo forced oscillations, its equation of motion is:

$$\rho \ddot{u} = L(u) + q, \quad (1)$$

where $u(x, t)$ is the desired displacement;

ρ is the density of system elements;

q is external dynamic load;

$L(u)$ is an operator of a static task, depending on the nature of the work of the structure;

It can be demonstrated the following examples of the mode of the operator of the static task $L(u)$:

a) $L(u) = EAu''$ is for tasks in tension and compression;

b) $L(u) = -EIu^{IV}$ is for the task on bending rods;

c) $L(u) = -D(\partial^4 u / \partial x^4 + 2\partial^4 u / \partial x^2 \partial y^2 + \partial^4 u / \partial y^4)$ is for tasks of plate bending;

Let the external harmonic load $p(t) = P_0 \sin(\theta t)$ acts on the system, then the equation of motion will look like (2):

$$L(u) + \rho\theta^2 u + P_0 = 0. \quad (2)$$

The desired displacement is determined using the method of spectral decomposition in a row according to the modes of natural oscillations by the formula (3):

$$u_n(x) = \sum_{k=1}^n a_k U_k(x), \quad (3)$$

where n is the number of considered modes;

a_k is the amplitude value of the k -mode $U_k(x)$;

Thus, the solution of a dynamic problem by the formula (3) implies the choice of such a number n of the system's natural oscillations taken into account, which will be enough to find the desired displacement with the necessary accuracy. This number can be quite large, which will lead to a significant investment of time and resources.

Therefore, it is possible to approach the solution of this problem in another way: take in the formula (3) a small number of the terms $N(N \ll n)$, and the rest (higher modes of oscillations) to take into account in the calculation statically.

To do this, the first step is to consider the solution of the auxiliary static task from the action of the static force P_0 . The exact static displacement is determined by solving the differential equilibrium equation (4):

$$L(u) + P_0 = 0. \quad (4)$$

The next step is to solve another auxiliary static problem by using the method of spectral decomposition in a row according to the modes of natural oscillations. Similar to solving a dynamic problem, you can write an expression for this static task in the next mode (5):

$$u_{n,st}(x) = \sum_{k=1}^n b_k U_k(x). \quad (5)$$

Having solved auxiliary static problems using formulas (4) and (5), one can find the desired displacement of a dynamic problem when taking into account a small number N modes of natural oscillations in the following formula (6):

$$u(x) = u_N(x) + [u_{ex,st}(x) - u_{N,st}(x)], \quad (6)$$

where $u_N(x)$ is the solution of a dynamic task by the formula (3);

$u_{ex,st}(x)$ is the exact solution of the static task by the formula (4);

$u_{N,st}(x)$ is an approximate solution of the static problem by the formula (5).

Thus, the difference $[u_{ex,st}(x) - u_{N,st}(x)]$, obtained in formula (6), is the static contribution of the rejected natural oscillations in formula (3). Figure 1 shows a graphical illustration of the use of this approach to solving problems.

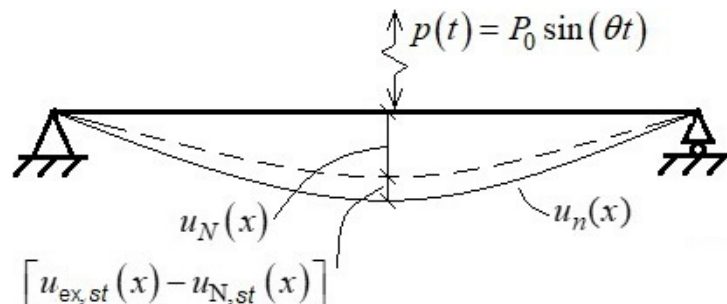


Figure 1. Beam deflection when solving a dynamic problem with a static account of the contribution of highest modes.

As is well known, the movement of a point mass with steady-state oscillations has the formula (7):

$$u(t) = u_{st}\beta(t), \quad (7)$$

here u_{st} is the static deflection of the beam at the location of the point mass from the statically applied force P_0 ; $\beta(t)$ is the dynamic coefficient equal to the ratio of the dynamic displacement $u(t)$ to the static displacement u_{st} at a given time.

If an external harmonic load acts on the system, then the maximum value of the coefficient β in case of forced damped oscillations can be found using formula (8):

$$\beta = \frac{1}{\sqrt{\left(1 - \frac{\theta^2}{\omega^2}\right)^2 + \gamma_{in}^2 \frac{\theta^2}{\omega^2}}}. \quad (8)$$

As noted above, the auxiliary static task should be solved by the method of expansion in a row in the modes of natural oscillations. For this, a static calculation is carried out as a solution to a dynamic problem with an external load in the mode $p(t) = P_0 \sin(\theta t)$, where a very small value of the angular frequency is specified. From formula (8), $\beta \rightarrow 1$ as $\theta \rightarrow 0$ and according to (1) the solution of the dynamic problem will tend to solve statically.

3. Results and Discussion

In order to verify the method of static accounting of the highest modes of oscillations, two calculation schemes were built in the SCAD Office 21.1 software package.

2.1. The space frame

The system consists of rod finite elements (Figure 2). The overall dimensions of the design scheme are 12×10×14 m. The lower nodes of the system are rigidly clamped. The material is B25 concrete, the dimensions of the cross sections of the elements are 20×20, 35×40, 50×50 cm × cm (Figure 3). The harmonic dynamic load $p(t) = P_0 \sin(\theta t)$ is applied at node 15 in the X direction. The amplitude of the force P_0 is assumed to be 100 T, the angular frequency was set in two variants: $\theta_1 = 8$ rad/s and $\theta_2 = 13$ rad/s. According to the results of the modal analysis, the first, second and third natural frequencies (eigenfrequencies) of the system are respectively 10.7, 11.4 and 15.5 rad/s. For reinforced concrete structures adopted the coefficient of inelastic resistance of the material $\gamma_{in} = 0.09$.

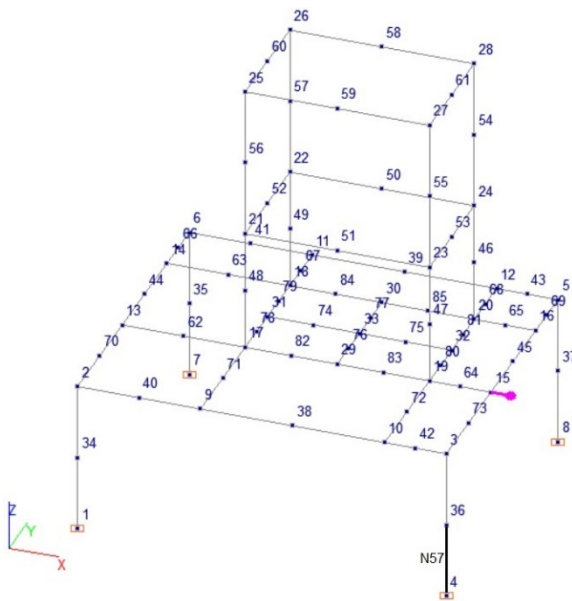


Figure 2. Spatial frame scheme.



Figure 3. Stiffness of scheme elements.

The movement of nodes 2 and 25 in the X direction is considered, as well as the bending moment relative to the Y axis in the N57 element (in Figure 2, it is highlighted with a thick line). The result of the calculation of the frame on the dynamic load is shown in Table 1.

Table 1. Dynamic frame calculation.

| Number of the mode | $\theta = 8 \text{ rad/s}$ | | | $\theta = 13 \text{ rad/s}$ | | |
|--------------------|----------------------------|----------------------|----------------------------------|-----------------------------|----------------------|----------------------------------|
| | $u_2, \text{ mm}$ | $u_{25}, \text{ mm}$ | $M_{57}, \text{ T}\cdot\text{m}$ | $u_2, \text{ mm}$ | $u_{25}, \text{ mm}$ | $M_{57}, \text{ T}\cdot\text{m}$ |
| 1 | -2.535 | -148.860 | -5.672 | -2.368 | 139.011 | -5.296 |
| 2 | -2.563 | -149.577 | -5.841 | -2.396 | 139.730 | -5.529 |
| 3 | -2.744 | -158.363 | -6.234 | -1.942 | 117.410 | -4.544 |
| 5 | -41.725 | -118.532 | -99.719 | -47.466 | 164.646 | -113.912 |
| 7 | -48.053 | -116.483 | -113.526 | -54.400 | 166.908 | -128.890 |
| 10 | -48.909 | -125.380 | -115.641 | -55.327 | 157.519 | -131.180 |
| 15 | -49.291 | -125.775 | -116.287 | -55.732 | 157.101 | -131.877 |
| 30 | -45.554 | -126.341 | -108.006 | -51.945 | 156.542 | -123.485 |
| 60 | -45.372 | -126.000 | -106.461 | -51.763 | 156.879 | -121.933 |
| 100 | -45.332 | -126.004 | -106.378 | -51.723 | 156.874 | -121.849 |
| 140 | -45.373 | -126.005 | -106.620 | -51.763 | 156.874 | -122.091 |
| 180 | -45.373 | -126.005 | -106.620 | -51.763 | 156.874 | -122.091 |
| 220 | -45.373 | -126.005 | -106.619 | -51.763 | 156.874 | -122.090 |
| 250 | -45.373 | -126.005 | -106.619 | -51.763 | 156.874 | -122.090 |

As can be seen, the desired values cease to change significantly already taking into account the 60 modes.

Further, the auxiliary static problem was exactly solved by formula (4) from a force equal to the amplitude of the force P_0 . Exact static displacements of nodes 2 and 25 are -39.203 and -44.940 mm respectively, and the bending moment in the element N57 is 92.139 T·m.

The next step is also the static problem was solved by the dynamic method at the frequency of the forcing force $\theta = 0.0001$. As shown in the previous paragraph, at such a frequency, the solution of the dynamic problem should practically coincide with the solution of the static problem. The results of the calculation with a different number of considered modes are given in Table 2.

From Table 2 it can be seen that the method of solving a static problem proposed in this paper by solving a dynamic problem with a very low frequency of the forcing force really converges to an exact solution to the static problem with an increase in the number of vibrational modes taken into account.

Table 2. Static calculation of the frame through modes of oscillations.

| Number of modes | $u_2, \text{ mm}$ | $u_{25}, \text{ mm}$ | $M_{57}, \text{ T}\cdot\text{m}$ |
|-----------------|-------------------|----------------------|----------------------------------|
| 1 | -1.138 | -66.839 | -2.547 |
| 2 | -1.151 | -67.166 | -2.630 |
| 3 | -1.278 | -73.316 | -2.904 |
| 4 | -35.924 | -37.643 | -85.993 |
| 5 | -35.895 | -37.660 | -85.924 |
| 6 | -36.095 | -36.962 | -85.183 |
| 8 | -42.687 | -43.642 | -101.025 |
| 10 | -42.721 | -44.329 | -101.112 |
| 12 | -43.129 | -45.372 | -102.213 |
| 14 | -41.300 | -44.713 | -97.782 |
| 16 | -41.893 | -44.609 | -99.060 |
| 200 | -39.203 | -44.940 | -92.139 |
| 250 | -39.203 | -44.940 | -92.139 |

As follows from Table 1, a practically exact solution to the problem of dynamics was obtained when taking into account 140 modes of natural oscillations. In Table 3, this exact solution is compared with the solution proposed by the proposed method, taking into account 5 modes.

Table 3. Frame calculation results.

| No. | Solution | $\theta = 8 \text{ rad/s}$ | | | $\theta = 13 \text{ rad/s}$ | | |
|-----|---|----------------------------|----------------------|----------------------------------|-----------------------------|----------------------|----------------------------------|
| | | $u_2, \text{ mm}$ | $u_{25}, \text{ mm}$ | $M_{57}, \text{ T}\cdot\text{m}$ | $u_2, \text{ mm}$ | $u_{25}, \text{ mm}$ | $M_{57}, \text{ T}\cdot\text{m}$ |
| (1) | Dynamic Solution with $N = 5$ | -41.725 | -118.532 | -99.719 | -47.466 | 164.646 | -113.912 |
| (2) | Dynamic Solution with $N = 10$ | -48.909 | -125.380 | -115.641 | -55.327 | 157.519 | -131.180 |
| (3) | Dynamic Solution with $N = 15$ | -49.291 | -125.775 | -116.287 | -55.732 | 157.101 | -131.877 |
| (4) | Dynamic Solution with $N = 30$ | -45.554 | -126.341 | -108.006 | -51.945 | 156.542 | -123.485 |
| (5) | Static exact solution | -39.203 | -44.94 | -92.140 | -39.203 | -44.940 | -92.140 |
| (6) | Static solution with $N = 5$ | -35.895 | -37.660 | -85.924 | -35.895 | -37.660 | -85.924 |
| (7) | Static contribution of higher modes | -3.308 | -7.280 | -6.216 | -3.308 | -7.280 | -6.216 |
| (8) | Dynamic solution with static accounting mode with $N = 5$ | -45.033 | -125.812 | -105.935 | -50.774 | 157.366 | -120.128 |
| (9) | Dynamic exact solution | -45.373 | -126.005 | -106.619 | -51.763 | 156.874 | -122.090 |

Analysis of the results shown in Table 3 allows us to find the errors of various methods. These errors are given in Table 4, where the following is indicated: Δ is absolute error; ε is relative error.

Table 4. Comparison of results between different methods.

| Difference between | Type | $\theta = 8 \text{ rad/s}$ | | | $\theta = 13 \text{ rad/s}$ | | |
|--------------------|-------------------|----------------------------|----------------------|----------------------------------|-----------------------------|----------------------|----------------------------------|
| | | $u_2, \text{ mm}$ | $u_{25}, \text{ mm}$ | $M_{57}, \text{ T}\cdot\text{m}$ | $u_2, \text{ mm}$ | $u_{25}, \text{ mm}$ | $M_{57}, \text{ T}\cdot\text{m}$ |
| (8) and (9) | Δ | -0.340 | -0.193 | -0.684 | -0.989 | -0.492 | -1.962 |
| | $\varepsilon, \%$ | 0.75 | 0.15 | 0.64 | 1.91 | 0.31 | 1.61 |
| (1) and (9) | Δ | 3.648 | 7.473 | 6.900 | 4.297 | 7.772 | 8.178 |
| | $\varepsilon, \%$ | 8.04 | 5.93 | 6.47 | 8.30 | 4.95 | 6.70 |
| (2) and (9) | Δ | -3.536 | 0.625 | -9.022 | -3.564 | 0.645 | -9.090 |
| | $\varepsilon, \%$ | 7.79 | 0.50 | 8.46 | 6.89 | 0.41 | 7.45 |
| (3) and (9) | Δ | -3.918 | 0.230 | -9.668 | -3.969 | 0.227 | -9.787 |
| | $\varepsilon, \%$ | 8.64 | 0.18 | 9.07 | 7.67 | 0.14 | 8.02 |
| (4) and (9) | Δ | -0.181 | -0.336 | -1.387 | -0.182 | -0.332 | -1.395 |
| | $\varepsilon, \%$ | 0.40 | 0.27 | 1.30 | 0.35 | 0.21 | 1.14 |

Analysis of the results in Table 4, allows to formulate the following conclusions:

1. The use of the method of static accounting of the highest forms of oscillations can significantly improve the accuracy of the results both in terms of displacements and in terms of internal efforts, compared to the standard method with comparable computational costs. For example, the standard method when accounting for 10 modes gives an error of 7–8 %; the proposed method when accounting for 5 modes gives an error of 1–2 %; at the same time, in the proposed method it is necessary to solve the dynamic problem twice, taking into account 5 modes, which is less in computational costs than one solution with 10 modes.

2. The standard method only when taking into account 30 modes gives errors comparable to the errors of the proposed method when taking into account 5 modes. Thus, the proposed method can significantly reduce computational costs to achieve the same accuracy of the solution.

4. The bendable plate

The plate consists of plates (Figure 4). The overall dimensions of the design scheme are 4x5 m. The right and left nodes of the system are rigidly clamped. The material is concrete B25, slab thickness is 15 cm. Forcing dynamic load $p(t) = P_0 \sin(\theta t)$ is applied at node N68 in the Z direction. The amplitude of the forcing force P_0 is assumed to be 100T, the angular frequencies were also set in two variants: $\theta_1 = 110 \text{ rad/s}$ and $\theta_2 = 150 \text{ rad/s}$. According to the results of the modal analysis, the first, second and third natural frequencies of the system are 129.9, 170.2 and 323.3 rad/s. For reinforced concrete structures adopted the coefficient of inelastic resistance of the material $\gamma_{in} = 0.09$.

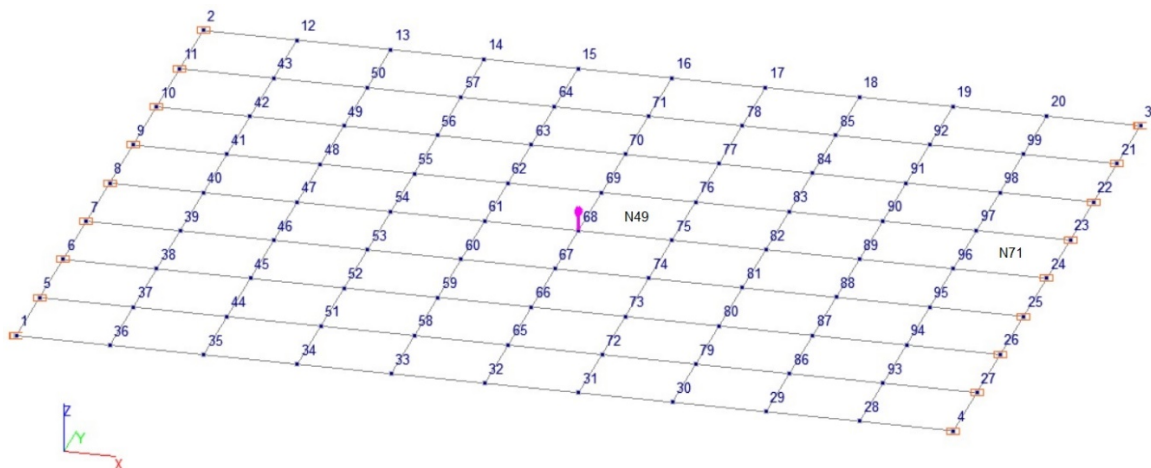


Figure 4. Plate design scheme.

In this case, the vertical movement of the node 68, the bending moment in the N49 element and the shear force in the N71 element (Figure 4) were considered. The result of the calculation of the plate on the dynamic load is given in Table 5.

Table 5. Dynamic plate calculation.

| Number of modes | $\theta = 110 \text{ rad/s}$ | | | $\theta = 150 \text{ rad/s}$ | | |
|-----------------|------------------------------|------------------------------------|-----------------------|------------------------------|------------------------------------|-----------------------|
| | $u_{68}, \text{ mm}$ | $M_{49}, \text{ T}\cdot\text{m/m}$ | $Q_{71}, \text{ T/m}$ | $u_{68}, \text{ mm}$ | $M_{49}, \text{ T}\cdot\text{m/m}$ | $Q_{71}, \text{ T/m}$ |
| 1 | -56.892 | 32.970 | -52.300 | 48.060 | -27.854 | 44.118 |
| 2 | -56.892 | 32.973 | -52.226 | 48.060 | -27.854 | 44.118 |
| 3 | -61.325 | 31.318 | -61.721 | 43.304 | -24.278 | 34.091 |
| 5 | -61.325 | 36.318 | -61.721 | 43.304 | -24.278 | 34.091 |
| 7 | -61.325 | 36.318 | -61.721 | 43.304 | -24.278 | 34.090 |
| 10 | -61.742 | 37.799 | -56.096 | 42.896 | -22.843 | 39.515 |
| 15 | -62.584 | 39.725 | -50.689 | 42.079 | -21.020 | 44.834 |
| 30 | -62.883 | 40.976 | -56.467 | 41.791 | -19.859 | 39.182 |
| 60 | -63.228 | 41.663 | -54.094 | 41.459 | -19.229 | 41.485 |
| 100 | -63.352 | 41.695 | -54.401 | 41.340 | -19.200 | 41.185 |
| 140 | -63.352 | 41.695 | -54.403 | 41.340 | -19.200 | 41.184 |
| 180 | -63.352 | 41.695 | -54.402 | 41.340 | -19.200 | 41.184 |
| 220 | -63.352 | 41.695 | -54.402 | 41.340 | -19.200 | 41.184 |
| 240 | -63.352 | 41.695 | -54.402 | 41.340 | -19.200 | 41.184 |

As can be seen, the desired values cease to change significantly already taking into account 100 modes.

The exact static displacement of the node 68 from the amplitude forcing force of 100 T is 22.793 mm, the bending moment in the element N49 is 18.155 T·m/m, the lateral force at the node N71 is 16.624 T·m/m.

The next step is also the static problem was solved by the dynamic method at the frequency of the forcing force $\theta = 0.0001 \text{ rad/s}$. As was proved in the previous paragraph, at such a frequency, the solution of the dynamic problem practically coincides with the solution of the static task.

As follows from Table 5, a practically exact solution of the dynamics problem was obtained with account of 100 modes of natural oscillations. In Table 6, this exact solution is compared with the solution proposed by the proposed method, taking into account 5 modes.

Table 6. The results of the calculation of the plate.

| No. | Solution | $\theta = 110 \text{ rad/s}$ | | | $\theta = 150 \text{ rad/s}$ | | |
|-----|---|------------------------------|------------------------------------|-----------------------|------------------------------|------------------------------------|-----------------------|
| | | $u_{68}, \text{ mm}$ | $M_{49}, \text{ T}\cdot\text{m/m}$ | $Q_{71}, \text{ T/m}$ | $u_{68}, \text{ mm}$ | $M_{49}, \text{ T}\cdot\text{m/m}$ | $Q_{71}, \text{ T/m}$ |
| (1) | Dynamic Solution with $N = 10$ | -61.742 | 37.799 | -56.096 | 42.896 | -22.843 | 39.515 |
| (2) | Dynamic Solution with $N = 15$ | -62.584 | 39.725 | -50.689 | 42.079 | -21.020 | 44.834 |
| (3) | Dynamic Solution with $N = 30$ | -62.883 | 40.976 | -56.467 | 41.791 | -19.859 | 39.182 |
| (4) | Dynamic Solution with $N = 60$ | -63.228 | 41.663 | 54.094 | 41.459 | -19.229 | 41.485 |
| (5) | Static exact solution | -22.793 | 18.155 | -16.624 | -22.793 | 18.155 | -16.624 |
| (6) | Static solution with $N = 5$ | -20.732 | 12.717 | -23.931 | -20.732 | 12.717 | -23.931 |
| (7) | Static contribution of higher modes | -2.061 | 5.438 | 7.307 | -2.061 | 5.438 | 7.307 |
| (8) | Dynamic solution with static accounting mode with $N = 5$ | -63.386 | 41.756 | -54.414 | 41.243 | -18.840 | 41.398 |
| (9) | Dynamic exact solution | -63.352 | 41.695 | -54.402 | 41.340 | -19.200 | 41.184 |

Analysis of the results shown in Table 6 allows us to find the errors of various methods. These errors are listed in Table 7, where: Δ is the absolute error; ε is relative error.

Analysis of the results shown in Table 7, allows to formulate the following conclusions:

1. The use of the method of static accounting of the highest modes of oscillations can significantly improve the accuracy of the results both in terms of displacements and in terms of internal efforts, compared to the standard method with comparable computational costs. For example, the standard method when accounting for 15 modes gives errors of 2–10 %; the proposed method when accounting for 5 modes gives an error of 0.02–2 %; at the same time, in the proposed method it is necessary to solve the dynamic problem twice, taking into account 5 modes, which is less in computational costs than one solution with 15 modes.

2. The standard method only when accounting for 60 modes gives an error comparable to the error of the proposed method when accounting for 5 modes. Thus, the proposed method can significantly reduce computational costs to achieve the same accuracy of the solution.

Table 7. Comparison of results between different methods.

| Difference between | Type | $\theta = 110 \text{ rad/s}$ | | | $\theta = 150 \text{ rad/s}$ | | |
|--------------------|-------------------|------------------------------|------------------------------------|-----------------------|------------------------------|------------------------------------|-----------------------|
| | | $u_{68}, \text{ mm}$ | $M_{49}, \text{ T}\cdot\text{m/m}$ | $Q_{71}, \text{ T/m}$ | $u_{68}, \text{ mm}$ | $M_{49}, \text{ T}\cdot\text{m/m}$ | $Q_{71}, \text{ T/m}$ |
| (8) and (9) | Δ | -0.034 | -0.061 | -0.012 | 0.097 | 0.360 | 0.214 |
| | $\varepsilon, \%$ | 0.05 | 0.15 % | 0.02 | 0.23 | 1.88 | 0.52 |
| (1) and (9) | Δ | 1.610 | -3.896 | -1.694 | 1.556 | -3.643 | -1.669 |
| | $\varepsilon, \%$ | 2.54 | 9.34 | 3.11 | 3.76 | 18.97 | 4.05 |
| (2) and (9) | Δ | 0.768 | -1.970 | 3.713 | 0.739 | -1.820 | 3.650 |
| | $\varepsilon, \%$ | 1.21 % | 4.72 | 6.83 | 1.79 | 9.48 | 8.86 |
| (3) and (9) | Δ | 0.469 | -0.719 | -2.065 | 0.451 | -0.659 | -2.002 |
| | $\varepsilon, \%$ | 0.74 | 1.72 | 3.80 | 1.09 | 3.43 | 4.86 |
| (4) and (9) | Δ | 0.124 | 0.032 | 0.308 | 0.119 | 0.029 | 0.301 |
| | $\varepsilon, \%$ | 0.20 | 0.08 | 0.57 | 0.29 | 0.15 | 0.73 |

5. Conclusions

1. In this paper proposed a method for solving a dynamic problem from the action of a harmonic load on structures, based on a static account of higher modes of oscillation. The method requires solving two dynamic problems and one static task.

2. As shown in the examples, the proposed method gives a high accuracy of the solution at lower computational costs compared with the standard method of decomposition in its own modes of oscillation. High accuracy of the solution is obtained not only by movements, but also by efforts.

3. Solving a dynamic problem with a static account of the highest modes of oscillations can significantly save computation time and computer resources, since it is necessary to solve one dynamic problem with a small number of modes and two static tasks, instead of solving one dynamic problem with a large number of modes taken into account in the calculation. As is known, the relationship between the number of forms taken into account and computational costs is non-linear. With a decrease in the dimension of the problem, its solution is an order of magnitude easier and faster.

4. In the future, it is planned to extend the method of static accounting of the highest modes of oscillations to tasks with an arbitrary time-dependent load, as well as to problems of calculating structures from seismic effects.

References

- Tusnina, V.M., Emelianov, D.A. The seismic stability of facade system with facing by composite panels. Magazine of Civil Engineering. 2018. 80(4). Pp. 62–72. DOI: 10.18720/MCE.80.6.
- Karpov, A.S. Raschet sobstvennykh chastot i form kolebaniy opornykh i proletrykh konstruksiy avtomobilnykh estakad [Calculation of natural frequencies and mode shapes of spans and supporting road flyovers]. [Online]. System requirements: AdobeAcrobatReader. URL: <https://naukovedenie.ru/PDF/19KO514.pdf> (reference date: 08.03.2019). (rus)
- Indeykin, I.A., Chizhov, S.V., Shestakova, E.B., Antonyuk, A.A., Evtukov, E.S., Kulagin, K.N., Karpov, V.V., Golitsynsky, G.D. Dynamic stability of the lattice truss of the bridge taking into account local oscillations. Magazine of Civil Engineering. 2017. 76(8). Pp. 266–278. DOI: 10.18720/MCE.76.23.
- Ivanov, A.Y., Chernogorskiy, S.A., Vlasov, M.P. Seismic design optimization considering base-isolation system. Magazine of Civil Engineering. 2018. 80(4). Pp. 138–150. DOI: 10.18720/MCE.80.13
- Martelli, A., Forny, M. Seismic isolation: present application and perspectives. International Workshop On Base Isolated High-rise Buildings. Yerevan, Armenia. 2006. Pp. 1–26.
- Li, S., Zuo, Zh., Zhai, Ch., Xie, L. Comparison of static pushover and dynamic analyses using RC building shaking table experiment. Engineering Structures. 2017. No. 136. Pp. 430–440.
- Mazza, F. Seismic demand of base-isolated irregular structures subjected to pulse-type earthquakes. Soil Dynamics and Earthquake Engineering. 2018. No. 108. Pp. 111–129.
- Momtaz, A.A., Abdollahian, M.A., Farshidianfar, A. Study of wind-induced vibrations in tall buildings with tuned mass dampers taking into account vortices effects [Online]. System requirements: AdobeAcrobatReader. URL: <https://link.springer.com/content/pdf/10.1007%2Fs40091-017-0174-9.pdf> (reference date: 08.03.2019).
- Mohamad, A., Poursha, M. A non-adaptive displacementbased pushover procedure for the nonlinear static analysis of tall building frames. Engineering Structures. 2016. No. 126. Pp. 586–597.
- Mrdak, I., Rakočević, M., Žugić, L., Usmanov, R., Murgul, V., Vatin, N. Analysis of the influence of dynamic properties of structures on seismic response according to montenegrin and european regulations. Applied Mechanics and Materials. 2014. Vol. 633–634. Pp. 1069–1076.
- Chintanapakdee, C., Chopra, A.K. Evaluation of Modal Pushover Analysis Using Generic Frames. Earthquake Engineering and Structural Dynamics. 2003. Vol. 32. Pp. 417–442.
- Krawinkler, H., Seneviranta, G.D.P.K. Pros and cons of a pushover analysis of seismic performance evaluation. Engineering Structures. 1998. 20(4). Pp. 452–464.

13. Khodzhaev, D., Abdikarimov, R., Vatin, N. Nonlinear oscillations of a viscoelastic cylindrical panel with concentrated masses [Online]. System requirements: AdobeAcrobatReader. URL: https://www.matec-conferences.org/articles/mateconf/pdf/2018/104/mateconf_eece2018_01001.pdf (reference date: 08.03.2019).
14. Abdikarimov, R., Khodzhaev, D., Vatin, N. To Calculation of Rectangular Plates on Periodic Oscillations. [Online]. System requirements: AdobeAcrobatReader. URL: https://www.matec-conferences.org/articles/mateconf/pdf/2018/104/mateconf_eece2018_01003.pdf (reference date: 08.03.2019).
15. Chopra, A.K., Goel, R.K. A modal pushover analysis procedure for estimating seismic demand of buildings. *Earthquake Engineering and Structural Dynamics*. 2002. No. 31. Pp. 561–582.
16. Denisov, G.V., Lalin, V.V. About the continuous spectrum of vibrations of beam constructions elements under high-frequency effects. *Magazine of Civil Engineering*. 2012. 27(1). Pp. 91–97. Doi: 10.5862/MCE.27.10. (rus)
17. Sokolov, V.A., Strakhov, D.A., Sinyakov, L.N. Design of tower type structures to dynamic effects taking into account flexibility of the pile foundation and the base. *Magazine of Civil Engineering*. 2013. 39(4). Pp. 46–50. (rus)
18. Sukhoterina, M.V., Baryshnikov, S.O., Knysh, T.P., Abdikarimov, R.A. Natural oscillations of a rectangular plates with two adjacent edges clamped. *Magazine of Civil Engineering*. 2018. 82(6). Pp. 81–94. DOI: 10.18720/MCE.82.8.
19. Tyapin, A.G. Non-Classical Damping in the Soil-Structure System and Applicability of the Linear-Spectral Method to the Calculation of Forces. *Earthquake engineering. Constructions safety*. 2016. No. 4. Pp. 44–49. (rus)
20. Fajfar, P.A Nonlinear Analysis Method for Performance Based Seismic Design. *Earthquake Spectra*. 2000. Vol. 16. Pp. 573–592.
21. Akulenko, L.D. High-frequency natural oscillations of mechanical systems. *Journal of Applied Mathematics and Mechanics*. 2000. Vol. 64. No. 5. Pp. 783–796.
22. Nguyen, A.H., Chintanapakee, C., Hayashikawa, T. Assessment of current nonlinear static procedures for seismic evaluation of BRBF buildings. *Journal of Constructional Steel Research*. 2010. No. 66. Pp. 1118–1127.
23. Poursha, M., Khoshnoudian, F., Moghadam, A. The extended consecutive modal pushover procedure for estimating the seismic demands of two-way unsymmetric-plan tall buildings under influence of two horizontal components of ground motions. *Soil Dynamics and Earthquake Engineering*. 2014. No. 63. Pp. 162–173.
24. Soleimani, S., Aziminejad, A., Moghadam, A. Approximate two-component incremental dynamic analysis using a bidirectional energy-based pushover procedure. *Engineering Structures*. 2018. No. 157. Pp. 86–95.
25. Barkov, Yu.A., Bestuzheva, A.S. Formy sobstvennykh kolebaniy betonnoy plotiny s uchetom uprugikh svoystv osnovaniya [Forms of self-oscillations of a concrete dam with the elastic properties reason]. *Scientific and Technical Volga region Bulletin*. 2013. No. 6. Pp. 130–132. (rus)
26. Sergeev, O.A., Kiselev, V.G., Sergeeva, S.A. Optimal design of 3d frame structures taking into account the stress and multiple natural frequency constraints. *Magazine of Civil Engineering*. 2016. 61(1). Pp. 74–81. DOI: 10.5862/MCE.61.7. (rus)
27. Rust, W. *Non-Linear Finite Element Analysis in Structural Mechanics*. Springer, 2015. 367 p.
28. Sergio, Oller. *Nonlinear Dynamics of Structures*. Springer, 2014. 203 p.
29. Tyapin, A.G. Sovremennyye normativnyye podkhody k raschetu otvetstvennykh sooruzheniy na seismicheskiye vozdeystviya [Modern regulatory approaches to the calculation of critical structures for seismic load]. Moscow: ASV, 2018. 518 p. (rus)
30. Datta, T.K. *Seismic Analysis of Structures*. John Wiley & Sons (Asia) Pte Ltd, 2010. 464 p.
31. Pintoa, P.E., Giannini, R., Franchin, P. *Seismic reliability analysis of structures*. Pavia, Italy: iUSS press, 2004. 370 p.
32. Higashino, M., Okamoto, Sh. *Response Control and Seismic Isolation of Buildings*. New York: Taylor & Francis, 2006. 484 p.
33. Sucuoğlu, H., Akkar, S. *Basic Earthquake Engineering. From Seismology to Analysis and Design*. New York City, 2014. 288 p.
34. Josep, M. Font-Llagunes. *Multibody Dynamics. Computational Methods and Applications*. New York City, 2016. 321 p.
35. Denisov, G.V. On the vibrations localization in building structures. *Magazine of Civil Engineering*. 2012. 31(5). Pp. 60–64. DOI: 10.5862/MCE.31.7 (rus)
36. Birbraer, A.N., Sazonova, J.V. Vklad vysshikh mod v dinamicheskiy otklik konstruksiy na vysokochastotnyye vozdeystviya [Input of high modes in dynamic response of structures subjected to high frequency loads]. *Structural Mechanics and Analysis of Constructions*. 2009. Vol. 227(6). Pp. 22–27. (rus)
37. Tyapin, A.G. Realizatsiya "kontseptsii ostatochnogo chlena" v raschetakh sooruzheniy na seismicheskiye vozdeystviya modalnym i spektralnym metodami [Implementation of the "Residual Term" Concept in Seismic Analysis by Modal and Spectral Methods]. *Earthquake engineering. Constructions safety*. 2014. No. 4. Pp. 32–35. (rus)
38. Batseva, O.D., Dmitriyev, S.N. Uchet vysshikh tonov kolebaniy pri vychislenii chuvstvitelnosti sobstvennykh form kolebaniy k variatsiyam parametrov mekhanicheskoy sistemy [Accounting the highest tones of oscillations when calculating the sensitivity of modes of their own to variations in the parameters of a mechanical system]. *Engineering Journal: Science and Innovation*. 2018. 79(7). Pp. 3–23. (rus)
39. Balakirev, Yu.G. Osobennosti vydeleniya kvazistaticheskikh sostavlyayushchikh pri analize dinamicheskogo nagruzheniya uprugikh konstruksiy [Quasistatic components particularities in the analysis of the elastic structures dynamic loading]. *Cosmonautics and rocket engineering*. 2014. Vol. 76(2). Pp. 34–40. (rus)
40. Likhoded, A.I., Sidorov, V.V. Nekotoryye osobennosti skhodimosti metoda razlozheniya po tonam kolebaniy primenitelno k kontinualnym i konechno-elementnym modelyam [Certain Convergence Features of the Decomposition Method by Tones Vibrations Concerning Continuum and Finite-Element Models]. *Cosmonautics and rocket engineering*. 2013. Vol. 71(2). Pp. 20–27. (rus)
41. Zegzhda, S.A. *Soudareniye uprugikh tel [Collision of elastic bodies]*. Saint-Petersburg: Izdatel'stvo Sankt-Peterburgskogo universiteta. 1997. 316 p. (rus)
42. *Seismic Evaluation and Retrofit of Concrete Buildings*. Vol. 1: ATC-40 Report. – Applied Technology Council. Redwood City, California, 1996. 334 p.
43. Chopra, A.K. *Dynamic of structures. Theory and Applications to Earthquake Engineering*. New Jersey: Prentice-Hall, 2006. 794 p.

Contacts:

Tu Quang Trung Le, +7(952)2311578; quangtrung1690@gmail.com
Vladimir Vladimirovich Lalin, +7(921)3199878; vllalin@yandex.ru
Alexey Aleksandrovich Bratashov, +7(981)8451950; aleks.kuskus@mail.ru



DOI: 10.18720/MCE.88.1

Статический учет высших мод колебаний в задачах динамики конструкций

Т.К.Ч. Ле*, В.В. Лалин, А.А. Браташов

Санкт-Петербургский политехнический университет Петра Великого, Санкт-Петербург, Россия

* E-mail: quangtrung1690@gmail.com

Ключевые слова: динамика сооружений, спектральный метод, моды колебаний, высшие формы, статический учет, пространственные конструкции

Аннотация. Расчёт строительных конструкций на динамические воздействия обычно выполняется по методу разложения по собственным формам колебаний. Однако, проблема состоит в том, что такой метод дает точное решение динамической задачи при полном учёте всего спектра мод. Более того, при решении практических задач с использованием программных комплексов динамические расчеты выполняются приближенно с учетом ограниченного количества первых собственных форм колебаний. Вклад в динамическую реакцию сооружения неучтенных высших форм колебаний, как правило, никак не оценивается. Результаты показывают, что, погрешность такого решения динамической задачи может оказаться значительной. Следовательно, настоящая работа посвящена способу статического учета высших форм колебаний в задачах динамики строительных конструкций. Приведено описание основных положений метода, даны примеры его реализации при расчете пространственных конструкций под действием внешней гармонической нагрузки. С помощью расчетного программного комплекса определены перемещения узлов и внутренние усилия в элементах рассматриваемых конструкций. Задавались различные параметры динамического воздействия и число учитываемых мод колебаний. Принятый метод статического учета высших форм колебаний требует решения одной динамической задачи и двух вспомогательных статических задач. Важным обстоятельством подхода является то, что одна из статических задач должна быть решена методом разложения по собственным формам колебаний. Предлагаемый в статье подход позволяет значительно снизить вычислительные затраты на динамический расчёт в сравнении с классическим подходом. Этот результат может иметь большое значение при решении задач на сложные динамические воздействия и для неоднородных по жесткости конструкций.

Литература

1. Туснина В.М., Емельянов Д.А., Сейсмостойкость фасадной системы с облицовкой композитными панелями // Инженерно-строительный журнал. 2018. № 4(80). С. 62–72.
2. Карпов А.С. Расчет собственных частот и форм колебаний опорных и пролетных конструкций автомобильных эстакад [Электронный ресурс]. Систем. требования: AdobeAcrobatReader. URL: <https://naukovedenie.ru/PDF/19KO514.pdf> (дата обращения: 08.03.2019).
3. Индейкин А.В., Чижов С.В., Шестакова Е.Б., Антонюк А.А., Евтюков С.А., Кулагин Н.И., Карпов В.В., Голицынский Д.М. Динамическая устойчивость решетчатой фермы моста с учетом местных колебаний // Инженерно-строительный журнал. 2017. № 8(76). С. 266–278. DOI: 10.18720/MCE.76.23
4. Иванов А.Ю., Черногорский С.А., Власов М.П. Оптимизация конструктивных решений сейсмостойкого проектирования по экономическому критерию // Инженерно-строительный журнал. 2018. № 4(80). С. 138–150.
5. Martelli A., Forny M. Seismic isolation: present application and perspectives // International Workshop On Base Isolated High-rise Buildings. Yerevan, Armenia: 2006. Pp. 1–26.
6. Li S., Zuo Zh., Zhai Ch., Xie L. Comparison of static pushover and dynamic analyses using RC building shaking table experiment // Engineering Structures. 2017. No. 136. Pp. 430–440.
7. Mazza F. Seismic demand of base-isolated irregular structures subjected to pulse-type earthquakes // Soil Dynamics and Earthquake Engineering. 2018. No. 108. Pp. 111–129.
8. Momtaz A.A., Abdollahian M.A., Farshidianfar A. Study of wind-induced vibrations in tall buildings with tuned mass dampers taking into account vortices effects [Электронный ресурс]. Систем. требования: AdobeAcrobatReader. URL: <https://link.springer.com/content/pdf/10.1007%2Fs40091-017-0174-9.pdf> (дата обращения: 08.03.2019).
9. Mohamad A., Poursha M. A non-adaptive displacementbased pushover procedure for the nonlinear static analysis of tall building frames // Engineering Structures. 2016. No. 126. Pp. 586–597.
10. Mrdak I., Rakočević M., Žugić L., Usmanov R., Murgul V., Vatin N. Analysis of the influence of dynamic properties of structures on seismic response according to montenegrin and european regulations // Applied Mechanics and Materials. 2014. Vol. 633–634. Pp. 1069–1076.

11. Chintanapakdee C., Chopra A.K. Evaluation of Modal Pushover Analysis Using Generic Frames // Earthquake Engineering and Structural Dynamics. 2003. Vol. 32. Pp. 417–442.
12. Krawinkler H., Seneviranta G.D.P.K. Pros and cons of a pushover analysis of seismic performance evaluation // Engineering Structures. 1998. No. 20(4). Pp. 452–464.
13. Khodzhaev D., Abdikarimov R., Vatin N. Nonlinear oscillations of a viscoelastic cylindrical panel with concentrated masses [Электронный ресурс]. Систем. требования: AdobeAcrobatReader. URL: https://www.matec-conferences.org/articles/mateconf/pdf/2018/104/mateconf_eece2018_01001.pdf (дата обращения: 08.03.2019).
14. Abdikarimov R., Khodzhaev D., Vatin N. To Calculation of Rectangular Plates on Periodic Oscillations [Электронный ресурс]. Систем. требования: AdobeAcrobatReader. URL: https://www.matec-conferences.org/articles/mateconf/pdf/2018/104/mateconf_eece2018_01003.pdf (дата обращения: 08.03.2019).
15. Chopra A.K., Goel R.K. A modal pushover analysis procedure for estimating seismic demand of buildings // Earthquake Engineering and Structural Dynamics. 2002. No. 31. Pp. 561–582.
16. Денисов Г.В., Лалин В.В. О сплошном спектре колебаний балочных элементов конструкции при высокочастотных воздействиях // Инженерно-строительный журнал. 2012. № 1(27). С. 91–97.
17. Соколов В.А., Страхов Д.А., Синяков Л.Н. Расчет сооружений башенного типа на динамические воздействия с учетом податливости свайного фундамента и основания // Инженерно-строительный журнал. 2013. № 4(39). С. 46–50.
18. Сухотерин М.В., Барышников С.О., Кныш Т.П., Абдикаримов Р.А. Собственные колебания прямоугольной пластины, защемленной по двум смежным краям // Инженерно-строительный журнал. 2018. № 6(82). С. 81–94.
19. Тяпин А.Г. Неклассическое демпфирование в системе «Основание-Сооружение» и вопрос о применимости спектрального метода расчета усилий // Сейсмостойкое строительство. Безопасность сооружений. 2016. № 4. С. 44–49.
20. Fajfar P. A Nonlinear Analysis Method for Performance Based Seismic Design // Earthquake Spectra. 2000. vol. 16. Pp. 573–592.
21. Akulenko L.D. High-frequency natural oscillations of mechanical systems. Journal of Applied Mathematics and Mechanics. 2000. Vol. 64. No. 5. Pp. 783–796.
22. Nguyen A. H., Chintanapakdee C. and Hayashikawa T. Assessment of current nonlinear static procedures for seismic evaluation of BRBF buildings // Journal of Constructional Steel Research. 2010. No 66. Pp. 1118–1127.
23. Poursha M., Khoshnoudian F., Moghadam A. The extended consecutive modal pushover procedure for estimating the seismic demands of two-way unsymmetric-plan tall buildings under influence of two horizontal components of ground motions // Soil Dynamics and Earthquake Engineering. 2014. No. 63. Pp. 162–173.
24. Soleimani S., Aziminejad A., Moghadam A. Approximate two-component incremental dynamic analysis using a bidirectional energy-based pushover procedure // Engineering Structures. 2018. No. 157. Pp. 86–95.
25. Барков Ю.А., Бестужева А.С. Формы собственных колебаний бетонной плотины с учетом упругих свойств основания // Научно-технический вестник Поволжья. 2013. № 6. С. 130–132.
26. Сергеев О.А., Киселев В.Г., Сергеева С.А. Оптимальное проектирование рам с учетом ограничений по прочности и кратным частотам собственных колебаний // Инженерно-строительный журнал. 2016. № 1(61). С. 74–81.
27. Rust W. Non-Linear Finite Element Analysis in Structural Mechanics. Springer, 2015. 367 p.
28. Sergio Oller. Non-linear Dynamics of Structures. Springer, 2014. 203 p.
29. Тяпин А.Г. Современные нормативные подходы к расчету ответственных сооружений на сейсмические воздействия: Научное издание. М.: Издательство АСВ, 2018. 518 с.
30. Datta T.K. Seismic Analysis of Structures. John Wiley & Sons (Asia) Pte Ltd, 2010. 464 p.
31. Pintoa P.E., Giannini R., Franchin P. Seismic reliability analysis of structures. Pavia, Italy: iUSS press, 2004. 370 p.
32. Higashino M., Okamoto Sh. Response Control and Seismic Isolation of Buildings. New York: Taylor & Francis, 2006. 484 p.
33. Sucuoğlu H., Akkar S. Basic Earthquake Engineering. From Seismology to Analysis and Design. New York City, 2014. 288 p.
34. Josep M. Font-Llagunes. Multibody Dynamics. Computational Methods and Applications. New York City, 2016. 321 p.
35. Денисов Г.В. К вопросу о локализации колебаний в строительных конструкциях // Инженерно-строительный журнал. 2012. № 5(31). С. 60–64.
36. Бирбраер А.Н., Сазонова Ю.В. Вклад высших мод в динамический отклик конструкций на высокочастотные воздействия // Строительная механика и расчет сооружений. 2009. № 6(227). С. 22–27.
37. Тяпин А.Г. Реализация «концепции остаточного члена» в расчетах сооружений на сейсмические воздействия модальным и спектральными методами // Сейсмостойкое строительство. Безопасность сооружений. 2014. № 4. С. 32–35.
38. Бацева О.Д., Дмитриев С.Н. Учет высших тонов колебаний при вычислении чувствительности собственных форм колебаний к вариациям параметров механической системы // Инженерный журнал: наука и инновации. 2018. № 7(79). С. 3–23.
39. Балакирев Ю.Г. Особенности выделения квазистатических составляющих при анализе динамического нагружения упругих конструкций // Космонавтика и Ракетостроение. 2014. № 2(76). С. 34–40.
40. Лиходед А.И., Сидоров В.В. Некоторые особенности сходимости метода разложения по тонам колебаний применительно к континуальным и конечно-элементным моделям // Космонавтика и ракетостроение. 2013. № 2(71). С. 20–27.
41. Зегжда С.А. Соударение упругих тел. СПб: Изд-во С.-Петербург. ун-та. 1997. 316с.
42. Seismic Evaluation and Retrofit of Concrete Buildings. Vol. 1: ATC-40 Report. – Applied Technology Council. Redwood City, California. 1996. 334 p.
43. Chopra A.K. Dynamic of structures. Theory and Applications to Earthquake Engineering. New Jersey: Prentice-Hall, 2006. 794 p.

Контактные данные:

Ты Куанг Чунг Ле, +7(952)2311578; эл. почта: quangtrung1690@gmail.com
Владимир Владимирович Лалин, +7(921)3199878; эл. почта: vllalin@yandex.ru
Алексей Александрович Браташов, +7(981)8451950; эл. почта: aleks.kuskus@mail.ru



DOI: 10.18720/MCE.88.2

Factors affecting the ultrasonic disaggregation of powders

S.A. Shakhov*, E.V. Rogova

Siberian Transport University, Novosibirsk, Russia

* E-mail: sashakhov@mail.ru

Keywords: ultrasonic, cavitation, ultrafine additive, disaggregation, grinding, cement, construction

Abstract. Using finely dispersed mineral particles of various origins and morphologies offers a promising strategy in controlling the structure formation in cement composites. However, the use of such additives is hampered because those additives proved to be prone to consolidation into rather dense aggregates. Fine dispersion and disaggregation of powders is possible with the aid of cavitation ultrasonic treatment. However, the optimal conditions for such processing can not be established without conducting simulation studies. The purpose of the present study was the identification of ultrasonic-action factors and conditions ensuring an efficient disaggregation of finely dispersed powders of various origins and particle morphologies. In our study, we used diopside, granulated blastfurnace slag (GBS), wollastonite, ash, and calcium carbonate powders. It is found that the process of ultrasonic treatment of aqueous suspensions is accompanied not only by the dispersion of initial particles and aggregates but, also, by simultaneous formation of new aggregates. That is why the observed variations of the specific surface area and the optical density of powders can be attributed to the variation of the fractional composition of dispersed phase. The activating capability of a mineral additive is due to the fraction of the particles less than 1 μm in size exerting a key influence on the variation of the specific surface area of the powder. Our estimate of the energy efficiency of the cavitation disaggregation of powders during an ultrasonic treatment shows that the most energy-favorable one is the ultrasonic treatment lasting for 1–5 minutes, i.e. during the period of the first half-wave of the variation of the particle fraction less than 1 μm in size.

1. Introduction

A promising method for improving properties of cement composites implies filling the cement-binder matrix with finely dispersed mineral particles of different origin and morphology. An analysis of literature data shows that, as modifiers in structural material science, not only finely dispersed natural materials but, also, various specially prepared powders can be used [1–5]. Introduction of both additives, natural minerals (quartz, granites, basalts and others) and technogenic wastes, promotes an increase of cement-stone density and stability, a reduction of water demand of mixtures and their segregability, an increase of water-retaining capacity and homogeneity of the composites, and shrinkage reduction.

However, the use of such additives is difficult due to their propensity for aggregation and inefficiency with respect to objects of this class of traditional methods of disaggregation by mechanical actions [6]. And, if it is not possible to destroy the aggregates, then the activating effect of the introduced additive decreases sharply, since the main advantage of a highly dispersed powder, the ability to form a large number of contacts with its very small content, is unrealized.

One of the promising research lines in the fine dispersion and disaggregation of dispersed phase is the use of ultrasonic cavitation. The cavitation process features a multi-factorial complexity of phenomena proceeding in the cavitation cavity [7–11]. Under the action of cavitation, on the local scale intense liquid microscopic flows and high-power local shock waves are generated; the shock waves ensure a rise of temperature to 5000 K and a rise of pressure to 100 MPa, both processes leading to mass-transfer

Shakhov, S.A., Rogova, E.V. Factors affecting the ultrasonic disaggregation of powders. Magazine of Civil Engineering. 2019. 88(4). Pp. 14–24. DOI: 10.18720/MCE.88.2.

Шахов С.А., Рогова Е.В. Факторы, влияющие на ультразвуковую дезагрегацию порошков // Инженерно-строительный журнал. 2019. № 4(88). С. 14–24. DOI: 10.18720/MCE.88.2.



This open access article is licensed under CC BY 4.0 (<https://creativecommons.org/licenses/by/4.0/>)

intensification and to a substantial variation of the characteristics of treated medium [11]. Presently, well-substantiated concepts of the mechanism of ultrasonic dispersion are available. According to those concepts, both the shock waves and the acoustic flows having arisen due to the micro-explosions of cavitation bubbles can be factors causing the disintegration of particles and aggregates [6, 14]. Along with the dispersion, a dispersed-phase coagulation process develops in suspensions under the action of ultrasound. The mechanism of acoustic coagulation was attributed to the action of hydrodynamic forces, Bernoulli and Bierkness ones, on the particles. However, the expressions for the latter forces were derived for the case of hydrodynamic action of particles in a uniform steady-state flow of ideal incompressible liquid, whereas the liquid flow with a propagating sonic wave is non-uniform and unsteady. Considering the latter fact, many authors adhere to the opinion that the mechanism of particle coagulation process in a sonic wave fundamentally differs from the picture which the Bernoulli force produces in an incompressible liquid flow [16].

Also, the kinetics of dispersion and coagulation processes is influenced by the intensity and duration of ultrasonic action. In engineering practice, the ultrasound intensity can be evaluated from the oscillation amplitude [6, 7]. The time required for the dispersion of powders depends, first of all, on the intensity of the ultrasonic action, on the physico-mechanical properties of the material to be dispersed, and on the state of the surface of powder particles.

The efficiency of the dispersion process is largely defined by the erosion activity of the liquid, whose magnitude substantially depends on its physico-mechanical properties. Here, the most pronounced action is due to the saturated vapor pressure of the liquid because the micro-impact actions due to cavitation decrease sharply at a high value of the latter pressure inside cavitation bubbles. That is why it is recommended to disperse materials in aqueous solutions as the erosion activity of such solutions proved to be much higher than that of organic solutions [6].

During the ultrasonic treatment, the dispersed-medium temperature affects the cavitation intensity and, hence, the powder dispersion process. For each liquid, there exists a certain range of temperatures in which the intensity of the cavitation action is maximal; for water, this temperature range is 35 to 50 °C [8].

On the whole, the profound scope of performed theoretical and experimental studies has ensured rather wide a range of industrial applications of cavitation technologies [6–10, 17, 20]. Nonetheless, calculation-based identification of the conditions of ultrasonic treatment ensuring most efficient dispersion and disaggregation of powders of different origin and particle morphology is presently impossible. In this connection, there arises a necessity in experimental studies.

The purpose of the present study was to identify factors and conditions of the ultrasonic action providing for a most efficient disaggregation of finely dispersed powders of different origin and particle morphology.

To achieve this goal, the following tasks were solved:

- to establish the nature of the change in the content of particles smaller than 1 μm , depending on the specific surface area of the initial powders and the duration of the ultrasonic treatment;
- to substantiate the energy-preferable duration of processing of powders by ultrasound, which provides a maximum content of particles smaller than 1 μm .

2. Materials and Methods

In the present study, as the carrier medium we used distilled water and as the dispersed phase, powders of heating-plant ash, granulated blastfurnace slag, diopside, wollastonite, and calcium carbonate. The particle size study of the powders was performed on an FSKh-6 photosidometer, whose work is based on the sedimentary Stokes law and the law of radiation attenuation in the turbid media of Lambert-Berra. The granulometric composition of initial powders is shown in Figure 1. It should be noted that for methods based on light scattering there is a characteristic description of the hydrodynamic diameter of particles that can be both primary particles and their aggregates and agglomerates [12, 13]

The optical density of suspensions was measured on a KFK-2MP photocolimeter ($\lambda = 470 \text{ nm}$). The test compositions were prepared by mixing powders in distilled water. The cavitation treatment of specimens was implemented using a UZG Volna-M device generating up to 1000-W ultrasound (model UZTA 1.0/22). The working compounds were placed in a transparent cylindrical vessel, where it was sonicated at a frequency of 22 kHz for different duration and power of ultrasound.

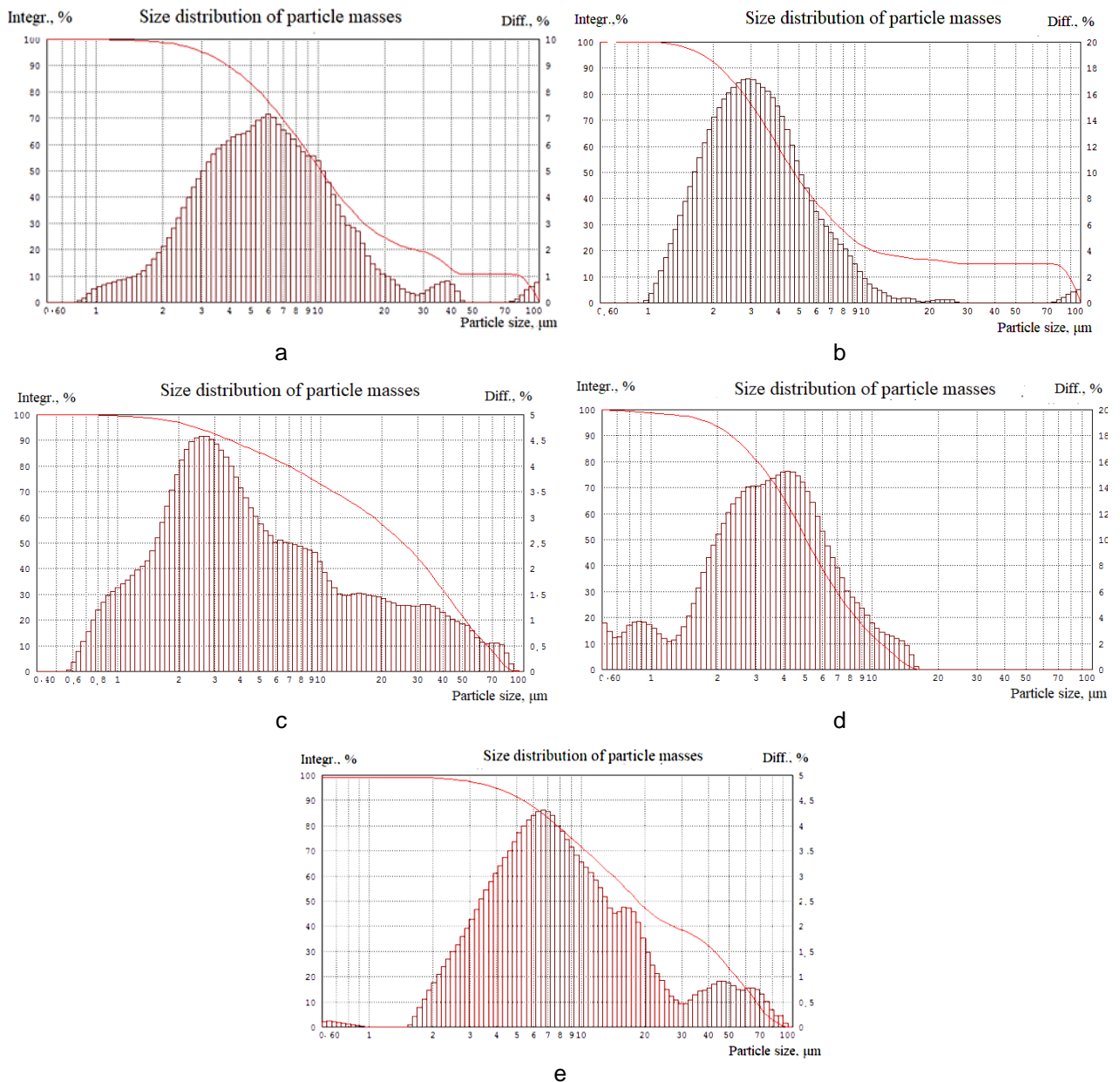


Figure 1. Granulometric composition of virgin (non-processed) powders: a – ash ($S_{sp} = 2840 \text{ cm}^2/\text{g}$), b – granulated blastfurnace slag ($S_{sp} = 4186 \text{ cm}^2/\text{g}$), c – diopside ($S_{sp} = 1840 \text{ cm}^2/\text{g}$), d – wollastonite ($S_{sp} = 5226 \text{ cm}^2/\text{g}$), e – calcium carbonate CaCO_3 ($S_{sp} = 2327 \text{ cm}^2/\text{g}$).

3. Results and Discussion

Treatment with ultrasound of aqueous suspensions of powders of various origins and particle morphologies is accompanied with a change of specific surface area, an integral characteristic characterizing the degree of dispersion and aggregation of powders (Figure 2). The obtained results on the variation of specific surface area proved to be well correlating with the data on the variation of optical density at the passage of light through ultrasonically processed suspensions (Figure 3). The variation of the granulometric composition of dispersed phase can be judged considering the data on the variation of root-mean-square particle diameter (d_m) versus the duration of ultrasonic treatment (Figure 4). For all the powders, the variation of d_m exhibits an oscillating behavior being a result of the dispersion and coagulation processes. During the initial period of ultrasonic treatment (0–5 min), the impact action due to the ultrasonic waves, the intense motions of particles, and the inter-particle collisions all cause the rupturing of bonds between dispersed-phase particles, this rupturing leading to a profound increase of free surface energy (by a factor in excess of 10) [6]. The molecular forces thus increased hamper the further rupturing of particles and aggregates. That is why the rate of dispersion decreases in value during further treatment of the suspension, and the particle aggregation process begins. It should be noted here that, due to coagulation, no restoration of the poly-dispersed system to its initial (pre-dispersion) state occurs since, as a rule, fragments of aggregates and coarse particles never restore into an entity by absorbing water and by forming, due to a higher specific surface energy, a solvate shell with a monolayer of heavily bonded water that will not allow the van der Waals forces to draw together the fine solid particles [14].

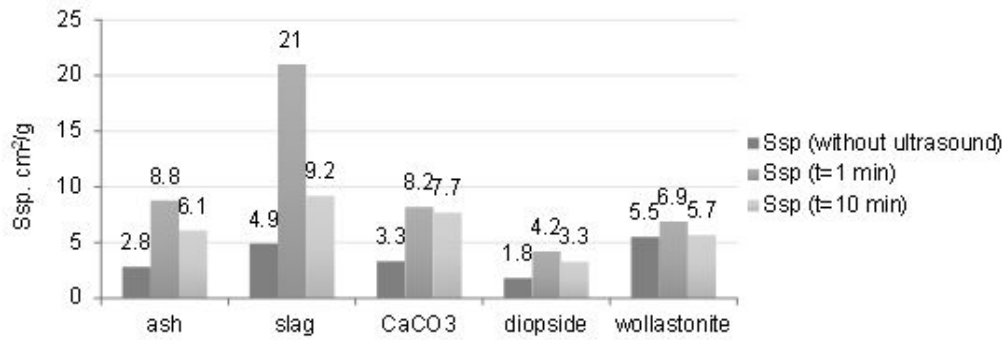


Figure 2. Variation of the specific surface area of powders versus the duration of ultrasonic treatment.

Thus, the ultrasonic treatment of aqueous suspensions is accompanied, first, by the disaggregation of initial particles and aggregates and, second, by the simultaneous formation of new aggregates. That is why the observed variations of specific surface area and optical density are defined by the variation of the fractional composition of dispersed phase. In all the powders, the behaviors exhibited by the fine (sized less than 1 μm) and coarse (sizes greater than 10 μm) particle fractions exhibit an oscillating character being a consequence of the simultaneously proceeding dispersion and coagulation processes. Since, as a rule, at short durations of ultrasonic treatment (less than 5 minutes) the amount of particles smaller than 1 μm in size increases, and the amount of particles greater than 10 μm in size, decreases in magnitude, then the dispersion process at those times prevails over the aggregation process. On the other hand, with increasing the duration of ultrasonic treatment, the amount of particles smaller in size than 1 μm decreases, and the amount of particles greater than 10 μm in size normally increases in magnitude, this finding being indicative of the prevalence of the coagulation process (Figure 4).

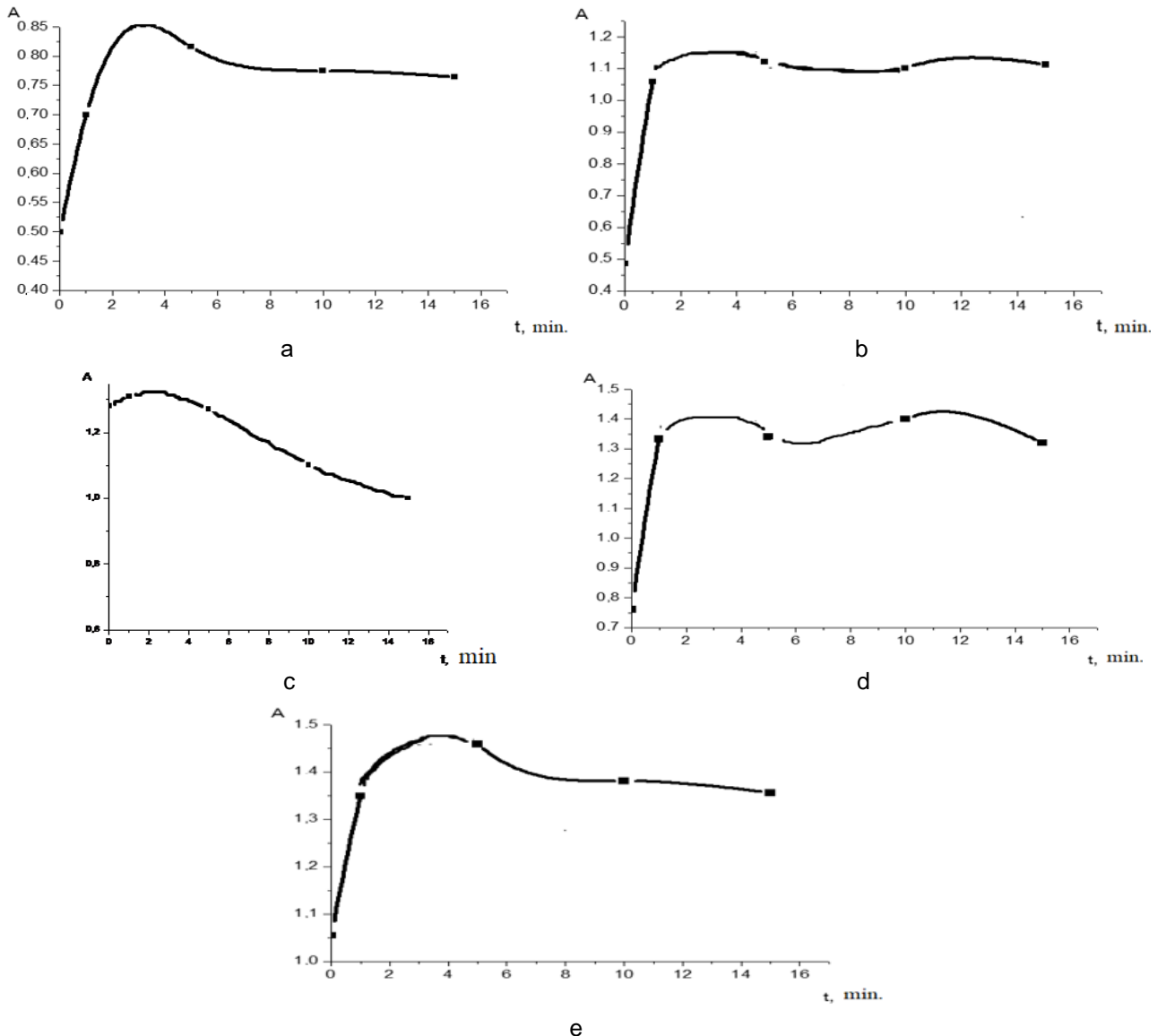


Figure 3. Variation of the optical density of suspension versus the duration of ultrasonic treatment: a – ash; b – diopside; c – CaCO₃; d – granulated blastfurnace slag; e – wollastonite.

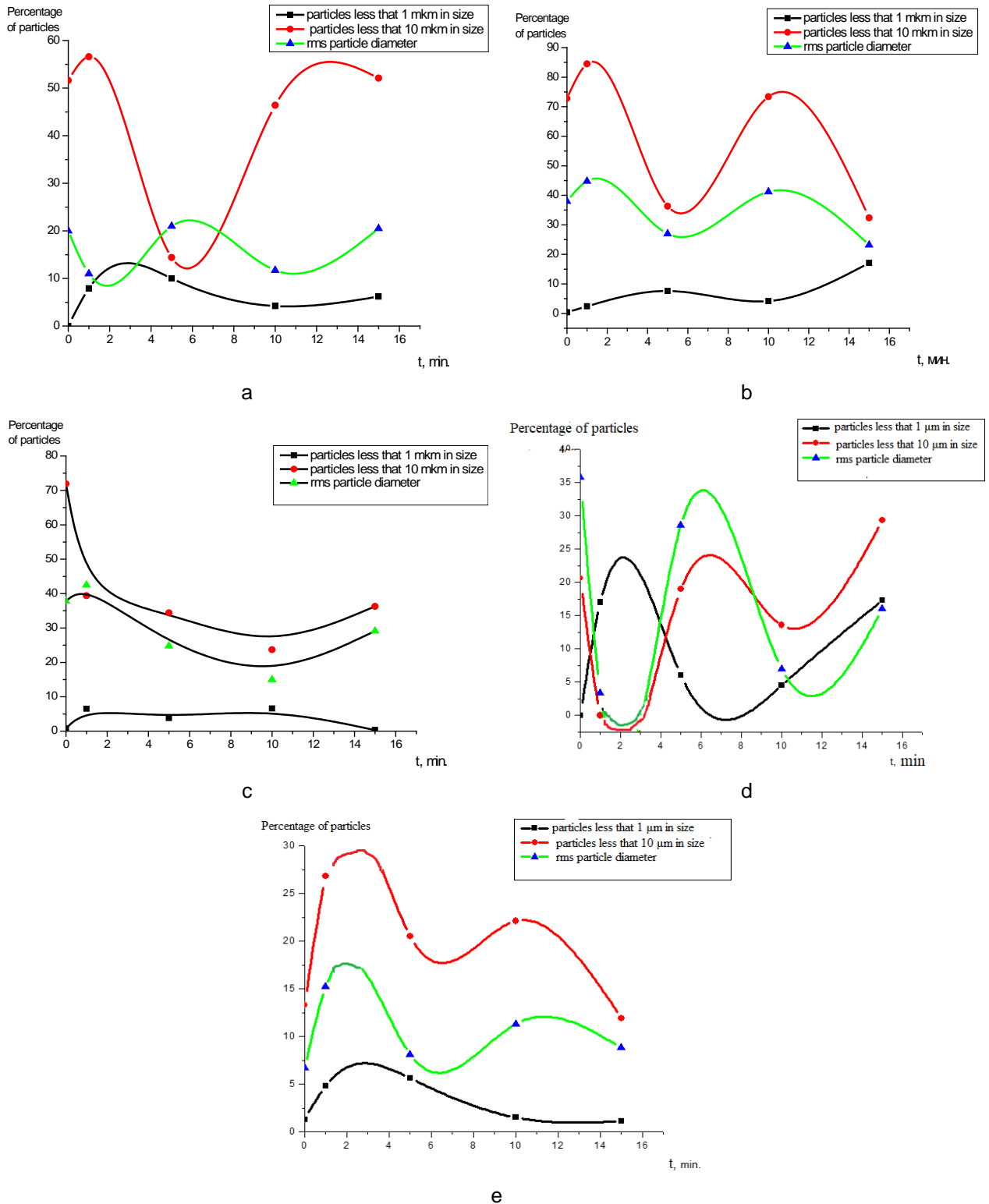


Figure 4. The content of particles versus the duration of ultrasonic treatment: a – ash; b – diopside; c – CaCO₃; d – granulated blastfurnace slag; e – wollastonite.

Under identical conditions of the ultrasonic treatment, the amount of particles of the newly formed fraction sized less than 1 μm exerts a predominant action on the behavior of the specific surface area of particle, a parameter largely determining the activating capacity of the mineral additive (Figure 5). Since the latter regularity is exhibited by powders of various origins and particle morphologies, then the fraction of the particles sized less than 1 μm can be considered as a criterion of the efficiency of the ultrasonic dispersion and disaggregation of mineral additives, whose maximization will promote the enhancement of the reactivity of the mineral additive.

The data in Figures 6–8 show that, along with the duration of supersonic treatment, the intensity of the ultrasonic action and the specific surface area (S_i) of initial powders can be recognized as factors influencing the formation of the maximum amount (fraction) of the particles of the size fraction less than 1 μm in a suspension treated with ultrasound.

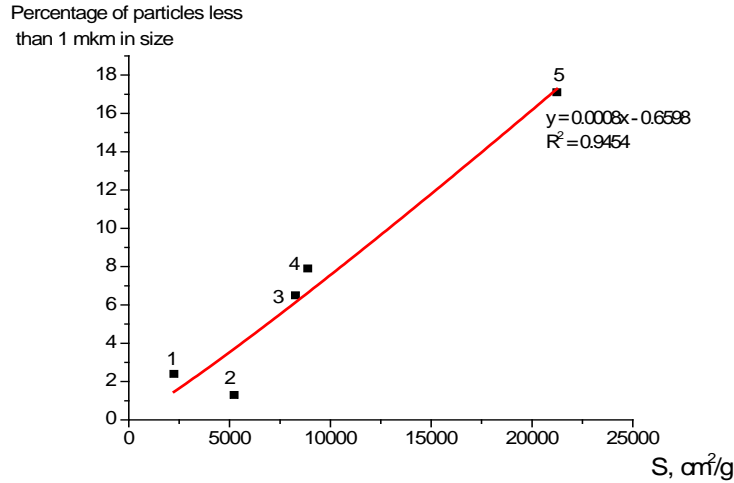


Figure 5. Contents of particles of various size fractions versus the specific surface area of powder for 1-minute duration of ultrasonic treatment.

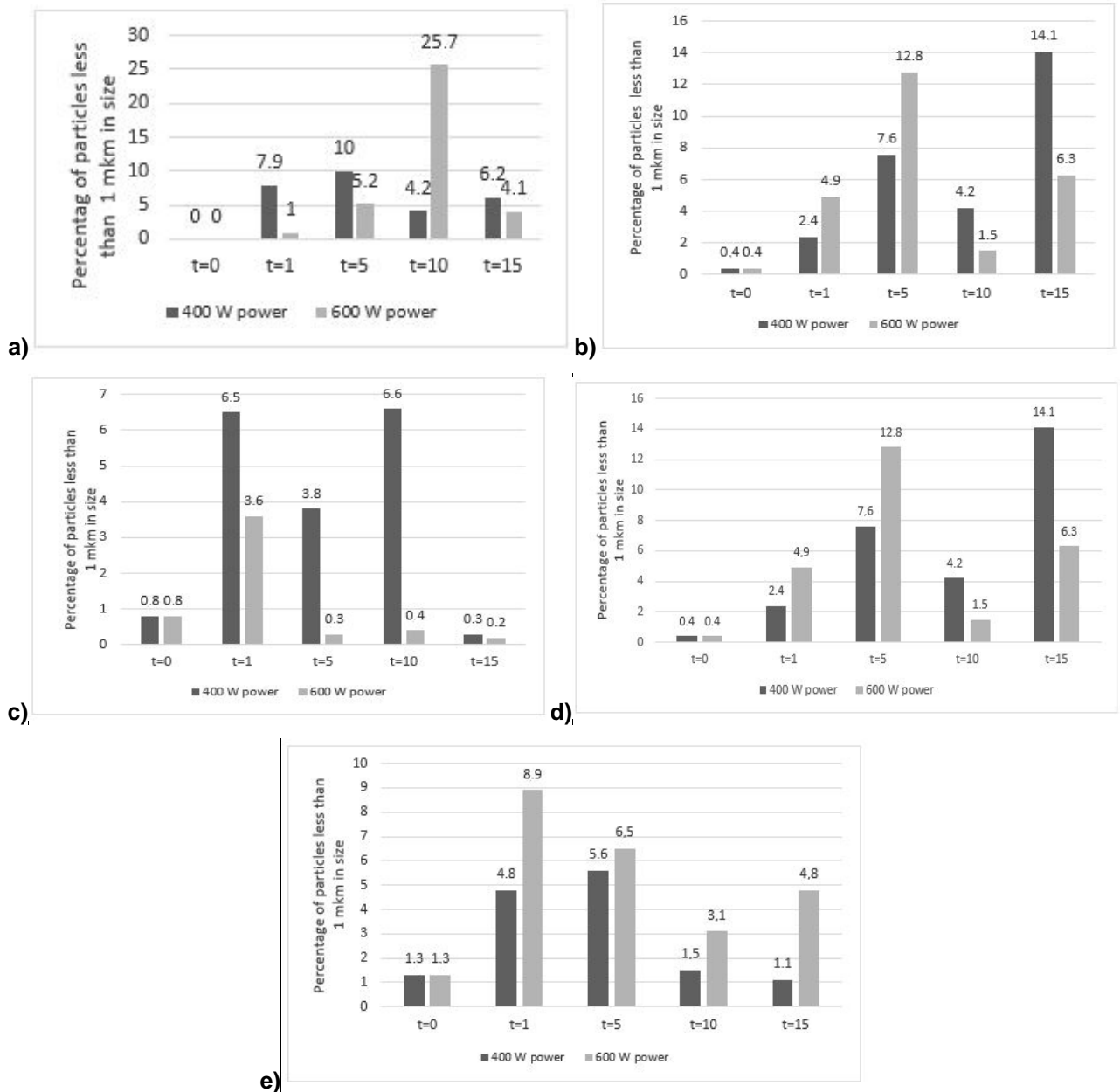


Figure 6. Variation of the contents of particles of various size fractions at different durations and intensities of ultrasonic treatment: a – ash; b – diopside; c – CaCO₃; d – granulated blastfurnace slag; e – wollastonite.

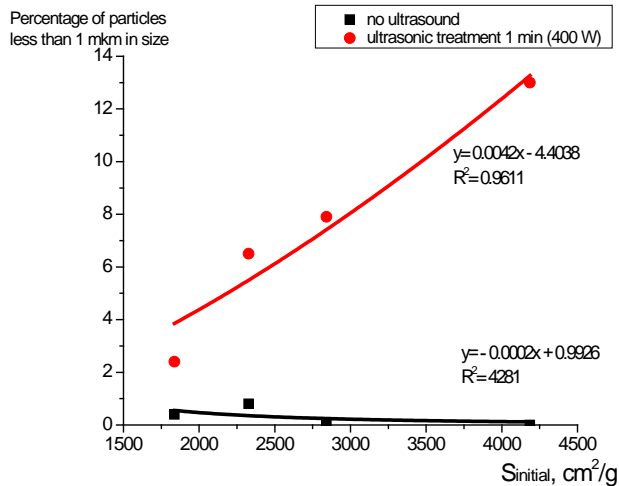


Figure 7. Dependence particle fraction content of less than 1 mm from the original surface area of powders of different genesis and morphology.

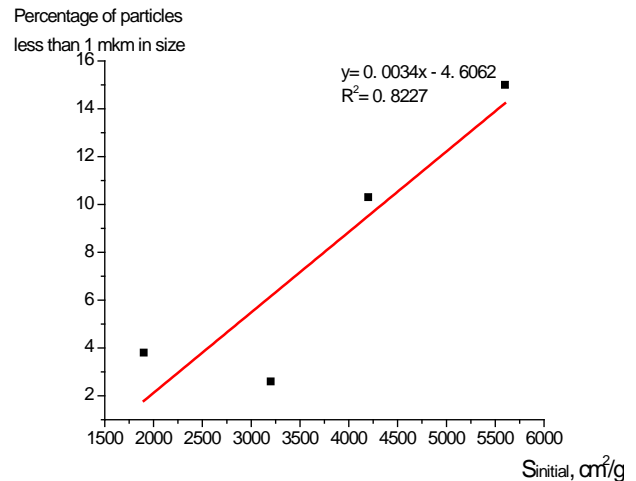


Figure 8. Variation of the content of particles of size fraction less than 1 µm in granulated blastfurnace slag powders of different specific surface areas.

Ultrasonic dispersion and disaggregation can both be classed to the mechanical dynamic activation due to cavitation and due to the mutual friction of rapidly moving and colliding particles. Since the center of a collapsing cavitation bubble is normally situated at some distance from the surface of the solid particles, then, on the adoption of a value of 10^2 – 10^3 MPa [14] for the pressure produced by cavitation-bubble explosion, one can arrive at a conclusion that the stress applied to a powder particle will be two or three orders smaller than the theoretical strength of particle material as determined by the Griffith formula, 10^4 to 10^5 MPa [16]. That is why, in spite of the fact that, because of structural imperfections, the strength of real materials is much lower than its theoretical value, the energy of a cavitation micro-explosion will always be insufficient for the fracture of fine particles containing a low amount of defects. In this connection, we believe that the main process defining the variation of the granulometric composition is, first of all, the disaggregation of powder particles bonded together by autohesion forces and having much a lower strength in comparison with homogeneous particles.

The effectiveness and kinetics of the fracture of particles and their aggregates under conditions of an ultrasonic treatment depends on the intensity of the shock wave and on the velocity of the acoustic flows generated in the medium during the micro-explosion of cavitation bubbles. Presently, two models for cavitation dispersion are known, the fracture of solid particles under the action of shock waves and that under the action of acoustic flows. According to the first model, high-intensity local shock waves ensuring the rise of temperature to 5000 K and the rise of pressure to 100 MPa are generated during micro-explosions of cavitation bubbles. Here, the pressure pulse exerts a most pronounced disturbing action on the particles floating on the surface of cavitation bubbles. That is why a necessary condition for the dispersion of particles in this model is a spherical shape of the gas bubbles at the time of collapsing. The latter is only possible when the diameter of such bubbles will substantially exceed the sizes of the particles and aggregates to be dispersed [14–15, 19].

According to the second model, the dispersion process proceeds due to the collisions of the particles being accelerated, by the cavitation-induced micro-jets, to velocities reaching tens and hundreds meters per second. Previously, calculations performed for powder particles sized 0.1, 0.01, and 0.001 mm [19] have proved the kinetic energy to be sufficient for the fracture of the particles during the collisions; indeed, the generated stresses were in the range from 10 to 10^3 MPa, this values being comparable with the pressure 10^2 – 10^3 MPa produced by a collapsing cavitation bubble.

It should be noted here that the previously obtained data [14–16, 19] show that the cavitation action can simultaneously obey both models. However, depending on the size of dispersed-phase particles and the parameters of the ultrasonic treatment (amplitude and frequency), one of the two models will appear prevailing. For instance, coarser particles will be dispersed due to the cavitation-explosion-induced acoustic flows while the finer particles, due to the intense shock waves (since the pressure pulse due to these shock waves exerts a most pronounced disturbing action only when the dispersed-phase particles float on the surface of the cavitation bubble, the latter in turn being only possible when the sizes of such a bubble will be greater than the particle sizes [20]). In our opinion, an aggregate formed by particles smaller is size than the voids in such an aggregate can be considered as a version of the latter ultrasonic dispersion scheme. In the latter case, the gas-bubble size will be defined by the void size. Accordingly, the ultrasonic-field parameters must ensure cavitation explosions of gas bubbles contained in the voids of such aggregates. Thus, the intensity of the ultrasonic action is to be chosen considering the possibility of ensuring the cavitation of gas bubbles of radius $R_{bubble} = R_{void}$.

With due regard for the fact that the fraction of the particles smaller than 1 μm plays a determining role in the formation of dispersed-phase surface, the choice of the optimum duration of ultrasonic treatment can be made considering an estimate of the energy efficiency of the cavitation disaggregation of powders treated with ultrasound. This efficiency can be evaluated considering the value of the coefficient of the energy efficiency of cavitation dispersion ($K_{en.eff.}$), which can be determined from the formula

$$K_{en.eff.} = E_d / E_{cav.} \cdot 100 \%,$$

where E_d is the energy spent for increasing the specific surface area of the particles smaller than 1 μm during the time t ;

$E_{cav.}$ is the energy consumed for the production of cavitation.

The calculated curve of the energy efficiency factor versus the duration of ultrasonic treatment shown in Figure 9 indicates that the long-term action due to the cavitation leads to a decreased value of the energy efficiency factor. Most probably, the reduction of the efficiency of the ultrasonic treatment is due to the fact that the ultrasonic-curing process of aqueous suspensions is accompanied not only by the dispersion of initial powders and aggregates but, also, by the concomitant formation of new aggregates; on the other hand, according to the definition of the energy efficiency factor, the energy spent for coagulation will pertain to the losses.

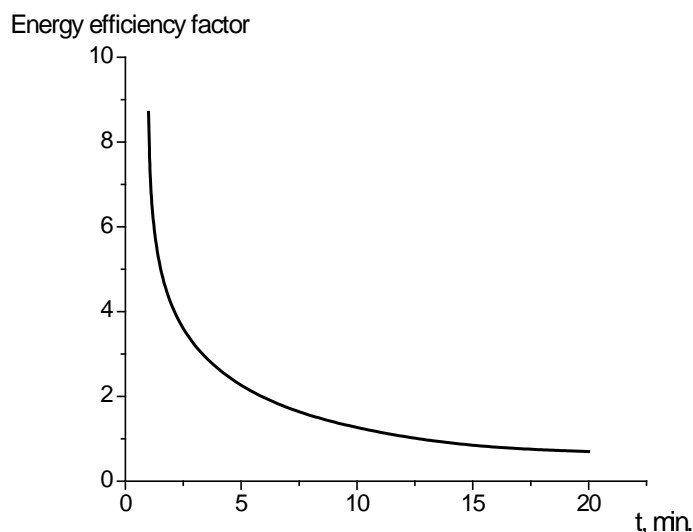


Figure 9. Energy efficiency factor versus the duration of ultrasonic treatment.

Thus, at a relatively small difference between the contents of particles with sizes smaller than 1 μm , the most efficient treatment is the treatment with ultrasound lasting for 1–5 minutes, that is, for the period of the first half-wave of variation of the amount (fraction) of particles smaller than 1 μm in size.

4. Conclusions

The research results showed that, regardless of the genesis and morphology of the particles, by varying the duration of cavitation treatment in powders, it is possible to initiate both a dispersing and aggregating effect. In this regard, time optimization of the processing of powders by ultrasound according to the criterion of maximum disaggregation will increase the potential of such powders as additives to improve the properties of cement composites.

1. Regardless of the time of ultrasonic treatment, the fraction of particles of the most active fraction (less than 1 micron) of wollastonite, chalk, ash, diopside powders, blast furnace granulated slag does not exceed 25 %. Therefore, from the point of view of energy efficiency, it is more preferable to treat these powders with ultrasound within 1–5 minutes, that is, during the first half-wave of a change in the fraction of particles of the fraction $<1 \mu\text{m}$.

2. The ultrasound processing time optimal for a particular powder will depend on the parameters determining the power (intensity) of the ultrasound effect: amplitude, frequency, and volume of the working chamber of the ultrasonic unit.

References

1. Meng, T.Yu.Y., Wang, Z.J. Effect of nano-CaCO₃ slurry on the mechanical properties and micro-structure of concrete with and without fly ash. *Composites part b-engineering*. 2017. Vol. 117. Pp. 124–129.
2. Rassokhin, A.S., Ponomarev, A.N., Figovsky, O.L. Silica fumes of different types for high-performance fine-grained concrete. *Magazine of Civil Engineering*. 2018. 78(2). Pp. 151–160. doi: 10.18720/MCE.78.12
3. Roychand, R., De Silva, S., Law, D. et al. Micro and nano engineered high volume ultrafine fly ash cement composite with and without additives. *International journal of concrete structures and materials*. 2016. Vol. 10. Pp. 113–124.
4. Cherkashin, A.V., Pykhtin, K.A., Begich, Y.E., Sherstobitova, P.A., Koltsova, T.S. Mechanical properties of nanocarbon modified cement. *Magazine of Civil Engineering*. 2017. 72(4). Pp. 54–61. DOI: 10.18720/MCE.72.7
5. Liu, R., Xiao, H., Li, Hi et al. Effects of nano-SiO₂ on the permeability-related properties of cement-based composites with different water/cement ratios. *Journal of materials science*. 2018. Vol. 53. No. 7. Pp. 4974–4986.
6. Roychand, R., De Silva, S., Setunge, S. Nanosilica modified high-volume fly ash and slag cement composite: Environmentally Friendly Alternative to OPC. *Journal of materials in civil engineering*. 2018. Vol. 30. No. 4. Pp. 1–12.
7. Agranat, B.A., Dubrovin, M.N., Khavskii, N.N. *Osnovy fiziki i tekhniki ul'trazvuka*. [Basics of ultrasound physics and engineering]. Moscow: Vysshaya Shkola. 1987. 352 p. (rus)
8. Shangyu, Song, Xia, Zhou, Li, Li, Wuming, Ma. Numerical simulation and experimental validation of SiC nanoparticle distribution in magnesium melts during ultrasonic cavitation based processing of magnesium matrix nanocomposites. *Ultrasonics Sonochemistry*. 2015. Vol. 24. Pp. 43–54.
9. Lesnik, S., Mettin, R., Brenner, G. Study of ultrasound propagation and cavitation activity in a packing bed of spherical particles. *Chemie ingénieurur technik*. 2017. Vol. 89. Pp. 1379–1384.
10. Shakhov, S.A. *Primenenie ultrazvuka dlya intensivatsii protsessa formovaniya (Obzor)*. [Application of ultrasound for intensification of forming processes (Review)]. *Izv. VUZov. Stroitel'stvo*. 2007. No. 5. Pp. 111–118. (rus)
11. Sviridov, D.P., Semenov, I.A., Ul'yanov, B.A. *Zakonomernosi i energeticheskaya effektivnost kavitatsionnogo izmel'cheniya*. [Regularities and energy efficiency of cavitation-assisted atomization]. *Sovremennyeologii. Sistemnyi analiz. Modelirovanie*. 2011. No. 1(29). Pp. 76–81. (rus)
12. Meyers, R.A. (ed). *Encyclopedia of an Analytical Chemistry: Applications. Theory and Instrumentation*. N.Y. Wiley, 2000. 14344 p.
13. Klyuev, S.V., Khezhev, T.A., Pukhareno, Yu.V., Klyuev, A.V. *Fiber Concrete on the basis of composite binder and technogenic raw materials*. *Materials Science Forum*. 2018. Vol. 931. Pp. 603–607.
14. Kuzovnikov, Yu.M. *Intensifikatsiya protsessa razdeleniya emulsii i suspenzii v polyakh monochastotnykh i shirokopolosnykh ultrazvukovykh kolebaniy, Avtoreferat cand. tekhn. nauk* [Intensification of the segregation process of emulsions and suspensions in the fields of high-intensity single-frequency and wide-band ultrasonic oscillations, PhD theses] 05.17.08. Biisk: Polzunov Altai State Techn. University, 2012. 17 p. (rus)
15. Adama Maiga, M., Coutier-Delgosha, O., Buisine, D. Analysis of the critical pressure of cavitation bubbles. *Meccanica*. 2018. Vol. 53. No. 4–5. Pp. 787–801.
16. Bavlabyshko, A.M., Yudaev, V.F. *Rotornye apparaty s modulyatsiei potoka i ikh primeneniye v promyshlennosti* [Flow-modulation rotary apparatus and their application in industry]. Moscow: Nedra, 1992. 172 p. (rus)
17. Fedyuk, R.S., Mochalov, A.V., Timohin, A.M. *Obzor metodov aktivatsii vyazhushchego i betonnykh smesey* [Overview of the methods of activation of binder and concrete mixtures]. *Celi materialovedeniya*. 2018. 5(5). Pp. 916–931.
18. Shakhov, S.A., Pletnev, P.M. *Upravleniye strukturnoi organizatsiei dispersnykh system s pomoshchiyu diskretno-impul'snykh vozdeistviy* [Control of the structural organization of dispersed systems with the help of discrete-pulse energy actions]. *Konstruktsii iz Kompozitnykh Materialov*. 2009. No. 4. Pp. 70–74. (rus)
19. Shakhov, S.A., Rogova, E.V. Disaggregation of ultrafine powders in conditions of ultrasonic cavitation. *Magazine of Civil Engineering*. 2017. 71(3). Pp. 21–29. doi: 10.18720/MCE.71.3
20. Dolinskiy, A.A., Basok, B.I., Gulaj, S.I. i dr. *Diskretno-impul'snyi vvod energii v teplotekhnologiyakh* [Discrete-pulse energy input in thermal technologies]. / A.A. Dolinskii et al. Kiev: Institute of Engineering Thermophysics, Ukraine National Academy of Sciences, 1996. 206 p. (rus)

Contacts:

Sergey Shakhov, +7(383)3280274; sashakhov@mail.ru
 Elena Rogova, +7(913)8957872; elena.rogova4@yandex.ru

© Shakhov, S.A., Rogova, E.V., 2019

14. Кузовников Ю.М. Интенсификация процесса разделения эмульсий и суспензий в полях высокоинтенсивных моночастотных и широкополосных ультразвуковых колебаний: автореферат кандидата технических наук: 05.17.08. Бийск: Алт. гос. техн. ун-т им. И.И. Ползунова, 2012. 17 с.
15. Adama Maiga M., Coutier-Delgosha O., Buisine D. Analysis of the critical pressure of cavitation bubbles // *Meccanica*. 2018. Vol. 53, No. 4-5. Pp. 787–801.
16. Бавлабышко А.М., Юдаев В.Ф. Роторные аппараты с модуляцией потока и их применение в промышленности. М.: Недра, 1992. 172 с.
17. Федюк Р.С., Мочалов А.В., Тимохин А.М. Обзор методов активации вяжущего и бетонных смесей // *Цели материаловедения*. 2018. 5 (5). С. 916–931.
18. Шахов С.А., Плетнев П.М. Управление структурной организацией дисперсных систем с помощью дискретно – импульсных энергетических воздействий // *Конструкции из композитных материалов*. 2009. №. 4. С. 70–74.
19. Шахов С.А., Рогова Е.В. Деагрегация ультрадисперсных порошков в условиях ультразвуковой кавитации // *Инженерно-строительный журнал*. 2017. № 3(71). С. 21–29. doi: 10.18720/МСЕ.71.3
20. Долинский А.А. и др. Дискретно-импульсный ввод энергии в теплотехнологиях. Киев: ИТТФ НАНУ, 1996. 206 с.

Контактные данные:

Сергей Александрович Шахов, +7(383)3280274; эл. почта: sashakhov@mail.ru
Елена Владимировна Рогова, +79138957872; эл. почта: elena.rogova4@yandex.ru

© Шахов С.А., Рогова Е.В., 2019



DOI: 10.18720/MCE.88.3

Polystyrene paint with reduced contents of volatile compounds

V.I. Loganina^a, N.A. Petukhova^a, R.S. Fediuk^b, R.A. Timokhin^b

^a Penza State University of Architecture and Construction, Penza, Russia

^b Far Eastern Federal University, Vladivostok, Russia

* E-mail: roman44@yandex.ru

Keywords: buildings, construction, facades, organomineral additive, polystyrene paint, clay, volatile organic compounds

Abstract. The proposed organomineral additives are novel, eco- friendly components for polystyrene paints. A light brown-red loam was used as a filler for polystyrene paints. Rheological, technological and physico-mechanical properties of paints and coatings based on them were studied by a series of standard tests. Characteristics of frost and water resistance, hiding power and holding capacity of polystyrene paint confirmed the creation of durable paints with high performance properties. Comprehensive studies have shown that the addition of organic additives in the composition of polystyrene paint increases the critical volume concentration of pigment 1.2 times, increases the degree of grinding paint, reduces dispersion time (2 times) and reduces the speed of shelter from 160 to 112 g / m². Analysis of the results of experiments showed that the addition of organic additives contributes to increased resistance to external influences, as well as the strength of adhesion to the substrate by 22 %. Using the obtained results will allow you to create polystyrene paints with a low content of volatile compounds and increased crack resistance.

1. Introduction

Every year more and more stringent requirements are imposed on paints and coatings based on them in connection with the advent of new technologies in industry, construction and the formation of modern aesthetic tastes at the consumer. This applies to both the protective and decorative properties of coatings, which are determined by the physicochemical parameters of all components of the paintwork formulation. In recent years, the demand for high-quality products, characterized by increased durability and lower consumption per unit of the painted area, has increased [1–5]. At the beginning of 21-nd century, three factors had a significant influence on the main directions of development of the global paint industry. First, the tightening of environmental legislation on the content of volatile organic compounds (VOC) in paint and varnish products [6–10]. Secondly, it is the search for substitutes for traditional paints and varnishes, which use organic solvents as a basis (mainly solvents and white spirit, as well as drying oil) [11–16]. Thirdly – the economic factor acting in full force in connection with the tightening of environmental legislation. Its action led to a resurgence of interest in the use of powder paints [17–21]. Trends in the development of materials move in the direction of minimizing the solvent content in paint systems, while achieving professional quality that meets all environmental requirements. The advantages of such paints include, first of all, the possibility of their use at low temperatures, which can significantly increase the seasonality of the finishing works. This group of paints is characterized by the formation of a durable and well adhered to a variety of substrates protective film with high rates of frost resistance.

Especially attractive for the use of polystyrene in the paint industry is the comparative cheapness of this polymer, which is associated with the availability of raw materials, simple manufacturing technology, valuable properties [22–26]. Despite the advantages of polystyrene, it is extremely limited in the paint industry. One of the reasons is its high brittleness temperature, which is 90 °C and is almost close to the glass transition temperature of the polymer. In this regard, the difference between the lower and upper boundaries of the temperature range of operation of the coatings is small, which can cause their cracking at low temperatures.

Loganina, V.I., Petukhova, N.A., Fediuk, R.S., Timokhin, R.A. Polystyrene paint with reduced contents of volatile compounds. Magazine of Civil Engineering. 2019. 88(4). Pp. 25–41. DOI: 10.18720/MCE.88.3.

Логанина В.И., Петухова Н.А., Федюк Р.С., Тимохин Р.А. Полистирольная краска с пониженным содержанием летучих соединений // Инженерно-строительный журнал. 2019. № 4(88). С. 25–41. DOI: 10.18720/MCE.88.3.



This open access article is licensed under CC BY 4.0 (<https://creativecommons.org/licenses/by/4.0/>)

Nanomaterials (pigments, additives) are effective in all types of coatings (organic, water-dispersed, powder). In the case of polymer nanocomposites, nanoparticulate substances are introduced into the polymer matrix. The role of such substances can be performed by organoclays obtained by modifying montmorillonite clays with an organic additive. The chemical composition of clay causes the presence of inorganic cations on the surface of the plates, giving the surface high hydrophilicity and, accordingly, incompatibility with many polymer resins. For successful formation of a clay-polymer nanocomposite, an appropriate surface treatment should be carried out, reducing the polarity of the clay to make the clay «organophilic» [27–31]. Modified clay (organoclay) has several advantages over simple clay: organoclays are well dispersed in the polymer matrix and interact with the polymer chain. The addition of organoclay into the polymer matrix contributes to the improvement of the mechanical properties of polymers and thermal stability. This is achieved by combining the complex properties of organic (lightness, flexibility, plasticity) and inorganic (strength, heat resistance, chemical resistance) materials.

According [32–39], the process of nanocomposite formation proceeds through a series of intermediate stages (Figure 1).

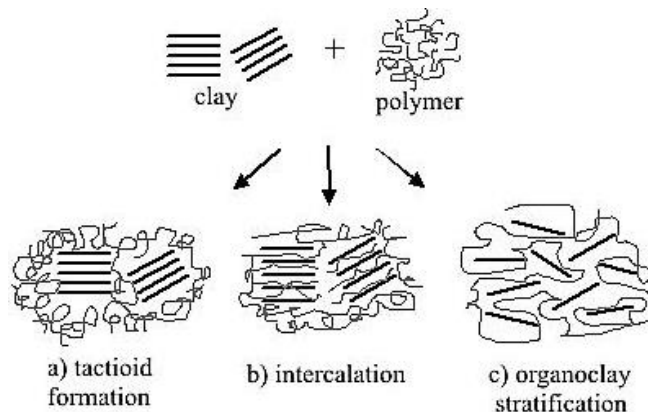


Figure 1. The formation of different morphologies during the dispersion of fillers.

At the first stage, the formation of a tactoid occurs – the polymer surrounds the agglomerates of the organoclay [40–46]. At the second stage (intercalation), the polymer penetrates into the interlayer space of the organic clay, as a result of which the layers expand to 2–3 nm [47–48]. At the third stage (partial exfoliation), partial separation and disorientation of the organic clay layers occurs [49]. At the last stage, peeling occurs [50].

As a scientific hypothesis, a provision has been adopted on the possibility of obtaining an organomineral additive of mixed-layer clay with a high content of montmorillonite. The purpose of this paper is to develop polystyrene paint compositions with a low content of volatile compounds, and coatings based on it, which have enhanced crack resistance.

2. Methods

2.1. Production of organomineral additive

In developing the organomineral additive, clay was used with a specific surface area of 478.3 m²/kg and an average particle size of 5.01 μm. The specific surface area of clay was determined using the PSH-9 device (Granat, Russia).

The main characteristics and chemical composition of clay are listed in Tables 1 and 2.

Table 1. The main characteristics of clay.

| Name of indicator | Value of indicator |
|------------------------------|--------------------|
| Career humidity, % | 20–24 |
| Plasticity coefficient | 14.3 |
| Total shrinkage, % | 5.1 |
| Hygroscopic moisture, % | 3.31 |
| Particle size (% by volume): | |
| clayey | 11.9–15.8 |
| sandy | 30–35 |
| dusty | 49–59 |

Table 2. The chemical composition of clay.

| CaO | SiO ₂ | Al ₂ O ₃ | Fe ₂ O ₃ | MgO | SO ₃ | LOI |
|------|------------------|--------------------------------|--------------------------------|------|-----------------|-------|
| 3.24 | 65.50 | 9.54 | 7.72 | 0.76 | 0.06 | 11.40 |

As an organic component, several additives were used: sulfanol, Melflux 1641F (BASF, Germany), Melment F15G (BASF, Germany), as well as additives OP-4 and OP-10 (Himbyt, Russia), which are products

of processing a mixture of mono- and dialkylphenols with ethylene oxide and used as wetting and emulsifying surfactants

The plasticizer concentration was determined by changing the surface tension of the plasticizer solution, which was determined by the drip method and was calculated by the formula (1):

$$\sigma = \sigma_s \frac{n_s}{n}, \quad (1)$$

where σ_s is a surface tension of the solvent;

n_s is amount of solvent droplets in 1 ml;

n is number of drops of the solution in 1 ml.

To reduce the time for the manufacture of organomineral additive, it was proposed to prepare the organoclay in a solvent, which was later used to prepare paint formulations.

To determine the amount of surfactant adsorption on the clay surface under the condition $\sigma = \text{const}$, clay was added to the resulting solution; the solution was mixed and settled for 10 minutes. The time required for the complete adsorption of the OP-4 and OP-10 additives on the clay was determined by the kinetics of changes in the surface tension of the solution. After clay deposition, the surface tension was again checked.

2.2. Design of polystyrene varnishes

For the preparation of polystyrene varnishes were used coal solvent (Severstal, Russia) and oil solvent (Neft, Russia), with equal density of 860 kg/m³. High impact polystyrene (Salavatnefteorsintez, Russia) was also used. Titanium dioxide, ocher, iron oxide, chromium oxide were used as pigments. Colored sand (Nizhne-Abyazovskoye deposit, Russia), Omyacarb (Vapenna, Czech Republic), microdolomite (Dolomit, Russia) were used as fillers. Telaz (Avtokoninvest, Russia) was used as a wetting agent. It is an amino acid of vegetable oils, visually a viscous flowing brown liquid, with an amine value of at least 30 mg; is introduced before the dispersion process in the calculation of 5 g per 1 kg of paint.

2.3. Evaluation of the rheological, technological and physicomachanical properties of paint materials and coatings based on them

Conditional viscosity of paint and varnish compositions was determined using a VZ-4 viscometer (Zapadpribor, Russia). The method is based on determining the duration of the expiration (in seconds) of 100 ml of polymer solution through a nozzle with a diameter of 4 mm. The dynamic viscosity of the compositions was also determined using a VZ-4 viscometer. The method is based on the fact that two liquids whose densities ρ_1 and ρ_2 , with dynamic viscosity η_1 and η_2 , of one volume flow under the action of gravity through the same tube in time t_1 and t_2 . This process is described by an equation that follows from the Poiseuille law for laminar fluid flow through capillaries, and has the form:

$$\frac{\eta_2}{\eta_1} = \frac{t_2 \cdot \rho_2}{t_1 \cdot \rho_1}, \quad (2)$$

where η_2 is the dynamic viscosity of the test solution, Pa · s;

η_1 is dynamic viscosity of water, Pa · s;

t_2 is time of leakage of the test solution, s;

t_1 is time of outflow of water, s;

ρ_2 is density of the test solution, g/cm³;

ρ_1 is water density, g/cm³.

The value of the dynamic viscosity of the studied finishing composition was calculated on the basis of equation (2), according to the formula (3):

$$\eta_2 = \eta_1 \cdot \frac{t_2 \cdot \rho_2}{t_1 \cdot \rho_1}. \quad (3)$$

The determination of spreadability was carried out according to the follow procedure. Paint with a working viscosity is applied to a metal plate measuring 20 × 40 cm and quickly (no more than 2–3 minutes) distributed by longitudinal and transverse movements of the brush over the entire surface. Then the brush sharply conducts a deep stroke in the middle of the plate from one edge to the other and mark the time when the brush strokes disappear and the surface becomes completely flat. Depending on the time required for the

«filling» of the paint, there are three estimates: 1 – satisfactory (no later than 10 minutes); 2 – slow (10–15 minutes); 3 – unsatisfactory (more than 15 minutes).

The mass fraction of non-volatile substances NV , %, was determined as follows. A paint material was poured into a flat-bottomed metal cup of size 70×110 mm, weighed and evenly distributed along the bottom. Then the paint was dried in a drying oven to constant weight. The mass fraction of non-volatile substances was determined by the formula (4):

$$NV = \frac{(m_2 - m_0)}{(m_1 - m_0)} \cdot 100, \quad (4)$$

where m_2 is a mass of the cup with the dried residue, g;

m_0 is a mass of an empty cup, g;

m_1 is a mass of the test specimen cup, g.

The surface roughness R_a of the coatings was measured using a portable device profilograph TR100 (Time, China), which is based on the principle of feeling the surface of the coating with a diamond needle with a small radius of curvature and the transformation of needle vibrations into voltage changes proportional to these fluctuations.

To assess the adhesion strength, the method of tearing stamp was used (normal tear). The method consists in measuring the force required to detach the coating from the concrete surface with the help of a glued metal stamp of a cylindrical shape with a diameter of 18 mm. The separation force was measured using a dynamometer. Epoxy glue was used to glue the dies to the coating. The adhesion strength of the paint with the substrate R_{adh} was determined by the formula (5):

$$R_{adh} = \frac{P}{F}, \quad (5)$$

where P is a force of detach, N;

F is contact area of the stamp with the paint coating, m^2 .

The tensile strength (cohesive strength) was determined on a tensile testing machine IR 5057-50 (Avtomatika, Russia). The method is based on the tensile test specimen size of 0.7 × 10 × 50 mm to rupture at a deformation rate of 1 mm/min. Specimens of the films were fixed in the clamps of the tensile machine so that its longitudinal axis was located in the direction of tension, and the applied forces acted uniformly over the entire cross section of the specimen. The tests were carried out at air temperature $t = 20 \pm 2^\circ\text{C}$ and relative air humidity $\varphi = 64\%$.

The calculation of tensile strength was carried out according to the results of testing six specimens of each composition. The tensile strength σ_t for each specimen was calculated by the formula (6):

$$\sigma_t = \frac{F_{ti}}{S_{0i}}, \quad (6)$$

where F_{ti} is tensile load at the moment of rupture, N;

S_{0i} is a initial cross-sectional area of the specimen, m^2 .

The elastic modulus was calculated according to the stress-strain diagram (Figure 2) using the tangent of the angle of inclination to the abscissa axis of the tangent (Z), conducted to the initial straight section of the diagram.

The elastic modulus for each specimen E_i was calculated by the formula (7):

$$E_i = \frac{\sigma'_i}{L'_i} \cdot 100. \quad (7)$$

where σ'_i is the tensile strength at the moment of detach of the tangent from the stress-strain diagram, MPa;

L_i is relative elongation at break, %.

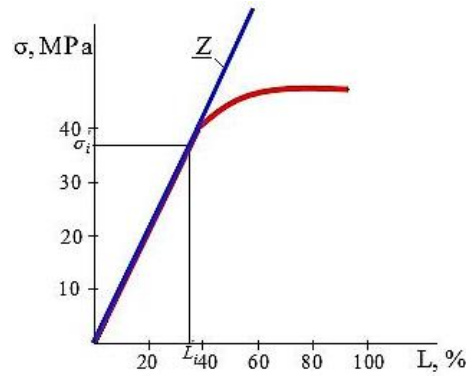


Figure 2. The stress-strain diagram.

The method of measuring internal stresses was as follows. On the disc of aluminum foil with a diameter of 120 mm and a thickness of 0.01 mm applied colorful compositions. A strain gauge with a 50 mm base was glued on the free side of the disk, the readings of which were recorded with an automatic strain gauge based on a digital strain gauge bridge. The value of the stress was determined by the formula (8):

$$\sigma_o = 2 \frac{(1 - \mu_1) \cdot h_2}{h_1} \cdot E_2 \cdot \varepsilon, \quad (8)$$

where μ_1 is Poisson's ratio of paint;

h_1 and h_2 are the thickness of the substrate and the paint coating, m;

E_2 is elastic modulus of the substrate, MPa;

ε is relative deformation of the substrate.

The milling degree was determined by the depth of the Klin device (Grindometer, Russia) groove (in μm) corresponding to the border of a significant amount of individual particles and aggregates of pigments and fillers visible on the surface of the layer of the test material or border the beginning of strokes from them.

The vapor permeability of the coatings was determined using a method based on determining the amount of water vapor that passed through 1 cm^2 of the free-film surface over a period of time at a temperature of 20 ± 2 °C. On the sides of the glass, in which 100 % relative humidity was created, was placed gauze (3 layers) with dried paint, smeared on the edges with paraffin. Periodically the glass was weighed until such time as the weight of the glass with the film did not become constant. The relative humidity of the air in the room was determined using a psychrometer and was 66 %. The coefficient of vapor permeability was calculated by the formula (10):

$$\mu = \frac{P \cdot \delta}{(e_1 - e_2) \cdot S \cdot \tau}, \quad (10)$$

here P is the total amount of water vapor passed through the film, corresponding to the increase in film mass during the test, mg;

σ is film thickness, m;

S is film area, m^2 ;

τ is test duration, h;

e_1 is water vapor elasticity, Pa (at $\varphi = 100$ %);

e_2 is water vapor elasticity, Pa (at $\varphi = 66$ %).

Resistance to vapor permeability, $\text{m}^2 \cdot \text{h} \cdot \text{Pa}/\text{mg}$, was determined by the formula:

$$R_v = \frac{\delta}{\mu}, \quad (11)$$

here δ is the film thickness, m;

μ is the estimated coefficient of vapor permeability of the material, $\text{mg}/(\text{m} \cdot \text{h} \cdot \text{Pa})$.

The covering power of the paint film was determined as follows. On a pre-weighted glass plate with a size of 200×200 mm put a colorful composition. Then a chessboard was put under the glass plate with the applied paint and with scattered reflected daylight it was observed whether the black and white squares of the chessboard been seen. Covering power (g/m^2) was determined by the amount of paint (in g), followed by coloring the surface of 1 m^2 .

The holding capacity of the paint was determined using filter paper. On a filter paper placed on the glass (to avoid additional moisture absorption by the base under the paper), a drop of paint was applied. After 2–3 minutes, the diameter of the drop d_d and the diameter of the wet spot around the drop d_s were measured. The holding capacity of paints was expressed in percent and was determined by the ratio of the diameter of a drop of paint to the diameter of the print of the solvent $d_d/d_s \cdot 100 \%$.

The water resistance properties of paint and varnish films were evaluated by the change in the quality of the appearance of the coatings under the action of water. Cement-sand specimens on one side were painted with paint, and on the sides they were treated with paraffin and placed in water. Two hours after removal from the water and air drying, the coatings were inspected and the appearance of white opaque spots, rashes, bubbles, wrinkles, and exfoliation was evaluated. The protective properties of polystyrene coatings were also evaluated by the rate of water penetration through the coating. On painted cement samples were installed flasks with water, treated with clay on the edges. At intervals of time, the amount of water that passed through the coating was measured, and the rate of moisture penetration was plotted against time.

Tests for frost resistance coatings were held in the following mode. Specimens of the cement-sand mortar stained with the proposed composition after saturation in water were placed in a freezer with a temperature of $-15 \text{ }^\circ\text{C}$ and kept for 4 hours, after which they were placed in water with a temperature of $18\text{--}20 \text{ }^\circ\text{C}$ for four hours (one cycle).

2.4. Determination of particle size distribution and sedimentation of clay

The determination of the granulometric composition of clays is based on the ability of clay particles to swell in water and at different rates of falling of particles in water depending on their size (sedimentation, or sedimentation rate). Sedimentation analysis is based on observations of the sedimentation rate of particles of the dispersed phase under the action of either gravity or centrifugal force (for systems in which the dispersed phase settles very slowly). The studied powder weighing 1 g was placed in a cylinder with a clean dispersion medium, then stirred evenly by a glass rod with a rubber disk attached at the bottom. Stirring was carried out for 3–5 minutes only in the vertical direction. When mixing, they made sure that no large lumps were left and no air bubbles were formed, as a result of too intensive mixing. After the suspension was thoroughly mixed, the cup was quickly lowered into it to accumulate sediment and hung on the balance arm at height H from the surface of the suspension. Further, sequential measurements were made of the weight of the precipitate during the sedimentation of the suspension using torsion weights device at the following time intervals: 1; 1.5; 2; 2.5; 4; 5; 7.5; 15; 25; 40 (time was taken in minutes).

2.5. Microscope image

The microstructure of clay was examined by polarizing microscope MIN-8 (Scopica, Russia). The microscope is designed to study transparent objects in transmitted ordinary or polarized light with conoscopic and orthoscopic rays.

When using the illuminator on a microscope, studies of opaque objects in reflected polarized and ordinary light were made.

3. Results and Discussion

3.1. Characterization of organomineral additive

It has been established (Figure 3) that with an increase in the concentration of plasticizers, the value of the surface tension decreases to a certain value.

When the concentration of sulfanol and Melment F15G is more than 0.2 %, OP-4 additives – 0.3 %, Melflux 1641F is higher than 0.05 %, stabilization of surface tension values is observed. Thus, the surface tension of a solution with additives at their optimum content is: with sulfanol $\sigma = 29.1$, OP-4 $\sigma = 30.1$, Melment F15G $\sigma = 64.7$, Melflux 1641 F $\sigma = 60.2$. Consequently, sulfanol and OP-4 additives have a more plasticizing effect in water.

It is established that the value of adsorption of the OP-4 and OP-10 additives on the clay is $0.38 \text{ mg}/\text{cm}^2$ and $0.17 \text{ mg}/\text{cm}^2$, respectively (Figure 4).

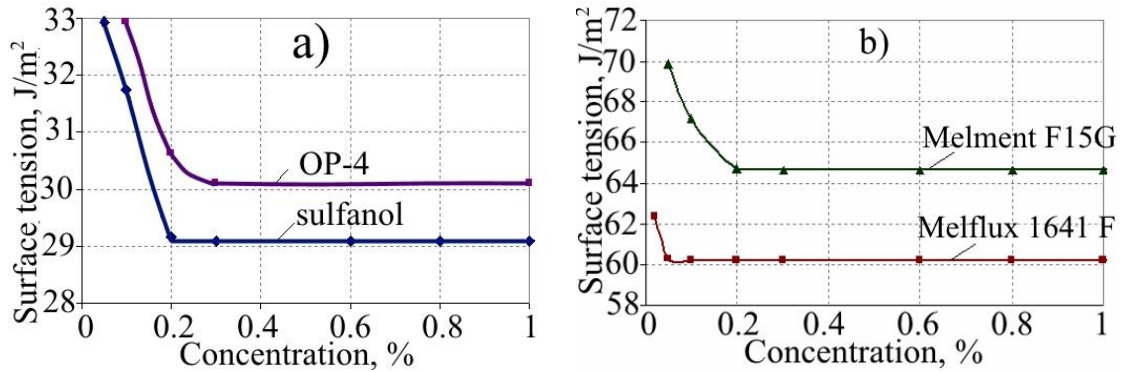


Figure 3. The dependence of the surface tension on the concentration of the additive in water.

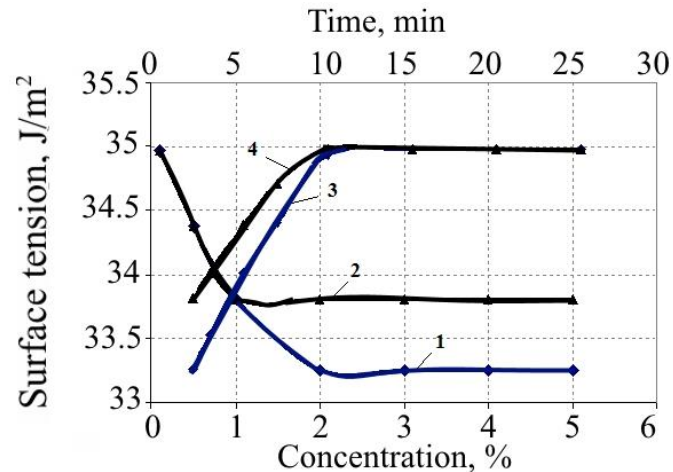


Fig. 4. Dependence of surface tension on concentration additives in the solvent (1, 2) and adsorption time (3, 4): 1, 3 – OP-4; 2, 4 – OP-10.

The subsequent formulation of a solution of polystyrene varnish took into account the amount of the additive adsorbed on the clay.

It has been proposed 2-stage addition of colored filler in the paint composition:

- preliminary mixing of a part of the solvent, OP-4 additives and part of the filler (production of organoclay);
- the subsequent addition of the remaining amount of varnish (solvent and polystyrene) and filler, followed by stirring.

The step-by-step addition of the filler in the mixture with the addition of OP-4 ensures that, at the first stage, in solution of the solvent, the organomineral additive due to the adsorption of the surfactant additives on the surface of clay particles which contained in the colored filler.

The results of the research indicate that the modified clay has a more finely dispersed structure compared to natural clay (Figure 5).

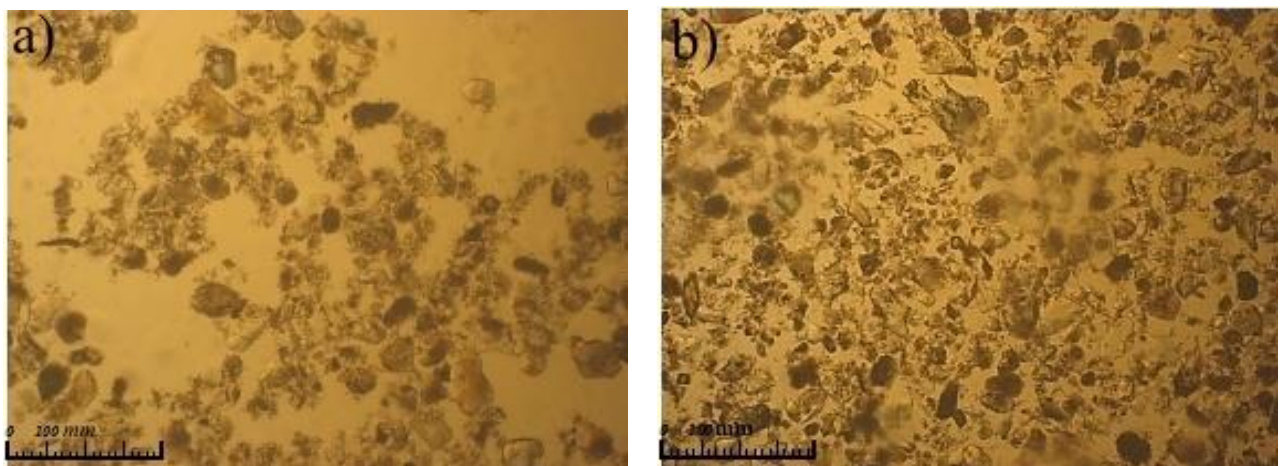


Figure 5. Images of natural (a) and modified (b) clay.

Were developed 2 methods of introducing organoclay in the composition of the paint. In the first method, the technology for preparing a solution with organoclay was as follows. In the solvent, which is used in the preparation of varnish, was introduced additive OP-4. In the resulting solution was added clay in an amount of 2 % by weight of polystyrene. In the second method of lacquer preparation, organoclay obtained in dry form was introduced into the polystyrene melt, which was then used to prepare the lacquer. It has been established that the method of introducing organoclay into the paint leads to a change in the physicochemical properties of films based on polystyrene varnish. The strength of polystyrene films with organoclay is higher than the controls by 40–45 % with the first method of preparing varnish and 11 % with the second method of introducing organoclay. Due to the high physicochemical properties, the first method of introducing organoclay into the paint composition was used in the future.

3.2. Determination of the optimal polymer and pigments concentration

In the course of determining the optimal polymer content by changing the viscosity of the polystyrene solution, depending on its concentration in the solvent, it was revealed that the critical concentration of the polystyrene solution in the solvent is 15 %. For further research, the concentration of polystyrene in the solution was 10–15 %.

During the determination of the volume content of pigment in paintwork formulations prepared on the basis of a 10 % solution of polystyrene in solvent, it was found that with the addition of organomineral additives, the values of the critical volume concentration of pigment (COCP) increase compared with the control compositions regardless of the type of pigment (Table 3).

Table 3. The values of the critical volume concentration of pigments.

| Composition | COCP | | | |
|---------------------------------|-----------------|-------|-------------|----------------|
| | TO ₂ | Ocher | Iron minium | Chromium oxide |
| control | 0.081 | 0.068 | 0.083 | 0.054 |
| with OP-4 | 0.085 | 0.071 | 0.088 | 0.060 |
| with organoclay, modified OP-4 | 0.091 | 0.076 | 0.093 | 0.063 |
| with OP-10 | 0.087 | 0.072 | 0.090 | 0.061 |
| with organoclay, modified OP-10 | 0.095 | 0.076 | 0.096 | 0.078 |

At the optimal content of organomineral additives modified by OP-4 and OP-10, an increase in the values of COCP is observed. So, the values of COCP are equal at a control composition of 0.081, for compositions with organoclay – 0.091 and 0.095, which is 12.3 and 17.3 %, respectively.

The optimal degree of filling of polymer composites, calculated on the basis of structural and topological parameters. The results of calculating the consumption of pigments are listed in Table 4.

Table 4. The results of calculations of the consumption of pigments and filler, depending on the topological parameters.

| Pigments and filler | Specific surface area, S_{sp} , m ² /kg | Average particle size, d_a , μm | Bulk density ρ_b , kg/m ³ | True density ρ_t , kg/m ³ | Volume of pigment particles, V , units of volume | Volume of monolithic pigment particles, V_m , units of volume | The volume of the film forming solution, V_f , units of volume |
|--------------------------------|--|-----------------------------------|---|---|--|---|--|
| TiO ₂ , R-2 brand | 467.92 | 3.20 | 650 | 4000 | 0.340 | 0.054 | 0.946 |
| TiO ₂ , CR-02 brand | 2053.03 | 0.73 | 757 | 4000 | 0.040 | 0.008 | 0.992 |
| Ocher | 1128.83 | 1.83 | 730 | 2900 | 0.182 | 0.046 | 0.954 |
| Iron minium | 750.53 | 2.04 | 1072 | 3900 | 0.209 | 0.057 | 0.943 |
| Chromium oxide | 1012.64 | 1.13 | 882 | 5210 | 0.089 | 0.015 | 0.985 |
| Colored sand | 114.40 | 21.00 | 1309 | 2660 | 0.883 | 0.435 | 0.565 |

3.3. Effect of organoclay to pigment dispersibility

Modification of clay with the addition of OP-4 leads to a significant increase in its dispersion due to the loosening effect on the structure of layered aluminosilicate, which helps in the process of dispersing in the manufacture of paint to obtain a higher degree of milling at lower energy costs (Figure 6).

It has been established that in paints with organoclay, a milling degree of 23 μm was obtained after 15 minutes of dispersion, and in a control composition (without organoclay), a degree of milling, equal to 25 μm, after 30 minutes. For comparison, Russian organobentonite was introduced into the composition of polystyrene paint. In the composition with organobentonite, a milling degree of 25 μm was obtained after 20 minutes of dispersion.

The addition of the organomineral additive leads to a decrease in the hiding power of the paint from 160 to 112 g/m², which is an indirect confirmation of the greater dispersion of the paint.

An additional confirmation of the finely dispersed structure is the experimental data obtained by us on the saturation of the color of the coatings. To describe the color, the HSB color model was used (H is a color tone, S is a saturation, B is a brightness). It is shown that the use of organomineral additive leads to an increase in color saturation from 0.875 to 0.906, i.e. by 3.4 % (while maintaining the values of H and B). Compared with the experimental data of other researchers [2, 8, 10], the shown increase in color saturation is a definite advantage.

3.4. Study of the kinetics of curing coatings

Solvent volatility is one of its most important characteristics. From the speed with which the solvent will evaporate from the surface of the paint film, such characteristics as lightness of feathering the paint, spreading, drying time from «dust» and «full drying», crack resistance, tensile strength depend. The study of the kinetics of solvent evaporation was carried out on paint formulations based on 10 % solutions of polystyrene (Figure 7).

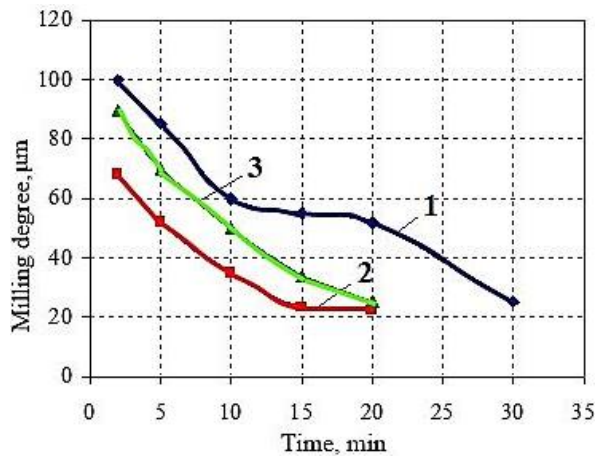


Figure 6. The dependence of the milling degree on the duration of dispersion: 1 – control (without additives); 2 – with organoclay; 3 – with organobentonite.

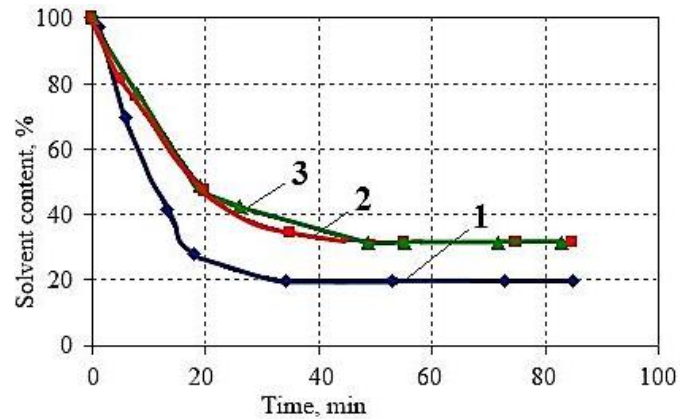


Figure 7. Kinetics of solvent removal from polystyrene paintwork: 1 – control (without additive); 2 – with organoclay; 3 – with organobentonite.

It has been established that at the first stage of coating formation an intensive evaporation of the solvent is observed, leading to a sharp decrease in the weight of the polymer coating. The addition of organomineral additives and organobentonite leads to a slow rate of evaporation of the solvent. In connection with this, the content of volatile compounds decreases in the coloration zone, which makes it possible to increase environmental safety during paint work. In the first 6 minutes of curing the polymer coating, the loss of solvent was 30.56 % for the control composition (without the additive), 18.65 % and 20.12 % for coatings with organobentonite and organic clay, respectively. The content of non-volatile substances of polystyrene paint based on 10 % varnish after 80 minutes of curing is 20 % for the control composition, and 34 % for the composition with organoclay. When using colored sand, the dry residue is 74 %.

It was established that the drying time of coatings to degree 3 on a glass substrate for a control composition is 18 minutes, for compositions with organoclay – 36 minutes; on the cement-sand substrate at the control composition 7 minutes, for compositions with organoclay – 10 minutes. At a negative temperature ($T = -10 \pm 2$ °C) of the cement-sand substrate and a positive paint temperature ($T = 20 \pm 2$ °C), the drying time of coatings based on the control and modified compositions remains almost unchanged. The use of colored filler paint in the formulation leads to a significant increase in the drying time of the coatings.

The slowed down rate of drying of coatings based on modified polystyrene paint leads to a change in its stress state during the curing process. The study of internal stresses in the process of curing the coatings was carried out on paint-and-lacquer compositions with an optimal pigment content (titanium dioxide) at air temperature $T = 20 \pm 2$ °C and relative air humidity $\varphi = 60-65$ %. It was established that the growth of internal stresses occurs within 15 minutes, while the evaporation of the solvent was for coatings without additives – 72.22 %, with organoclay – 53.13 %, with organobentonite – 51.43 %. The maximum values of internal stresses are typical for coatings based on control compositions and were $\sigma = 0.05$ MPa, with organoclay – 0.016 MPa, with organobentonite – 0.041 MPa. Stress relaxation is observed after 26–30 minutes. The residual values of the internal stresses in the coatings on the basis of the control composition were $\sigma_o = 0.006$ MPa, on the basis of the composition with organoclay – 0.005 MPa, on the basis of the composition with organobentonite – 0.013 MPa. Compared to experimental studies of internal stresses obtained by other researchers [36, 43, 48], it decrease of an average of 25–30 % is noted.

3.5. Physical and mechanical properties of varnish films

To study the patterns of change in the deformative properties of coatings based on modified polystyrene paint, free films based on 10 % polystyrene varnish were examined (Table 5).

Table 5. Physical and mechanical properties of varnish films.

| Method of organoclay introduction | Composition | Breaking strength σ_b , MPa | Elastic modulus E , MPa | Elastic deformations ε | Plastic deformations ε_p | Relative deformations ε_r |
|-----------------------------------|-----------------------------|------------------------------------|---------------------------|------------------------------------|--------------------------------------|---------------------------------------|
| First method | Control | 5.24 | 750 | 0.56/0.14 | 3.37/0.86 | 3.93/1 |
| | Organic clay based on OP-4 | 9.62 | 950 | 0.79/0.28 | 2.01/0.72 | 2.80/1 |
| | Organic clay based on OP-10 | 8.62 | 810 | 0.90/0.23 | 3.10/0.77 | 4.00/1 |
| Second method | Organic clay based on OP-4 | 5.91 | 850 | 0.65/0.24 | 2.05/0.76 | 2.70/1 |

Note. Above the line, the values of film deformations are given in %, and below the line, the fractions of elastic deformation in the total deformation.

An increase in the elastic deformations of the specimens of films prepared on the basis of compositions using organic clay has been established. Thus, in the control specimens, the elastic deformations amounted to 0.56 %, in the films based on compositions with an organomineral additive modified by OP-4, the elastic deformations increased and amounted to the first method of addition $\varepsilon = 0.79$ % and the second method of addition $\varepsilon = 0.65$ %.

It is shown that with the addition of the organomineral additive polystyrene films have higher values of elastic modulus. In the first method of introducing organoclay, the elastic modulus of the specimens is $E = 950$ MPa, in the second method of preparing varnish, the elastic modulus $E = 850$ MPa, while in the control one $E = 750$ MPa. The addition of organoclay modified with the addition of OP-10 also leads to an increase in the elastic modulus $E = 810$ MPa.

The reduction of internal stresses in the coatings based on the modified paint and the increase in its cohesive strength contribute to the improvement of their crack resistance. Crack resistance was evaluated by the coefficient of crack resistance, which was determined as the ratio of the internal stresses of the coatings to the tensile strength of the films. It was revealed that the use of organic additives in the formulation of polystyrene paint leads to an increase in crack resistance by 2 times compared with the control composition (without additives).

Addition to the formulation of polystyrene paint organomineral additives reduces the time of flowing property from 10 to 3–4 minutes, increasing the holding capacity by 13 %, which contributes to a better applicability of paint on cement surfaces and improve the quality of the appearance of coatings, which were evaluated, as well as in terms of surface roughness. It is revealed that the surface roughness of the coating based on the control composition is $R_a = 0.74$ – 1.2 μm , and the surface roughness of the coatings based on the composition with organic clay are $R_a = 0.4$ – 0.6 μm .

The addition of organic additives leads to an increase in adhesion strength by 22 %. The adhesive strength of the control specimen was 1.88 MPa, and with organoclay – 2.42 MPa. Replacing 5 % of the titanium dioxide pigment with Omycarb fillers and microdolomite leads to a decrease in the adhesion strength of the coatings to the substrate by 4.5 and 12 % compared with the composition without filler. It was studied the effect of the addition of organomineral additives on the water resistance of coatings, which was determined by the kinetics of moisture penetration through the coating, as well as by the change in the quality of the appearance of the coatings after 24 hours in water. It was established that the presence of organoclay in the formulation of paint helps to reduce the rate of penetration of moisture. The maximum speed of moisture penetration through the coating is after 72 hours for formulations with organogline of 0.0057 mg/h, and for the control composition (without organoclay) – 0.0125 mg/h. The maximum moisture penetration rate is characteristic of coatings based on paint with a filler, which characterizes a more porous structure of the coating. This is confirmed by the results of studying the porosity of paint coatings. It was revealed that the replacement of 5 % titanium dioxide by microdolomite leads to an increase in large pores of the coating. The relative total porosity with an equivalent radius of 50 to 99 μm was 54.8 % for the composition without filler and 56.0 % for the composition in which part of the pigment was replaced with microdolomite.

It is shown that the coatings based on the control composition (without organoclay) have a color change, appearance of stains, rash on 20 % of the surface after 288 hours in water, while the coating on the basis of the composition with an organomineral additive changes color without showing surface defects occurred only

after 512 hours of testing. The addition of fillers in the formulation of the paint composition contributed to a certain decrease in the waterproof properties of the coatings. Discoloration, the appearance of spots and rashes on the surface of the coatings appeared only after 360 hours of testing (for formulations with microdolomite) and 312 hours (for formulations with Omyacarb).

The presence of organic additives in the formulation of polystyrene paint leads to a change in the hydrophysical properties of coatings.

The resistance to vapor permeability of the control composition (without an organomineral supplement) was $R_v = 6.40 \cdot 10^5$, and with organic clay $R_v = 8.50 \cdot 10^5$. The resistance to vapor permeation of polymer coatings based on paints filled with microdolomite and Omyacarb are almost 1.5 times lower than the resistance to vapor permeation of polymer films based on paints without filler.

Addition to the formulation of paint organic supplement leads to an increase in the frost resistance of coatings. Coatings based on the control composition collapsed after 112 cycles of alternate freezing and thawing. Coatings based on the composition with organoclay after 160 cycles collapsed.

Based on comprehensive studies, an optimal formulation of polystyrene paint with an organomineral additive based on clays from local quarries has been developed. Table 6 shows the formulation of polystyrene paints with a rational content of pigment and filler.

Table 6. Formulations of polystyrene paints.

| Components | Composition of polystyrene paints (wt. %) | | | | |
|---------------|---|-----------------------------|-------|-------|-------|
| | control | with organomineral additive | | | |
| | | I | II | III | IV |
| Polystyrene | 7.9 | 7.8 | 7.8 | 7.8 | 4.5 |
| Solvent | 70.7 | 70.4 | 70.4 | 70.4 | 25.8 |
| Pigment | 20.9 | 21.3 | 20.23 | 20.23 | – |
| Color sand | – | – | – | – | 68.94 |
| Microdolomite | – | – | 1.07 | – | – |
| Omyacarb | – | – | – | 1.07 | – |
| Clay | – | 0.2 | 0.2 | 0.2 | 0.09 |
| Additive OP-4 | – | 0.3 | 0.3 | 0.3 | 0.17 |
| Telaz | 0.5 | – | – | – | 0.5 |

Table 7 shows the comparative characteristics of polystyrene paints of the control composition (without additives) and composition with organoclay.

Table 7. Exploitational properties of polystyrene paints and coatings based on them.

| Indicator | Control | I | II | III | IV |
|--|--|--|---|-------|--|
| Relative viscosity, s | 15–20 | 25–30 | 25–30 | 25–30 | 140–160 |
| Drying time at (20±2) °C, min, not more than | 7–9 | 10–12 | 9–12 | 8–10 | 12–14 |
| Milling degree, μm, not more | 50 | 22 | 25 | 25 | – |
| Resistance to static exposure to water at (20±2) °C, h, not less | 48 | 72 | 48 | 48 | 24 |
| Resistance to vapor permeability $R_v \cdot 10^{-5}$, m ² ·h·Pa/mg | 6.4 | 8.5 | 5.8 | 6.0 | 4.2 |
| Adhesion strength, MPa | 1.88 | 2.42 | 2.11 | 2.31 | 1.36 |
| The nature of the surface finishing layer | smooth | | | | textured |
| The quality of the external coating after 500 hours of moisturizing | loss of luster up to 50 %, dis-coloration, haziness, significant dirt retention, cracks or surface meshes, visible to the naked eye, flaking, no bubbles | loss of luster up to 5 %, color change is barely noticeable, haze is absent, grinding is barely noticeable, weathering, cracking, bubbles and exfoliation are absent | loss of gloss up to 20 %, dis-coloration, bronzing, haze, dirt retention are in-significant | IV.7 | loss of luster up to 50 %, dis-coloration, haziness, significant dirt retention, cracks or surface meshes, visible to the naked eye, flaking, no bubbles (after 200 h) |
| Covering power, g/m ² | 160 | 112 | 142 | 110 | – |
| Frost resistance, cycles | 112 | 160 | 138 | 132 | 18 |

Thus, the use of colored filler in the formulation of polystyrene paints gives the surface of coatings textured character, expands the decorative range of finishes.

4. Conclusion

A novel organomineral additive for the polystyrol paint with reduced contents of were prepared and characterized to determine its volatile compounds characteristics. Based on the results of various tests, the following conclusions were drawn:

1. The composition and technology of producing an organomineral additive designed for polystyrene paints as a structuring and dispersing additive, which is a mixed-layer clay with an adsorbed surfactant – the product of the interaction of alkylphenols with OP-4 ethylene oxide, has been developed. It is established that the value of the adsorption of the OP-4 additive on the clay is 0.00038. Methods for the addition of organomineral additives in the formulation of polystyrene paint are proposed.

2. The use of colored sand as a filler in polystyrene paints, which is a mixture of quartz sand and clay (up to 11 %) and has a red-brown color, is substantiated. It is proved that, on the basis of the specified filler, it is possible to obtain a solution of an organomineral additive by adsorbing an OP-4 additive on the surface of the clay particles contained in the colored filler. Based on the results of complex studies, it has been found that the addition of the organomineral additive into a polystyrene paint formulation increases the critical pigment volume concentration by a factor of 1.2, increases the degree of paint milling, reduces dispersion time (by 2 times), and decreases the hiding rate from 160 to 112 g/m².

3. The composition of polystyrene paint with a low content of volatile compounds, designed for exterior and interior decoration of building products and structures. It was revealed that the modified polystyrene paints have the best filling, increased by 13 % retention capacity (relative to the solvent). Coatings based on the developed polystyrene paint have improved crack resistance and appearance qualities. The main protective properties of coatings based on modified polystyrene paint are determined. It is shown that the addition of organic additives contributes to increased resistance to external influences, as well as the strength of adhesion to the substrate by 22 %.

4. The regularities of the influence of the organomineral additive on the technological properties of polystyrene paint and varnish compositions, which consist in increasing the drying time of coatings on the cement-sand substrate by 30 %, are established. Drying time at a low temperature for compounds with organoclay increases by 12.5 %. The regularities of the influence of the organomineral additive on the strength, deformative properties of coatings are established, namely, the addition of the organomineral additive in the polystyrene paint formulation leads to an increase in cohesive strength of 1.6–1.8 times, the elastic modulus 1.2 times, the proportion of elastic deformation 2 times and reduce the proportion of plastic deformation in the total deformation of the coatings. The regularities of changes in internal stresses in coatings based on polystyrene paint are established. It has been shown that the addition of the paint of an organomineral additive into the formulation leads to a decrease in internal stresses by a factor of 2.

References

- Zhegera, K.V., Pyshkina, I.S., Martyashin, G.V. Adhesive dry mix using an amorphous aluminosilicates. Magazine of Civil Engineering. 2018. 82(6). Pp. 23–31. DOI: 10.18720/MCE.82.3.
- Garrido, M.A., Paulo, P.V., Branco, F.A. Service life prediction of façade paint coatings in old buildings. Construction and Building Materials. 2012. 29. Pp. 394–402.
- Fediuk, R.S. Mechanical activation of construction binder materials by various mills. IOP Conf. Series: Mater. Sci. Eng., 2016. Vol. 125, 012019. DOI: 10.1088/1757-899X/125/1/012019.
- García, J.A., Martínez, A., Lerga, B., Rico, M., Fuentes, G.G., Zazpe, M., Rodríguez, R.J. Decorative coatings by PVD on ceramics. Boletín de la Sociedad Española de Cerámica y Vidrio. 2006. Vol. 45(4). Pp. 255–258.
- Fediuk, R.S. High-strength fibrous concrete of Russian Far East natural materials. IOP Conf. Series: Mater. Sci. Eng., 2016. Vol. 116 012020. DOI: 10.1088/1757-899X/116/1/012020.
- Lo, T.Y., Liao, W., Wong, C.K., Tang, W. Evaluation of carbonation resistance of paint coated concrete for buildings. Construction and Building Materials. 2016. Vol. 107. Pp. 299–306.
- Loganina, V.I., Skachkov, J.P., Uchaeva, T.V. Assessment of the Stability of the Staining Process of Building Products and Constructions. International Journal of Applied Engineering Research. 2016. Vol. 11. No. 19. Pp. 9727–9729.
- Chen, S., Jiang, L., Wu, L., Wang, Y., Usmani, A. Damage investigation of cementitious fire resistive coatings under complex loading. Construction and Building Materials. 2019. Vol. 204. Pp. 659–674.
- Loganina, V.I., Kamburg, V.G., Makarova, L.V., Bododkov, N.Yu. Method of Building Optimization of Composites Based on the Criterion Analysis. Contemporary Engineering Sciences. 2014. Vol. 7. Pp. 1555–1563.
- Neto, E., Magin, S., Camões, A., Begonh, A., Evtuguin, D.V., Cachim, P. Characterization of concrete surface in relation to graffiti protection coatings, Construction and Building Materials. 2016. Vol. 102(1). Pp. 435–444.
- Vatin, N.I., Pestryakov, I.I., Sultanov, Sh.T., Ogidan, T.O., Yarunicheva, Y.A., Kiryushina, A.P. Water vapour by diffusion and mineral wool thermal insulation materials. Magazine of Civil Engineering. 2018. 81(5). Pp. 183–192. DOI: 10.18720/MCE.81.18.
- García, O., Malaga, K. Definition of the procedure to determine the suitability and durability of an anti-graffiti product for application on cultural heritage porous materials. Journal of Cultural Heritage. 2012. Vol. 13(1). Pp. 77–82.
- Loganina V.I., Ryzhov, A.D. Structure and properties of synthesized additive based on amorphous aluminosilicates. Case Studies in Construction Materials. 2015. Vol. 3. Pp. 132–136.
- Rossi, S., Fedel, M., Petrolli, S., Deflorian, F. Behaviour of different removers on permanent anti-graffiti organic coatings. Journal of Building Engineering. 2016. Vol. 104–113.
- Deng, Z.P., Huang, X., Li, S.G., Xing, H.W. On-line calibration and uncertainties evaluation of spherical joint positions on large aircraft component for zero-clearance posture alignment. Robotics and Computer-Integrated Manufacturing. 2019. Vol. 56. Pp. 38–54.
- Svintsov, A.P., Nikolenko, Y.V., Kharun, M.I., Kazakov, A.S. Effect of viscosity of petroleum products on deformation properties of concrete. Magazine of Civil Engineering. 2014. Vol. 51(7). Pp. 16–22.

17. Lesovik V.S., Urkhanova L.A., Gridchin A.M., Lkhasaranov S.A. Composite binders on the basis of pearlite raw material of Transbaikalia. *Research Journal of Applied Sciences*. 2014. Vol. 9(12). Pp. 1016–1020.
18. Fediuk, R.S., Yevdokimova, Y.G., Smoliakov, A.K., Stoyushko, N.Y., Lesovik, V.S. Use of geonics scientific positions for designing of building composites for protective (fortification) structures. *IOP Conf. Series: Mater. Science and Eng*. 2017. Vol. 221. 012011.
19. Erofeev, V., Emelyanov, D., Tretiakov, I., Kalashnikov, V., Balathanova, E., Erofeeva, I., Smirnov, V., Matvievskiy, A. Biological resistance of cement composites filled with dolomite powders. *Material Science Forum*. 2016. Vol. 871. Pp. 33–39.
20. Fediuk, R., Timokhin, R., Mochalov, A., Otsokov, K., Lashina, I. Performance properties of high-density impermeable cementitious paste. *Journal of Materials in Civil Engineering*. 2019. Vol. 31(4).
21. Loganina, V.I., Khrustaleva, B.B., Uchaeva, T.V. Statistical management of the production of building products Eastern European. *Journal of advanced technology*. 2013. Vol. 1(3). Pp. 65–67.
22. Fomina, E.V., Kozhukhova, N.I., Sverguzova, S.V., Fomin, A.E. Application of mathematical model methods for optimization tasks in construction materials technology. *Journal of Physics: Conference Series*. 2018. Vol. 1015(5) 052015.
23. Loganina, V.I., Kuimova, E.I., Uchaeva T.V. Application of the method of multivariate analysis to assess the quality of coatings. *Contemporary Engineering Sciences*. 2014. Vol. 7. No. 35. Pp. 1853–1859.
24. Ibragimov, R. The influence of binder modification by means of the superplasticizer and mechanical activation on the mechanical properties of the high-density concrete. *ZKG International*, 2016. Vol. 69(6). Pp. 34–39.
25. Zagorodnjuk, L.H., Lesovik, V.S., Volodchenko, A.A., Yerofeyev, V.T. Optimization of mixing process for heat-insulating mixtures in a spiral blade mixer. *International journal of pharmacy and technology*. 2016. Vol. 8(3). Pp. 15146–15155.
26. Lukutsova, N., Pykin, A., Kleymenicheva, Y., Suglobov, A., Efremochkin, R. Nano-additives for composite building materials and their environmental safety. *International Journal Applied Engineering Research*. 2016. Vol. 11(11). Pp. 7561–7565.
27. Kharitonov, A.P., Simbirtseva, G.V., Nazarov, V.G., Stolyarov, V.P., Dubois, M., Peyroux, J. Enhanced anti-graffiti or adhesion properties of polymers using versatile combination of fluorination and polymer grafting. *Progress in Organic Coatings*. 2015. Vol. 88. Pp. 127–136.
28. Moura, A., Flores-Colen, I., de Brito, J. Study of the effect of three anti-graffiti products on the physical properties of different substrates. *Construction and Building Materials*. 2016. Vol. 107. Pp. 157–164.
29. Ciliberto, E., Battaglia, D.M., Capello, C., Gatto, M., La Delfa, S., Masieri, M., Quarta, G. Graphic Vandalism: Study of the Interaction of Spray Varnishes with Stone Materials and Test of some Antigrffiti Treatments. *Procedia Chemistry*. 2013. Vol. 8. Pp 165–174.
30. Karoglou, M., Bakolas, A., Moropoulou, A., Papapostolou, A. Effect of coatings on moisture and salt transfer phenomena of plasters. *Construction and Building Materials*. 2013. Vol. 48. Pp. 35–44.
31. Binas, V., Papadaki, D., Maggos, Th., Katsanaki, A., Kiriakidis, G. Study of innovative photocatalytic cement based coatings: The effect of supporting materials. *Construction and Building Materials*. 2018. Vol. 168. Pp. 923–930.
32. Oliver-Ortega, H., Chamorro-Trenado, M.À., Soler, J., Mutjé, P., Vilaseca, F., Espinach, F.X. Macro and micromechanical preliminary assessment of the tensile strength of particulate rapeseed sawdust reinforced polypropylene copolymer biocomposites for its use as building material. *Construction and Building Materials*. 2018. Vol. 168. Pp. 422–430.
33. Serra, A., Tarrés, Q., Claramunt, J., Mutjé, P., Ardanuy, M. Espinach, F.X. Behavior of the interphase of dyed cotton residue flocks reinforced polypropylene composites, *Composites. Part B: Engineering*. 2017. Vol. 128. Pp. 200–207.
34. Li, G., Guo, C., Gao, X., Ji, Y., Geng, O. Time dependence of carbonation resistance of concrete with organic film coatings. *Construction and Building Materials*. 2016. Vol. 114. Pp. 269–275.
35. Zafeiropoulou, T., Rakanta, E., Batis, G. Performance evaluation of organic coatings against corrosion in reinforced cement mortars. *Progress in Organic Coatings*. 2011. Vol. 72 (1-2). Pp. 175–180.
36. Creasey, R., Andrews, J.P., Ekolu, S.O., Kruger, D. Long-term 20-year performance of surface coating repairs applied to façades of reinforced concrete buildings. *Case Studies in Construction Materials*. 2017. Vol. 7. Pp. 148–160.
37. Al-Ta'an, S.A., Al-Rifaie, W.N., Al-Neimee, K.A. Properties of Fresh and Hardened High Strength Steel Fibres Reinforced Self-Compacted Concrete. *Tikrit Journal of Engineering Sciences*. 2016. Vol. 23 (1). Pp. 29–37.
38. Asaad, M.A., Ismail, M., Tahir, M.Md., Huseien, G.F., Raja, B., Asmara, Y.P. Enhanced corrosion resistance of reinforced concrete: Role of emerging eco-friendly *Elaeis guineensis*/silver nanoparticles inhibitor. *Construction and Building Materials*. 2018. Vol. 188. Pp. 555–568.
39. Hafizyar, R., Mosaberpanah, M.A. Evaluation of Flexible Road Pavement Condition Index and Life Cycle Cost Analysis of Pavement Maintenance: A Case Study in Kabul Afghanistan. *International Journal of Scientific Engineering Research*. 2018. Vol. 9(8). Pp. 1909–1919.
40. Saha, D., Srivastava, P.K., Kapilesh, B. Variation in ratio of maximum 1-hourly to 24-hourly rainfall at western coastal site in India, *Disaster Advanced*. 2018. Vol. 11(11). Pp. 10–17.
41. Wan, Y., Chen, R., Huang, S., Xu, Y., Zhong, D. A new insulating coating with characteristics of sand texture and imitation ceramic. *Construction and Building Materials*. 2014. Vol. 57. Pp. 9–14.
42. Saha, A., Singh, S.K., Ghosh, A., Ghosh, J., Haldar, M.K. Studies on synthesis and properties of magnesia refractory aggregates prepared from Indian magnesite through plasma fusion. *Ceramic International*. 2015. Vol. 41(2-B). Pp. 2876–2883.
43. Brenna, A., Bolzoni, F., Beretta, S., Ormellese, M. Long-term chloride-induced corrosion monitoring of reinforced concrete coated with commercial polymer-modified mortar and polymeric coatings. *Construction and Building Materials*. 2013. Vol. 48. Pp. 73–744.
44. Pei, X., Noël, M., Green, M., Fam, A., Shier, G. Cementitious coatings for improved corrosion resistance of steel reinforcement. *Surface Coating Technologies*. 2017. Vol. 315. Pp. 188–195.
45. Gonçalves, T.D., Brito, V., Musacchi, J. The whole and the parts: Can lime coatings enhance the drying of salt laden materials? *Construction and Building Materials*. 2014. Vol. 57. Pp. 179–189.
46. Kaczmarek, A., Wesolowska, M. Microstructure of Selected Mortars Undergoing Long-term Influence of External Environment. *Procedia Engineering*. 2016. Vol. 161. Pp. 931–936.
47. Erlbeck, L., Schreiner, P., Fasel, F., Methner, F.-J., Rädle, M. Investigation of different materials for macroencapsulation of salt hydrate phase change materials for building purposes. *Construction and Building Materials*. 2018. Vol. 180. Pp. 512–518.
48. Zhu, N., Li, S., Hu, P., Wei, S., Deng, R., Lei, F. A review on applications of shape-stabilized phase change materials embedded in building enclosure in recent ten years. *Cities and Society*. 2018. Vol. 43. Pp. 251–264.

49. Serralheiro, M.I., de Brito, J., Silva, A. Methodology for service life prediction of architectural concrete facades. *Construction and Building Materials*. 2017. Vol. 133. Pp. 261–274.
50. Sáez-Pérez, M.P., Rodríguez-Gordillo, J., Durán-Suárez, A. Synthetic white pigments (white titanium and white zinc) in different binding media. Influence of environmental agents. *Construction and Building Materials*. 2016. Vol. 114. Pp. 261–274.

Contacts:

Valentina Loganina, 89093169950; loganin@mail.ru

Nadezhda Petukhova, 8-412-49-49-53; npetukhova58@mail.ru

Roman Fediuk, +79502817945; roman44@yandex.ru

Roman Timokhin, +79502817945; gera210307@yandex.ru

© Loganina, V.I., Petukhova, N.A., Fediuk, R.S., Timokhin, R.A., 2019



DOI: 10.18720/MCE.88.3

Полистирольная краска с пониженным содержанием летучих соединений

В.И. Логанина^а, Н.А. Петухова^а, Р.С. Федюк^б, Р.А. Тимохин^б

^а Пензенский государственный университет архитектуры и строительства, г. Пенза, Россия

^б Дальневосточный Федеральный Университет, г. Владивосток, Россия

* E-mail: roman44@yandex.ru

Ключевые слова: здания; строительство; органоминеральная добавка, полистирольная краска, глина, летучие органические соединения

Аннотация. Предложенные органоминеральные добавки являются новыми, экологически чистыми компонентами для полистирольных красок. В качестве наполнителя для полистирольных красок использовался легкий суглинок коричнево-красного цвета. Реологические, технологические и физико-механические свойства лакокрасочных материалов и покрытий на их основе изучались серией стандартных испытаний. Характеристики морозо- и водостойкости, укрывистости и удерживающей способности полистирольной краски подтвердили создание долговечных красок с высокими эксплуатационными свойствами. Комплексные исследования показали, что введение органоминеральной добавки в состав полистирольной краски увеличивает критическую объемную концентрацию пигмента в 1,2 раза, увеличивает степень измельчения краски, уменьшает время диспергирования (в 2 раза) и уменьшает скорость укрытия со 160 до 112 г/м². Анализ результатов экспериментов доказал что введение органических добавок способствует повышению устойчивости к внешним воздействиям, а также прочности сцепления с подложкой на 22 %. Использование полученных результатов позволит создавать полистирольные краски с пониженным содержанием летучих соединений и повышенной трещиностойкостью.

Литература

1. Жегера К.В., Пышкина И.С., Мартяшин Г.В. Клеевая сухая строительная смесь с применением аморфных алюмосиликатов // Инженерно-строительный журнал. 2018. № 6(82). С. 23–31.
2. Kristoffersen M., Pettersen J.E., Aune V., Børvik T. Experimental and numerical studies on the structural response of normal strength concrete slabs subjected to blast loading // Engineering Structures. 2018. Vol. 174. Pp. 242–255.
3. Fediuk R.S. Mechanical activation of construction binder materials by various mills // IOP Conf. Series: Mater. Sci. Eng. 2016. Vol. 125, 012019. DOI: 10.1088/1757-899X/125/1/012019.
4. García J.A., Martínez A., Lerga B., Rico M., Fuentes G.G., Zazpe M., Rodríguez R.J. Decorative coatings by PVD on ceramics // Boletín de la Sociedad Española de Cerámica y Vidrio. 2006. Vol. 45(4). Pp. 255–258.
5. Fediuk R.S. High-strength fibrous concrete of Russian Far East natural materials // IOP Conf. Series: Mater. Sci. Eng. 2016. Vol. 116 012020. DOI: 10.1088/1757-899X/116/1/012020.
6. Lo T.Y., Liao W., Wong C.K., Tang W. Evaluation of carbonation resistance of paint coated concrete for buildings // Construction and Building Materials. 2016. Vol. 107. Pp. 299–306.
7. Loganina V.I., Skachkov J.P., Uchaeva T.V. Assessment of the Stability of the Staining Process of Building Products and Constructions // International Journal of Applied Engineering Research. 2016. Vol. 11. №. 19. Pp. 9727–9729.
8. Chen S., Jiang L., Wu L., Wang Y., Usmani A. Damage investigation of cementitious fire resistive coatings under complex loading // Construction and Building Materials. 2019. Vol. 204. Pp. 659–674.
9. Loganina V.I., Kamburg V.G., Makarova L.V., Bododkov N.Yu. Method of Building Optimization of Composites Based on the Criterion Analysis // Contemporary Engineering Sciences. 2014. Vol. 7. Pp. 1555–1563.
10. Neto E., Magin S., Camões A., Begonh A., Evtuguin D.V., Cachim P. Characterization of concrete surface in relation to graffiti protection coatings // Construction and Building Materials. 2016. Vol. 102(1). Pp. 435–444.
11. Ватин Н.И., Пестряков И.И., Султанов Ш.Т., Огидан О.Т., Яруничева Ю.А., Кирюшина А. Диффузионное влагопоглощение теплоизоляционных изделий и минеральной ваты // Инженерно-строительный журнал. 2018. № 5(81). С. 183–192.
12. García O., Malaga K., Definition of the procedure to determine the suitability and durability of an anti-graffiti product for application on cultural heritage porous materials // Journal of Cultural Heritage. 2012. Vol. 13(1). Pp. 77–82.
13. Loganina V.I., Ryzhov A.D. Structure and properties of synthesized additive based on amorphous aluminosilicates // Case Studies in Construction Materials. 2015. Vol. 3. Pp. 132–136.

14. Rossi S., Fedel M., Petrolli S., Deflorian F. Behaviour of different removers on permanent anti-graffiti organic coatings // *Journal of Building Engineering*. 2016. Vol. 104–113.
15. Deng Z.P., Huang X., Li S.G., Xing H.W. On-line calibration and uncertainties evaluation of spherical joint positions on large aircraft component for zero-clearance posture alignment // *Robotics and Computer-Integrated Manufacturing*. 2019. Vol. 56. Pp. 38–54.
16. Свинцов А.П., Николенко Ю.В., Харун М.И., Казаков А.С. Влияние вязкости нефтепродуктов на деформативные свойства бетона // *Инженерно-строительный журнал*. 2014. №7(51). С. 16–22.
17. Lesovik V.S., Urkhanova L.A., Gridchin A.M., Lkhasaranov S.A. Composite binders on the basis of pearlite raw material of Transbaikalia // *Research Journal of Applied Sciences*. 2014. Vol. 9(12). Pp. 1016–1020.
18. Fediuk R.S., Yevdokimova Y.G., Smoliakov A.K., Stoyushko N.Y., Lesovik V.S. Use of geonics scientific positions for designing of building composites for protective (fortification) structures // *IOP Conf. Series: Mater. Science and Eng*. 2017. Vol. 221. 012011.
19. Erofeev V., Emelyanov D., Tretiakov I., Kalashnikov V., Balathanova E., Erofeeva I., Smirnov V., Matvievskiy A. Biological resistance of cement composites filled with dolomite powders // *Material Science Forum*. 2016. Vol. 871. Pp. 33–39.
20. Fediuk R., Timokhin R., Mochalov A., Otsokov K., Lashina I. Performance properties of high-density impermeable cementitious paste // *Journal of Materials in Civil Engineering*. 2019. Vol. 31(4).
21. Loganina V.I., Khrestaleva B.B., Uchaeva T.V. Statistical management of the production of building products Eastern European // *Journal of advanced technology*. 2013. Vol. 1(3). Pp. 65–67.
22. Fomina E.V., Kozhukhova N.I., Sverguzova S.V., Fomin A.E. Application of mathematical model methods for optimization tasks in construction materials technology // *Journal of Physics: Conference Series*. 2018. Vol. 1015(5) 052015.
23. Loganina V.I., Kuimova E.I., Uchaeva T.V. Application of the method of multivariate analysis to assess the quality of coatings // *Contemporary Engineering Sciences*. 2014. Vol. 7. No. 35. Pp. 1853–1859.
24. Ibragimov R. The influence of binder modification by means of the superplasticizer and mechanical activation on the mechanical properties of the high-density concrete // *ZKG International*. 2016. Vol. 69(6). Pp. 34–39.
25. Zagorodnjuk L.H., Lesovik V.S., Volodchenko A.A., Yerofeyev V.T. Optimization of mixing process for heat-insulating mixtures in a spiral blade mixer // *International journal of pharmacy and technology*. 2016. Vol. 8(3). Pp. 15146–15155.
26. Lukutsova N., Pykin A., Kleymenicheva Y., Suglobov A., Efremochkin R. Nano-additives for composite building materials and their environmental safety // *International Journal Applied Engineering Research*. 2016. Vol. 11(11). Pp. 7561–7565.
27. Kharitonov A.P., Simbirtseva G.V., Nazarov V.G., Stolyarov V.P., Dubois M., Peyroux J. Enhanced anti-graffiti or adhesion properties of polymers using versatile combination of fluorination and polymer grafting // *Progress in Organic Coatings*. 2015. Vol. 88. Pp. 127–136.
28. Moura A., Flores-Colen I., de Brito J. Study of the effect of three anti-graffiti products on the physical properties of different substrates // *Construction and Building Materials*. 2016. Vol. 107. Pp. 157–164.
29. Ciliberto E., Battaglia D.M., Capello C., Gatto M., La Delfa S., Masieri M., Quarta G. Graphic Vandalism: Study of the Interaction of Spray Varnishes with Stone Materials and Test of some Antigrffiti Treatments // *Procedia Chemistry*. 2013. Vol. 8. Vol. 165–174.
30. Karoglou M., Bakolas A., Moropoulou A., Papapostolou A. Effect of coatings on moisture and salt transfer phenomena of plasters // *Construction and Building Materials*. 2013. Vol. 48. Pp. 35–44.
31. Binas V., Papadaki D., Maggos Th., Katsanaki A., Kiriakidis G. Study of innovative photocatalytic cement based coatings: The effect of supporting materials // *Construction and Building Materials*. 2018. Vol. 168. Pp. 923–930.
32. Oliver-Ortega H., Chamorro-Trenado M.À., Soler J., Mutjé P.F., Vilaseca F., Espinach X. Macro and micromechanical preliminary assessment of the tensile strength of particulate rapeseed sawdust reinforced polypropylene copolymer biocomposites for its use as building material // *Construction and Building Materials*. 2018. Vol. 168. Pp. 422–430.
33. Serra A., Tarrés Q., Claramunt J., Mutjé P., Ardanuy M., Espinach F.X. Behavior of the interphase of dyed cotton residue flocks reinforced polypropylene composites // *Composites. Part B: Engineering*. 2017. Vol. 128. Vol. 200–207.
34. Li G., Guo C., Gao X., Ji Y., Geng O. Time dependence of carbonation resistance of concrete with organic film coatings // *Construction and Building Materials*. 2016. Vol. 114. Pp. 269–275.
35. Zafeiropoulou T., Rakanta E., Batis G. Performance evaluation of organic coatings against corrosion in reinforced cement mortars // *Progress in Organic Coatings*. 2011. Vol. 72 (1-2). Pp. 175–180.
36. Creasey R., Andrews J.P., Ekolu S.O., Kruger D. Long-term 20-2018 performance of surface coating repairs applied to façades of reinforced concrete buildings // *Case Studies in Construction Materials*. 2017. Vol. 7. Pp. 148–160.
37. Al-Taan S.A., Al-Rifaie W.N., Al-Neimee K.A. Properties of Fresh and Hardened High Strength Steel Fibres Reinforced Self-Compacted Concrete // *Tikrit Journal of Engineering Sciences*. 2016. Vol. 23 (1). Pp. 29–37.
38. Asaad M.A., Ismail M., Tahir M.Md., Huseien G.F., Raja B., Asmara Y.P. Enhanced corrosion resistance of reinforced concrete: Role of emerging eco-friendly Elaeis guineensis/silver nanoparticles inhibitor // *Construction and Building Materials*. 2018. Vol. 188. Pp. 555–568.
39. Hafizyar R., Mosaberpanah M.A. Evaluation of Flexible Road Pavement Condition Index and Life Cycle Cost Analysis of Pavement Maintenance: A Case Study in Kabul Afghanistan // *International Journal of Scientific Engineering Research*. 2018. Vol. 9 (8). Pp. 1909–1919.
40. Saha D., Srivastava P.K., Kapilesh B. Variation in ratio of maximum 1-hourly to 24-hourly rainfall at western coastal site in India // *Disaster Advanced*. 2018. Vol. 11(11). Pp. 10–17.
41. Wan Y., Chen R., Huang S., Xu Y., Zhong D. A new insulating coating with characteristics of sand texture and imitation ceramic // *Construction and Building Materials*. 2014. Vol. 57. Pp. 9–14.
42. Saha A., Singh S.K., Ghosh A., Ghosh J., Haldar M.K. Studies on synthesis and properties of magnesia refractory aggregates prepared from Indian magnesite through plasma fusion // *Ceramic International*. 2015. Vol. 41(2-B). Pp. 2876–2883.
43. Brenna A., Bolzoni F., Beretta S., Ormellesse M. Long-term chloride-induced corrosion monitoring of reinforced concrete coated with commercial polymer-modified mortar and polymeric coatings // *Construction and Building Materials*. 2013. Vol. 48. Pp. 73–744.
44. Pei X., Noël M., Green M., Fam A., Shier G. Cementitious coatings for improved corrosion resistance of steel reinforcement // *Surface Coating Technologies*. 2017. Vol. 315. Pp. 188–195.
45. Gonçalves T.D., Brito V., Musacchi J. The whole and the parts: Can lime coatings enhance the drying of salt laden materials? // *Construction and Building Materials*. 2014. Vol. 57. Pp. 179–189.

46. Kaczmarek A., Wesołowska M. Microstructure of Selected Mortars Undergoing Long-term Influence of External Environment // Procedia Engineering. 2016. Vol. 161. Pp. 931–936.
47. Erlbeck L., Schreiner P., Fasel F., Methner F.-J., Rädle M. Investigation of different materials for macroencapsulation of salt hydrate phase change materials for building purposes // Construction and Building Materials. 2018. Vol. 180. Pp. 512–518.
48. Zhu N., Li S., Hu P., Wei S., Deng R., Lei F. A review on applications of shape-stabilized phase change materials embedded in building enclosure in recent ten 2018s // Cities and Society. 2018. Vol. 43. Pp. 251–264.
49. Serralheiro M.I., de Brito J., Silva A. Methodology for service life prediction of architectural concrete facades // Construction and Building Materials. 2017. Vol. 133. Pp. 261–274.
50. Sáez-Pérez M.P., Rodríguez-Gordillo J., Durán-Suárez A. Synthetic white pigments (white titanium and white zinc) in different binding media. Influence of environmental agents // Construction and Building Materials. 2016. Vol. 114. Pp. 261–274.

Контактные данные:

Валентина Ивановна Логанина, 89093169950; эл. почта: loganin@mail.ru

Надежда Алексеевна Петухова, 8-412-49-49-53; эл. почта: npetukhova58@mail.ru

Роман Сергеевич Федюк, +79502817945; эл. почта: roman44@yandex.ru

Роман Андреевич Тимохин, +79502817945; эл. почта: gera210307@yandex.ru

© Логанина В.И., Петухова Н.А., Федюк Р.С., Тимохин Р.А., 2019



DOI: 10.18720/MCE.88.4

Modeling of the mean wind loads on structures

S.Yu. Solovev^a, E.F. Khrapunov^{b*}

^a Krylov State Research Centre, St. Petersburg, Russia

^b Peter the Great St. Petersburg Polytechnic University, St. Petersburg, Russia

* E-mail: khrapunov.evgenii@yandex.ru

Keywords: aerodynamic force on buildings, atmospheric boundary layer, wind loads, physical modeling, Silsoe cube, wind tunnel, pressure coefficient, facades

Abstract. Correct determination and consideration of wind loads are primary importance in the design of unique architectural objects such as high-rise buildings, sport arenas, airports, large-span bridges. One of the most accurate ways to determine wind loads is to carry out model tests in specialized wind tunnels. Nowadays, during wind tests much attention is paid to the correct modeling of natural wind properties. In present work comparison of the most popular approaches for turbulence length scale determination is presented. One of the purposes of this study is to compare the main aerodynamic characteristics of the simple cube model obtained in uniform flow and during ABL modeling. This paper provides a brief overview of the method for ABL modelling in test section of the Landscape wind tunnel and contains experimental data on mean flow velocity distribution, turbulence intensity, dimensionless spectral density and integral scale of turbulence. The comparison of experimental data obtained for cube model in various wind tunnels revealed the influence of ABL on geometry and intensity of separation zones at the cube sides, and, as consequence, the influence of the same on integral and local aerodynamic characteristics of the object. On the basis of the obtained experimental data, it was concluded that the intensity of the separation zones has significant influence on the total aerodynamic loads, which is usually not taken into account in the framework of applied calculations. The difference in numerical values of aerodynamic characteristics was up to 30 %.

1. Introduction

According to Russian and foreign regulatory documents on the design of structures [1], wind load is to be determined with allowance for the specifics of atmospheric boundary layer (ABL). This requirement has to do with significant influence of ABL on aerodynamic characteristics of high-rise buildings and structures. Full-scale characteristics of ABL for each type of locality are known and specified in numerous design regulatory documents and meteorological reference guides and handbooks.

In the 50s of the last century, researchers began to pay attention to the study and modeling of ABL in wind tunnels, due to the fact that the designed at that time buildings began to show increased sensitivity to the wind's effects, which required to take into account the wind loads acting on the structures more accurately [2]. For a detailed account of wind loads, it was necessary to change experimental approach of studies of models of structures in a uniform flow and proceed to conducting experimental studies in wind tunnels that allow the characteristics of the atmospheric boundary layer to be reproduced. Despite this, research in wind tunnels, creating a uniform air flow, is still very popular in modern practice due to both the high prevalence of such experimental stands, and their great development. That's why it is important to understand how the experimental data obtained in laboratories differs from the information about real objects.

The task to determine the simulation criteria in wind tunnel tests of buildings and structures is not easy question. For example, it is impossible to perform tests with Reynolds number equals to the nature one. Besides, during wind tunnel tests it is important not only to simulate air-structure interactions but also atmospheric boundary layer properties. One of the main criteria for modeling ABL properties in this case is the

Solovev, S.Yu., Khrapunov, E.F. Modeling of the mean wind loads on structures. Magazine of Civil Engineering. 2019. 88(4). Pp. 42–51. DOI: 10.18720/MCE.88.4.

Соловьев С.Ю., Храпунов Е.Ф. Моделирование средних ветровых нагрузок на сооружения // Инженерно-строительный журнал. 2019. № 4(88). С. 42–51. DOI: 10.18720/MCE.88.4.



This open access article is licensed under CC BY 4.0 (<https://creativecommons.org/licenses/by/4.0/>)

Jensen number [3], which allows to estimate the necessary length of the test section for the natural growth of the boundary layer with the necessary characteristics. In accordance with this criterion, the minimum length of the test section can be estimated as 15–20 meters. In special-purpose wind tunnels with shorter test section, ABL modeling is based not only on natural boundary layer build-up along the length of test section wherein the additional large-scale obstacles and discrete roughness elements. The correctness of modeled ABL characteristics (mean wind velocity profile, vertical variation in turbulence intensity, energy characteristics of the flow, integral scale of turbulence) is to be ensured by proper selection of test section geometry, the geometry and number of obstacles. A seemingly simple method of ABL representation offers significant diversity in practical implementation [4, 5].

Determination of wind effects on modern buildings during wind tunnel tests can be difficult due to the complex geometry of the structure or not trivial properties of surrounding territory, for example in high-density cities. In case of low-rise buildings there are some challenges that are less evident with large buildings [8]. These challenges are connected with fundamental questions of simulation of ABL properties and can be formulated in simplify form as: what part of the turbulent spectrum should be simulated? High-frequency part corresponds to turbulence intensity changing with height, while low-frequency part corresponds to integral length scale changing with height. It should be noted that it is much harder to simulate changing of turbulence length scale than turbulence intensity. For the other hand changing of turbulence length scale with height in test section should correlate with well-known dependencies. Simplification of models geometry can be effective method for investigation of fundamental air-structure interaction. Besides information about pressure distribution on sides of the cube for example is commonly used in a lot of practical applications.

Modeling of interaction between air flow and bluff body is one of the basic tasks of wind tunnel tests. The main sources of information about properties of model of cube are [6–12]. In [9] comparison of pressure distributions on the sides of cube for uniform flow and ABL flow is presented. This data set is commonly used for validation of computational model and verification of experimental data obtained in wind tunnels. However information about full aerodynamic loads in this work is absent. In [10] the major attempt of results comparison of different laboratories is described. It should be noted that conditions of wind tests were not be the same but still data about pressure distribution in characteristic points on the surfaces of the model is in a good agreement. Works [8, 11] must be mentioned in this list due to performed experiments with natural-sized model – Silsoe cube. Nowadays data about pressure distribution on the surfaces of Silsoe cube is very popular due to the fact that wind tests using full-scale model provide possibilities of more accurate comparison. On the other hand, the number of papers where data about pressure distribution in high range of cube orientation is presented is limited. Such data were published in [12] but the height of test section in wind tunnel was not large enough to perform correct modeling.

The primary objectives of this study are as follows:

1. To compare the main aerodynamic characteristics (coefficients C_x , C_y , C_p) of cube model obtained in uniform flow and during ABL modeling,
2. To verify the main ABL parameters modeled in Landscape wind tunnel of the Krylov State Research Centre (Figure 1).

2. Methods

Experimental studies were carried out in two wind tunnels of the Krylov State Research Centre: large wind tunnel generating uniform stationary velocity profile (case I in Figure 2a), and Landscape wind tunnel (LWT) making it possible to simulate vertical distribution of the main ABL parameters (case II in Figure 2a)

Large wind tunnel of the Krylov Centre is a subsonic closed-circuit tunnel with open test section (length 5 m, width 4 m, height 2.5 m). Maximum flow velocity in test section is up to 100 m/s.

Landscape wind tunnel of the Krylov Centre is a two-level subsonic wind tunnel wherein the return flow channel is fitted with 7 impellers generating air flow at speeds up to 15 m/s. Test section (length 18 m, width 11 m, height 2.3 m) constitutes the first level in its entirety. Large-scale obstacles and different-scale discrete roughness elements are used to model ABL characteristics (as described in [5]).

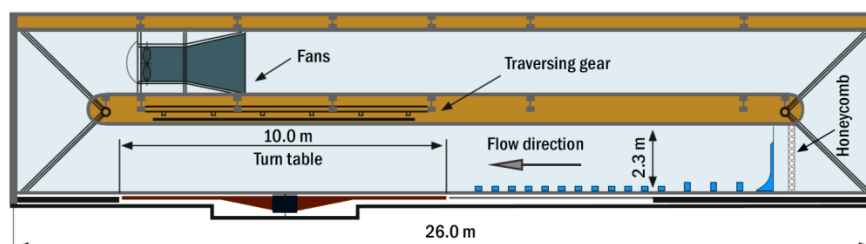


Figure 1. Scheme of the Landscape wind tunnel.

The main ABL parameters were determined in LWT using single-wire anemometer, velocity values were registered at sampling rate of 5 kHz, and measurement time at each point was equal to 900 seconds. This set of parameters made it possible not only to describe average processes, but also to obtain data on velocity fluctuations at measurement points with high level of accuracy.

In order to compare aerodynamic parameters of the cube obtained for different types of wind flow, a 400 mm cube model (Silsoe cube model [8]) was manufactured. Total aerodynamic loads on the cube were determined using load cell mounted at the base of the cube. Cell's axes system is shown in Figure 2b. For the purpose of pressure measurement, 87 perforations were bored in the cube as shown in Figure 2c (corresponds to [11]). The perforations were connected to pressure scanner by means of tube transfer system. In the course of experiment, pressure was measured during 30 seconds at 100 Hz within the range of angles from 0° to 180° where zero angle corresponds to normal flow incident on the face side of the cube. Thirty perforations were placed on one of the quadrant of the top side that made it possible to obtain data on pressure field at different angles of incident flow. The length of the tubes was chosen according to criteria of influence minimization on experimental data. Considering the dimensions of test sections of wind tunnels and cube size under study, flow chocking did not exceed 1%. Reynolds number, calculated using side height and flow velocity at cube height, for both cases was equal to $Re = 2.1 \times 10^5$.

3. Results and Discussion

3.1. Mean flow characteristics

The analysis of experimental data obtained for the purpose of modeling of ABL characteristics in LWT test section was performed using the following approach. Mean velocity was determined by the following ratio

$$\bar{U} = \frac{1}{n} \sum_i u_i, \quad (1)$$

where n is number of measured points;

u_i is instantaneous velocity at i -th point of time. Mean square deviation and turbulence level were calculated using the formulae respectively.

$$\sigma_u = \sqrt{(u_i - \bar{U})^2}, \quad (2)$$

$$It = \frac{\sigma_U}{U} \cdot 100. \quad (3)$$

Measurement algorithm is described in detail in the following study [14]. Vertical variation in dimensionless mean velocity profile is shown in Figure 3,a.

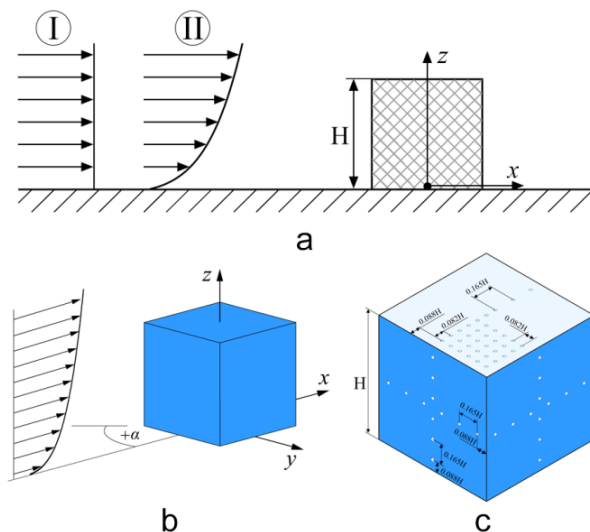


Figure 2. Cube model a) flow boundary conditions; b) model-linked coordinate system; c) pressure measurement points at cube surface.

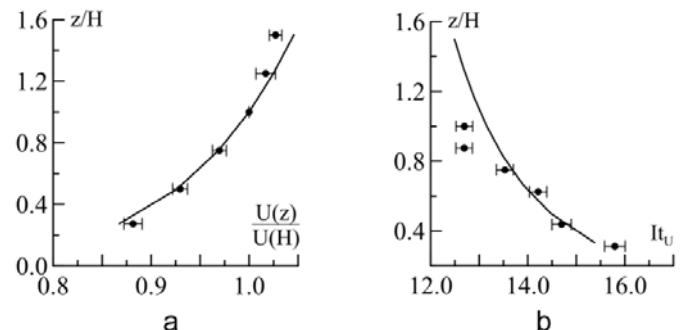


Figure 3. Changing of the main properties of the flow with test section height a) mean velocity; b) turbulence intensity.

The cube height was chosen as a reference height $z_{ref} = H = 0.4$ m, and the velocity at that height was chosen as a reference velocity U_{ref} . Exponential law for vertical variation in mean velocity specific for "0" type of locality pursuant to [1] is also plotted in the figure. Vertical variation in turbulence intensity as well as respective ratio from [1] are shown in Figure 3, b. It can be concluded that selected configuration of large-scale obstacles and discrete roughness makes it possible to reproduce main characteristics of full-scale wind for specified type of locality with sufficient accuracy.

3.2. Turbulence length scales in LWT

The questions of scale open up the whole area of physical simulation [3]. The basis of theories often includes considerations about dimensionless criteria: Strouhal, Reynolds, Froude, Jensen etc. In ABL wind tunnels not only dimensionless criteria is important but also mean and actual properties of the modeled flow, such as turbulence length scale.

The description of algorithms to determine turbulence scales is available in numerous well-known studies, e.g. [13, 14]. In present study, the scales were determined using autocorrelation coefficient (4) and Karman spectrum (5). In this case, it was assumed that Taylor hypothesis is true for the entire height of wind tunnel test section.

$$L_x^U = \bar{U} \cdot \int_0^\infty \frac{\overline{u_i'(t)u_i'(t+\tau)}}{\bar{u}_i'^2} d\tau, \tag{4}$$

$$\bar{S} = \frac{4 \cdot \bar{f}}{\left[1 + 70.7 \cdot \bar{f}^2\right]^{5/6}}, \tag{5}$$

where $\bar{S} = \frac{f \cdot S}{\sigma^2}$ is dimensionless spectral density,

$\bar{f} = \frac{f \cdot L_x^U}{U}$ is dimensionless frequency. Formula (5) can only be used on the assumption that all

spectral densities of signals at different heights coincide in dimensionless form. Dimensionless spectral densities at different heights within the LWT test section are shown in Figure 4. It can be seen that they match well both in high-frequency band ("5/3" law) and low-frequency band (position of maximum).

Turbulence scales determined using the abovementioned methods are given in Figure 5. As it is shown in the figure, these methods give similar results, so both of them can be used to obtain reliable data on flow parameters.

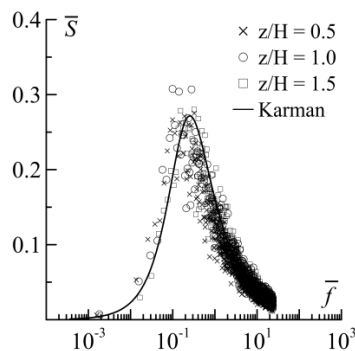


Figure 4. Dimensionless spectral density at different heights.

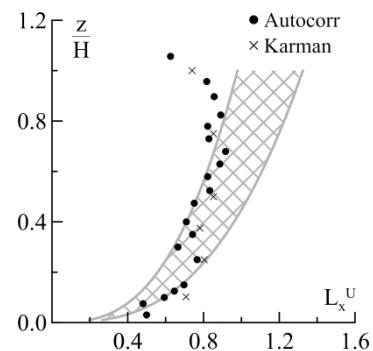


Figure 5. Changing of L_x^U and its acceptable 15% variation range.

Vertical variation in longitudinal integral turbulence scale in full-scale conditions can be described using the formula proposed in [15]

$$L_x^U = 25 \cdot (z - d)^{0.35} z_0^{-0.063}, \tag{6}$$

where d is zero place displacement in law-of-the-wall velocity,

z_0 is roughness length parameter in law-of-the-wall. Full description of all parameters can be easily found in [14].

The procedure for scale determination using formula (6) is suggested in [13]. Vertical variation in longitudinal integral turbulence scale in LWT test section as well as the range to cover the determined scales in accordance with formula (6) and requirements set forth in [15], are indicated in Figure 5. The results given therein imply the possibility to model longitudinal integral turbulence scale in LWT test section.

As outlined above and previously discussed in numerous well-known studies, e.g. [11], in order to determine mean wind loads on buildings and structures, it is sufficient to model mean velocity profile, turbulence intensity and high-frequency part of energy spectrum since these are parameters which are the most influential on obtained results. In case of study of aeroelastic oscillations simulations of turbulence length scales and Reynolds stresses have to be included in addition to parameters noted above.

3.3. Aerodynamic forces

High frequency load cells were used to record the values of aerodynamic forces and moments. The values measured in model-fixed coordinate system were non-dimensionalized using ratio (7). If it is necessary to change from object-fixed coordinate system to flow-fixed coordinate system (C_x^{flow} ; C_y^{flow}), simple rotation matrix can be used.

$$C_{x,y} = \frac{F_{x,y}}{\rho \frac{V^2}{2} S}, \quad (7)$$

where $F_{x,y}$ is aerodynamic force, acting in respective direction, N;

ρ is air density, in experimental conditions it was equal to 1.225 kg/m³;

S is cube side area, m²;

V is incident flow velocity, m/s.

The experiment was performed for those incident flow velocities wherein the aerodynamic characteristics do not vary with Re number. Aerodynamic coefficients C_x and C_y at two different flow velocities within the angular range from 0° to 180° are shown in Figure 6. It can be seen that C_y distribution is symmetrical about the angle of 90°, maximum values of coefficients coincide and occur at angles spaced 90° apart, that fully corresponds to the airflow physics. There was also discovered a non-monotonic variation in C_x coefficient in the vicinity of angle of 80° as well as similar non monotonic variation in C_y distribution at 10° and 170°, associated with separation zones occurring at the cube sides [16]. It is well known that for square prism flow patterns can be classified into two types, perfect separation type where angles of attack is less than ~14° and reattachment type where angle of attack is larger than ~14°. Aerodynamic coefficients change drastically at this point, i.e. mean drag coefficient becomes minimum, i.e. and magnitude of the lift coefficient reaches maximum [17, 18].

Dependencies for aerodynamic coefficients, obtained in both cases are qualitatively similar while quantitative difference between them can be up to 30 % as it has already been shown in other studies [19]. In some cases, such wind load overstating is acceptable; however, in a number of designs, this kind of “margin” may result in unjustified strength/mass/material consumption overrating.

It should be noted that transition from aerodynamic coefficients to dimensional aerodynamic force is to be made using dependency (7) in strict compliance with selected area S and height wherein the velocity V is determined, both in full-scale and experimental conditions.

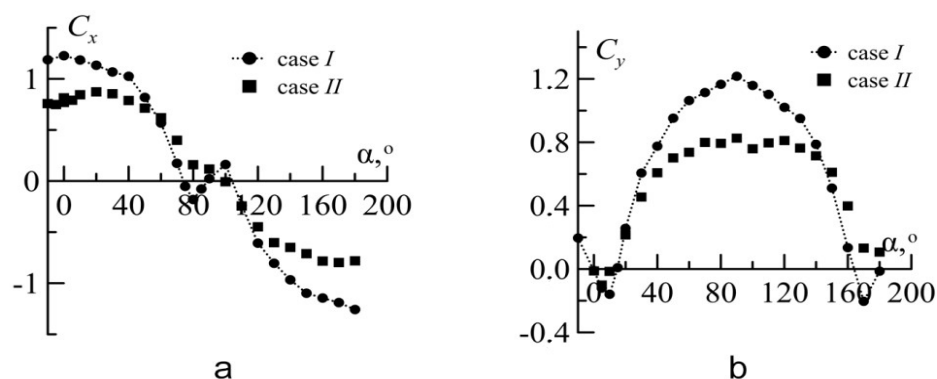


Figure 6. Distribution of aerodynamic coefficients
a) coefficient C_x ; b) coefficient C_y .

3.4. Mean wind loads

The main outcome of aerodynamic tests at the design stage is determination of mean, fluctuating and peak aerodynamic wind loads (following by [1]), acting on the facades of building and structures. In accordance with regulatory documents (e.g. [1]), wind loads can be determined using aerodynamic coefficients represented by dimensionless pressure coefficients.

For this purpose, during the experimental studies in LWT, instantaneous pressure values are measured at the points on the surface of object model. Values of sampling rate and measurement time are selected for each object individually depending on density of surrounding buildings (if any), the geometry of the object itself and other factors. Typical values of sampling rate exceed 100 Hz, minimum measurement time is 30 seconds.

Measurement data on instantaneous pressure at the points on the surface of object model at different angles of incident airflow make it possible to use mathematical tools of statistics theory in order to determine the required parameters. However, this paper deals only with mean pressure distribution on the surface of the cube under study.

In general engineering problems pressure coefficient is understood as a sum of coefficients for external and internal pressure acting on the surface element. In case of experimental studies in wind tunnel, internal pressure is usually not determined due to the difficulties associated therewith, so from this point on C_p will be used as external pressure coefficient determined as follows

$$\bar{C}_p = \frac{\frac{1}{N} \sum_j p_j}{q}, \quad (8)$$

where N is amount of data, obtained within measurement time

p_j is pressure measured at each point of time, Pa;

q is mean dynamic pressure at the cube height measured at $3H$ distance from its lateral side, Pa. All results are presented against dimensionless coordinate d/H , where d is distance from the point with "0" index as shown in explanatory figures and in Figure 2c.

Mean pressure coefficient distribution along symmetry lines at zero angle α obtained in both cases is shown in Figure 7. Figure also contains data presented in well-known studies [8–10]. As it can be seen, pressure coefficient along the front side for uniform flow remains almost constant. Pressure coefficient $C_p = -0.4$ at the top side for this case remains almost constant as well. Influence of the top side of the cube on pressure distribution in both cases starts at distance $0.75 \cdot H$ from floor – pressure coefficient become smaller than 1 in uniform flow (Figure 7,a). In case of nonuniform incident flow profile, pressure coefficient distribution along the face side is not constant and correlates well with experimental data obtained in other studies and with full-scale measurement results, including local minimum on the face side at distance $0.25 \cdot H$ from floor. In addition it should be noted that there is significant difference in pressure distribution between two cases along the top, left and right sides, associated with influence of gradient flow on geometry and intensity of separation zone. According to Figure 7.b there is a symmetry in pressure coefficient distribution along intervals 1→2 and 3→4 and even for back side of the cube in both cases.

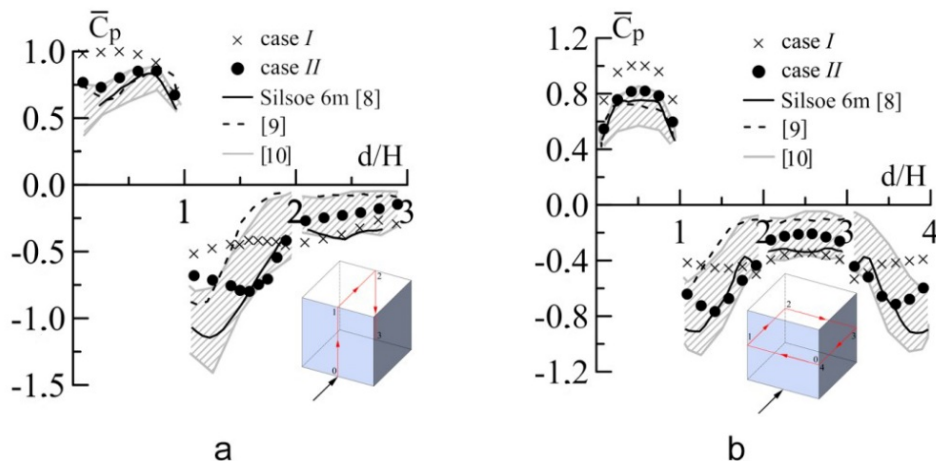


Figure 7. Pressure coefficient distribution along symmetry lines
a) vertical; b) horizontal.

Mean pressure coefficient distribution along symmetry lines at different angles α , obtained in both cases, is shown at Figures 8 and 9. There is no big difference in pressure distribution between all presented angles on the back side in uniform flow (Figure 8,a). Size of the separation zone on the top side in case I is much smaller than in case II. It should be taken into account, for example during snow drift simulation where sizes of separation zones play significant role.

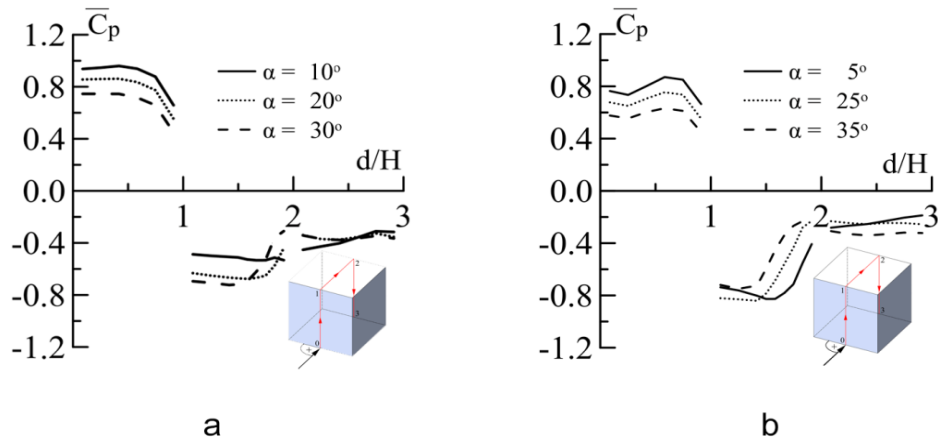


Figure 8. Pressure coefficient distribution along vertical symmetry line for different angles a) case I; b) case II.

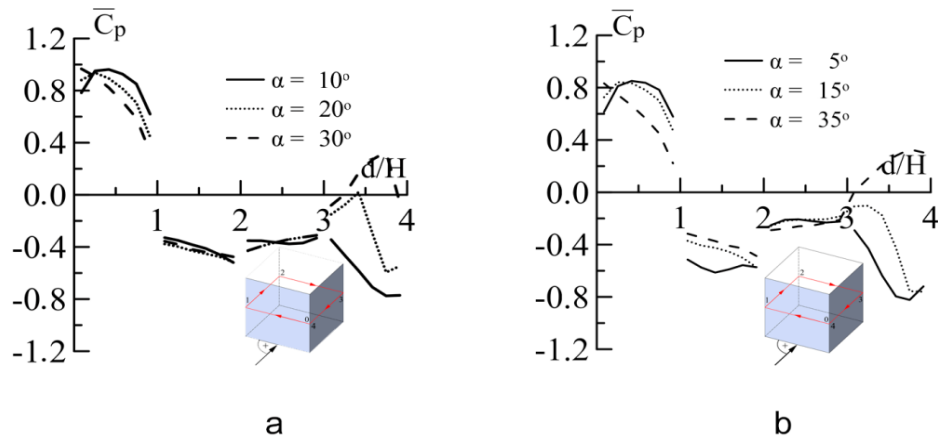


Figure 9. Pressure coefficient distribution along horizontal symmetry line for different angles a) case I; b) case II.

4. Conclusion

Nowadays, correct determination and consideration of wind loads are of primary importance in the design of unique architectural objects such as high-rise buildings, sport arenas, airports, large-span bridges. Moreover, correct modelling of ABL parameters in test section of wind tunnel is quite challenging, since it requires simultaneous representation of mean velocity profile of full-scale wind, vertical variation in its turbulence intensity, energy characteristics and turbulence integral scale.

This paper contains the results for resolving the following tasks:

1. To compare the main aerodynamic characteristics (coefficients C_x , C_y , C_p) of cube model obtained in uniform flow and during ABL modeling,
2. To verify the main ABL parameters modelled in Landscape wind tunnel of the Krylov State Research Centre.

Large-scale obstacles and discrete roughness were used to create ABL in LWT test section; this made it possible to reproduce mean velocity profile, varying in accordance with exponential law, and turbulence intensity of longitudinal velocity. Spectral densities obtained using Welch spectrogram demonstrate that high-frequency portion of energy spectra, which has an utmost importance in determining flow influence on the modeled objects, are predicted correctly. The data about integral turbulence scale presented herein [20] and obtained using two of the most frequently implemented approaches demonstrate the possibility for this parameter to be modeled in wide test section of wind tunnel.

In order to estimate the influence of ABL on main aerodynamic parameters, the model of cube was tested in two wind tunnels with and without ABL being considered. Experimental data obtained in the course of present investigation regarding air flow influence on cube model in ABL, correlate well with the results obtained by other researches in earlier studies. Comparison of experimental data revealed significant influence of ABL on geometry and intensity of separation zones at cube sides and, as consequence, the influence of the same on integral (C_x , C_y) and local C_p aerodynamic characteristics of the object. The difference in numerical values of aerodynamic characteristics was up to 30 %.

Based on experimental results discussed herein the following may be concluded:

1. experimental data on mean flow velocity distribution, turbulence intensity, dimensionless spectral density and integral scale of turbulence are in good agreement with existing dependencies and previous studies;

2. pressure distribution on the surfaces of cube model, obtained during the experiment in LWT, correlate well with existing full-scale measurement data and the results of experimental studies performed using similar test facilities;

3. the main ABL characteristics can be modeled correctly in LWT test section using the method for flow non uniformity generation described in this paper;

4. correct ABL modelling used to determine aerodynamic parameters of structures makes it possible to eliminate unreasonable wind load margins.

References

1. Eurocode 1: Actions on structures – 1–4: General actions – Wind actions.
2. Simiu, E., DongHun, Y. Wind Effects on Structures. Modern Structural Design for Wind. Wiley Blackwell. 2019. P. 496.
3. Jensen, M. The Model-law for Phenomena in Natural Wind. Ingenioren, 1958. No. 2(4). Pp. 273–282.
4. Irwin, H.P.A.H. The Design of Spires for Wind Simulation. J. Wind Eng. Ind. Aerodyn. 1981. Vol. 7. Pp. 361–366.
5. Counihan, J. An improved method of simulating an atmospheric boundary layer in a wind tunnel. Atmospheric Environment. 1967. Vol. 3. Pp. 197–214.
6. Hubová, O. et al. Pressure Coefficients on the Model of Silsoe Cube Determined by Tests in BLWT Tunnels. Roczniki Inżynierii Budowlanej – ZESZYTY. 2014. No 143. Pp. 85–90.
7. Sarkar, P. et al. Full-scale study of conical vortices and roof corner pressures. Wind and Structures An International Journal. 2001. Vol. 4(2). Pp. 131–146.
8. Richards, P.J. et al. Wind pressures on a 6m cube. J. Wind Eng. Ind. Aerodyn. 2001. Vol. 89. Pp. 1553–1564.
9. Castro, I.P., Robins, A.G. The flow around a surface-mounted cube in uniform and turbulent streams. J. Fluid Mech. 1977. Vol. 79 (pt. 2). Pp. 307–335.
10. Hölscher, N., Niemann, H.-J. Towards quality assurance for wind tunnel tests: a comparative testing program of the Windtechnologische Gesellschaft. J. Wind Eng. Ind. Aerodyn. 1998. Vol. 74. Pp. 599–608.
11. Richards, P.J. et al. Wind-tunnel modeling of the Silsoe Cube. J. Wind Eng. Ind. Aerodyn. 2007. Vol. 95. Pp. 1384–1399.
12. Sakamoto, H. Flow around a cubic body immersed in a turbulent boundary layer. J. Wind Eng. Ind. Aerodyn. 1982. Vol. 9. Pp. 275–293.
13. Cook, N.J. Determination of the model scale factor in wind-tunnel simulations of the adiabatic atmosphere boundary layer. J. of Ind. Aerodyn. 1978. Vol. 2. Pp. 311–321.
14. Kozmar, H. Wind-tunnel simulations of the suburban ABL and comparison with international standards. Wind and Structures International Journal. 2011. Vol. 14(1). Pp. 15–34.
15. ESDU 85020. Characteristics of atmospheric turbulence near the ground: Part II: single point data for strong winds (neutral atmosphere). Engineering Sciences Data Unit. 1985.
16. Norris, S.E., Richards, P.J. Transient Flow Structures around a Cubic Building. Report at 19th Australian Fluid Mechanics Conference. 2014. P. 4.
17. Oka, S., Ishihara, T. Numerical study of aerodynamic characteristics of a square prism in a uniform flow. J. of Wind Eng. Ind. Aerodyn. 2009. Vol. 97. Pp. 548–559.
18. Hirano, H., Maruoka, A., Watanabe, S. Calculations of aerodynamic properties of rectangular cylinder with slenderness ratio of 2:1 under various angles of attack. Journal of Structural Engineering. 2002. Vol. 48A. Pp. 971–978.
19. Pustoshny, A., Solovev, S. Landscape Wind Tunnel Krylov State Research Centre. Marine Intellectual Technologies. 2018. Vol. 3(41). Pp. 69–75. (rus)
20. Solovev, S., Khrapunov, E. Simulation of Energy Characteristics of ABL. Vestnik of Saint Petersburg University. Mathematics. Mechanics. Astronomy. 2018. Vol. 5(63). Pp. 689–700. (rus)

Contacts:

Sergei Solovev, +79062512310; aerodynamics.spb@gmail.com

Evgenii Khrapunov, +79818151792; khrapunov.evgenii@yandex.ru



DOI: 10.18720/MCE.88.4

Моделирование средних ветровых нагрузок на сооружения

С.Ю. Соловьев, Е.Ф. Храпунов*

^a ФГУП «Крыловский государственный научный центр», Санкт-Петербург, Россия

^b Санкт-Петербургский политехнический университет Петра Великого, Санкт-Петербург, Россия

* E-mail: hrapunov.evgenii@yandex.ru

Ключевые слова: аэродинамическая сила на здания, атмосферный пограничный слой, ветровая нагрузка, физическое моделирование, куб Силсо, аэродинамическая труба, коэффициент давления, фасады

Аннотация. Правильное определение и учет ветровых нагрузок имеют первостепенное значение при проектировании уникальных архитектурных объектов, таких как высотные здания, спортивные арены, аэропорты, большепролетные мосты. Одним из наиболее точных способов определения ветровых нагрузок считается проведение модельных испытаний в специализированных аэродинамических трубах. В последние десятилетия подход к моделированию воздействия воздушного потока на статические сооружения претерпел значительные изменения – в настоящее время все большее внимание уделяется корректному моделированию особенностей натурального ветра. При этом важно понимать, какое именно значение на результат эксперимента оказывает учет или не учет параметров ветра. В работе представлено сравнение наиболее популярных методов определения масштабов турбулентности – с использованием корреляционной функции и соотношения Кармана. Также целью данного исследования является сравнение основных аэродинамических характеристик (коэффициенты C_x , C_y , C_p) модели простого куба, полученных в однородном потоке и во время моделирования атмосферного пограничного слоя (АПС). В статье представлен краткий обзор метода моделирования АПС в рабочей части Ландшафтной аэродинамической трубы, а также экспериментальные данные о распределении средней скорости потока, интенсивности турбулентности, безразмерной спектральной плотности. Сравнение экспериментальных данных, полученных для модели куба в различных аэродинамических трубах, выявило влияние АПС на характеристики зон отрыва на сторонах куба и, как следствие, влияние на интегральные (C_x , C_y) и локальные (C_p) аэродинамические характеристики объекта. На основе полученных экспериментальных данных сделан вывод о существенном влиянии интенсивности отрывных зон на суммарные аэродинамические нагрузки, что обычно не учитывается в рамках практического расчета. В частности, показано, что учет особенностей градиентного потока приводит к снижению определяемых коэффициентов на 30 %.

Литература

1. Eurocode 1: Actions on structures – 1–4: General actions – Wind actions.
2. Simiu E., DongHun Y. Wind Effects on Structures. Modern Structural Design for Wind. Wiley Blackwell. 2019. P. 496.
3. Jensen M. The Model-law for Phenomena in Natural Wind // Ingenioren, 1958. No. 2(4). Pp. 273–282.
4. Irwin H.P.A.H. The Design of Spires for Wind Simulation // J. Wind Eng. Ind. Aerodyn. 1981. Vol. 7. Pp. 361–366.
5. Counihan J. An improved method of simulating an atmospheric boundary layer in a wind tunnel // Atmospheric Environment. 1967. Vol. 3. Pp. 197–214.
6. Hubová O. et al. Pressure Coefficients on the Model of Silsoe Cube Determined by Tests in BLWT Tunnels // Roczniki Inżynierii Budowlanej – ZESZYTY. 2014. No. 143. Pp. 85–90.
7. Sarkar P. et al. Full-scale study of conical vortices and roof corner pressures // Wind and Structures An International Journal. 2001. Vol. 4(2). Pp. 131–146.
8. Richards P.J. et al. Wind pressures on a 6m cube // J. Wind Eng. Ind. Aerodyn. 2001. Vol. 89. Pp. 1553–1564.
9. Castro I.P., Robins A.G. The flow around a surface-mounted cube in uniform and turbulent streams // J. Fluid Mech. 1977. Vol. 79 (pt. 2). Pp. 307–335.
10. Hölscher N., Niemann H.-J. Towards quality assurance for wind tunnel tests: a comparative testing program of the Windtechnologische Gesellschaft // J. Wind Eng. Ind. Aerodyn. 1998. Vol. 74. Pp. 599–608.
11. Richards P.J. et al. Wind-tunnel modeling of the Silsoe Cube // J. Wind Eng. Ind. Aerodyn. 2007. Vol. 95. Pp. 1384–1399.

12. Sakamoto H. Flow around a cubic body immersed in a turbulent boundary layer // J. Wind Eng. Ind. Aerodyn. 1982. Vol. 9. Pp. 275–293.
13. Cook N.J. Determination of the model scale factor in wind-tunnel simulations of the adiabatic atmosphere boundary layer // J. of Ind. Aerodyn. 1978. Vol. 2. Pp. 311–321.
14. Kozmar H. Wind-tunnel simulations of the suburban ABL and comparison with international standards // Wind and Structures International Journal. 2011. Vol. 14(1). Pp. 15–34.
15. ESDU 85020. Characteristics of atmospheric turbulence near the ground: Part II: single point data for strong winds (neutral atmosphere). Engineering Sciences Data Unit. 1985.
16. Norris S.E., Richards P.J. Transient Flow Structures around a Cubic Building. Report at 19th Australian Fluid Mechanics Conference. 2014. P. 4.
17. Oka S., Ishihara T. Numerical study of aerodynamic characteristics of a square prism in a uniform flow // J. of Wind Eng. Ind. Aerodyn. 2009. Vol. 97. Pp. 548–559.
18. Hirano H., Maruoka A., Watanabe S. Calculations of aerodynamic properties of rectangular cylinder with slenderness ratio of 2:1 under various angles of attack // Journal of Structural Engineering. 2002. Vol. 48A. Pp. 971–978.
19. Pustoshny A., Solovlev S. Landscape Wind Tunnel Krylov State Research Centre // Marine Intellectual Technologies. 2018. Vol. 3(41). Pp. 69–75.
20. Solovlev S., Khrapunov E. Simulation of Energy Characteristics of ABL. Vestnik of Saint Petersburg University // Mathematics. Mechanics. Astronomy. 2018. Vol. 5(63). Pp. 689–700.

Контактные данные:

Сергей Юрьевич Соловьев, +79062512310; эл. почта: aerodynamics.spb@gmail.com

Евгений Федорович Храпунов, +79818151792; эл. почта: hrapunov.evgenii@yandex.ru

© Соловьев С.Ю., Храпунов Е.Ф., 2019



DOI: 10.18720/MCE.88.5

Factors effecting the recovery process of self-repairing concrete

Q. Zhao^{a,b}, P. Cheng^{*a}, Y. Wei^c, J. Wang^d

^aNortheast Forestry University, Harbin, Heilongjiang, China

^bNortheast Agricultural University, Harbin, Heilongjiang, China

^cYellow River Survey Planning and Design Co., Ltd., Zhengzhou City, Henan Province, China

^dHarbin Dongan Automobile Engine Manufacturing Co., Ltd., Harbin, Heilongjiang, China

* E-mail: 492954791@qq.com

Keywords: self-repairing cement concrete, initial crack width, placement method, external environment, repair rate

Abstract. In order to explore the influence of external environmental factors, the initial width of cracks and the placement of glass fiber tubes on the repairing effect of self-repairing concrete, glass fiber tubes are built in self-repairing concrete specimens, Self-repair test using repair adhesive. The repair rate α is characterized by the ratio of the initial crack width l to the time t used for repair completion, and the effects of the above three factors on the repair rate were analyzed. The results show that at $-15\sim 30\text{ }^{\circ}\text{C}$, the repair rate increases with the increase of temperature; at $0\sim 30\text{ }^{\circ}\text{C}$, the growth rate of repair rate is obviously less than the growth rate of $-15\sim 0\text{ }^{\circ}\text{C}$. When the temperature is below $0\text{ }^{\circ}\text{C}$, the temperature plays a leading role in the improvement of the repair rate; The repair rate increases first and then decreases with the increase of the initial crack width. When the crack width is from 0.4 to 0.6 mm , the repair rate increases significantly faster than the crack width from 0.6 to 1.0 mm . The rate of repair of the crack width from 1.0 to 1.5 mm is significantly higher than that of the crack width from 1.5 mm to 2.0 mm . And when the initial crack width is about 1.0 mm , the repair rate reaches the highest level. When the initial crack width and the repair temperature are between -15 and $30\text{ }^{\circ}\text{C}$, the repair rate of the glass fiber tube is slightly better than that of the diamond when the inverted trapezoid is placed. The initial width of the crack has the greatest influence on the repair rate. Followed by temperature conditions and placement of fiberglass tubes. The corresponding factor levels at the maximum repair rate are 1.0 mm , $30\text{ }^{\circ}\text{C}$ and inverted trapezoids.

1. Introduction

Cement concrete pavement can adapt to the requirements of large-scale transportation, high speed, large traffic flow, etc., which are necessary for the development of transportation, and has many advantages such as high strength, good stability, long service life and low maintenance costs, etc. A non-homogeneous brittle material can easily generate microcracks inside the component under the influence of the surrounding environment. If these micro-cracks cannot be repaired in time, these irregular and inconsistent micro-cracks will further develop under the influence of external factors. Macroscopic cracks that will greatly reduce the durability and safety of cement pavements [1, 2]. Therefore, how to prevent cracks on cement pavement is crucial. At present, the commonly used crack repair methods include surface repair method, grouting caulking plugging method, structural reinforcement method, concrete replacement method, electrochemical protection method and other passive repair methods, while bionic self-healing method is an active repair method, which can be timely repair concrete cracks and restore their compactness and mechanical properties [3,4]. At present, the self-healing method to repair concrete cracks, that is, self-repairing concrete is still in the primary stage of intelligent concrete [5, 6]. Many scholars have carried out various attempts and researches on self-repairing concrete technology. Victor Li [7] and other fibers and quartz sand were incorporated into the fiber-reinforced cementitious composite material to achieve control of crack dispersion. The maximum distance between the cracks was 0.3 cm , and the average spacing was only $60\text{ }\mu\text{m}$. Carolyn Dry [8] selected a acetal polymer solution as a repairing agent, and the mechanical properties of the repaired test piece were

Zhao, Q., Cheng, P., Wei, Y., Wang, J. Factors effecting the recovery process of self-repairing concrete. Magazine of Civil Engineering. 2019. 88(4). Pp. 52–59. DOI: 10.18720/MCE.88.5.

Чжао Ц., Чен П., Вей Ю., Ван Д. Факторы, влияющие на процесс восстановления самовосстанавливающегося бетона // Инженерно-строительный журнал. 2019. № 4(88). С. 52–59. DOI: 10.18720/MCE.88.5.



This open access article is licensed under CC BY 4.0 (<https://creativecommons.org/licenses/by/4.0/>)

improved and improved. Michelle Pelletier [9] used the reaction product of $\text{Ca}(\text{OH})_2$ and Na_2SiO_3 to fill the cracks and achieve the purpose of repairing cracks. However, the research on the influencing factors of crack repair ability is limited to the internal factors such as repair materials and mix ratio. However, there are few studies on external factors such as temperature and load. Therefore, in order to achieve the best crack healing effect, the internal factors affecting the repair rate will be affected. It is necessary to conduct research in combination with external factors [10,11]. Self-repairing concrete with built-in fiberglass tube is a kind of self-repairing concrete. The reason why it can repair the crack is the combination of the initial width of the crack, the number and position of the fiberglass tube, the type of adhesive, and the external environment. In order to explore how each factor affects the self-repairing effect, the initial width of the crack, the placement of the fiberglass tube and the external environment (temperature) are selected as variables. The repair rate α is characterized by the ratio of the initial crack width l to the time t used for repair completion. The research was made in order to explore the influence of external environmental factors, the initial width of cracks and the placement of glass fiber tubes on the repairing effect of self-repairing concrete [12].

2. Methods

2.1. Repair materials and their carriers

The performance of the repair material is critical to the repair rate. The advantage of the adhesive is high bonding strength and good fluidity [13–16]. Select resin-based end isocyanate-based polyether-type single-liquid polyurethane as an adhesive, such as No. 717 adhesive produced by Great Wall manufacturers. The structural characteristics make it have the characteristics of normal temperature curing, temperature resistance, oil resistance, acid and alkali resistance. Therefore, test selected it as a repair material.

It is important to repair the effect of repairing the number of carriers and whether the mechanical properties of the repair carrier and the concrete matrix match. Since the coefficient of linear expansion of glass and concrete is very close, when the temperature changes, the glass and concrete will not break the bond between them due to the relative temperature deformation; and the glass is composed of various oxides, the calculation shows that the compressive strength is generally 500–2000 MPa, which is much higher than the compressive strength of concrete, which avoids the problem that the glass tube is broken before the concrete due to the load [17, 18]; in addition, the tensile strength of the glass is usually around 1/15 of compressive strength, in order to crack the glass tube while the specimen is cracked, a suitable glass tube size was calculated [19, 20]. In summary, the carrier used in this paper is an insulating glass fiber tube with a length of 25 cm, an inner diameter of 5 mm and a wall thickness of 0.5 mm.

2.2. Matrix materials and their mix ratio

The repaired fiber with a length of 25 cm, an inner diameter of 5 mm and a wall thickness of 0.5 mm was used for the test. The test substrate is a concrete anti-folding test piece with a size of 400 mm×100 mm×100 mm, and the tension zone is provided with 2 $\sqrt{8}$ fixtures. The cement is 42.5 grade ordinary portland cement; the fineness modulus of sand is 2.7; the gravel is 5–20 mm continuous gradation; the apparent density of concrete is 2406 kg/m³; the water is tap water; the admixture is naphthalene efficient water reducing agent (FDN-C), water-to-binder ratio is 0.41. The concrete mix ratio is shown in Table 1.

Table 1. Concrete mix ratio.

| Cement (kg/m ³) | Sand (kg/m ³) | Gravel (kg/m ³) | Water (kg/m ³) | Water Reducer (kg/m ³) |
|-----------------------------|---------------------------|-----------------------------|----------------------------|------------------------------------|
| 440 | 712 | 1068 | 180 | 6.6 |

2.3. Factors affecting repair capacity and evaluation indicators

Self-repairing concrete with built-in fiberglass tube is a kind of self-repairing concrete. The reason why it can repair the crack is the combination of the initial width of the crack, the number and position of the fiberglass tube, the type of adhesive, and the external environment. The factors affecting the repair rate can be generally divided into internal and external factors. The internal factors mainly include the content of various minerals (such as the amount of fly ash and silica fume), mix ratio, repair materials, repair carriers, etc. The external factors mainly include repair time, repair environment, initial crack width, external load, etc. Through the comparison of many internal and external factors, the initial crack size, the position of the glass fiber tube and the external environment (temperature) were taken as the influencing factors, and the internal and external factors were combined to study.

2.4. Influencing factors

The initial width of the crack has a great influence on the repair rate. Studies have shown that self-repairing concrete can only repair micro-cracks within a certain width range, but does not explain the effect of the initial crack size on the repair rate and repair time of the repaired specimens. Therefore, it is very important to study the effect of the initial crack width on the repair rate. In order to make the initial crack have the same characteristics as the actual crack, referring to the crack prefabrication method in the existing research, the

crack is obtained by applying a specific load to the test piece. The test shows that when the applied load is respectively 50, 55, 60, 65, 70 % of the failure load, the corresponding main crack width observed by the PTS-C10 intelligent crack width observer is about 0.4mm, 0.6 mm, 1.0 mm, 1.5 mm and 2.0 mm. The PTS-C10 intelligent crack width observer is shown in Figure 1. The reading view of the crack width is shown in Figure 2, the unit in Figure 2 is mm, the maximum range is 2 mm, and the minimum scale is 0.02 mm.



Figure 1. PTS-C10 intelligent crack width observer.

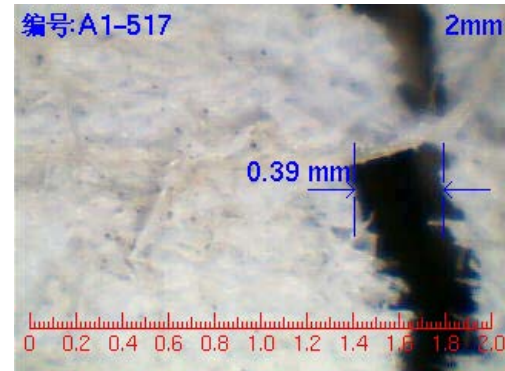


Figure 2. Crack width observation reading viewport.

The position of the fiberglass tube has a significant impact on the repair capacity. The hollow glass tube is added inside the test piece, and the flexural strength of the test piece will inevitably decrease. The test shows that the bending strength caused by placing four glass tubes is significantly lower than that when six pieces are placed. The placement is in the form of diamond and trapezoidal, where the reduction was the smallest compared with other placement methods, and the flexural strength decreased respectively by 5.7 % and 6.1 %, which was much lower than the lowest flexural strength recovery rate of 38.4 % in the test. In addition, the setting position is too low, the adhesive cannot repair the crack above the set position, the setting position is too high, and the adhesive capacity may not be enough to flow to the bottom of the crack. Therefore, it is important to properly set the position of the fiberglass tube. Studies have shown that the cracks are mainly produced in the longitudinal middle position of the test piece, and the development trend from bottom to top appears, so the position of the fiberglass tube in the test is selected in the middle to the lower position. In summary, the glass fiber tube is placed in the test in the form of a diamond and an inverted trapezoid as shown in Figure 3, the unit of measurement in Figure 3 is mm.

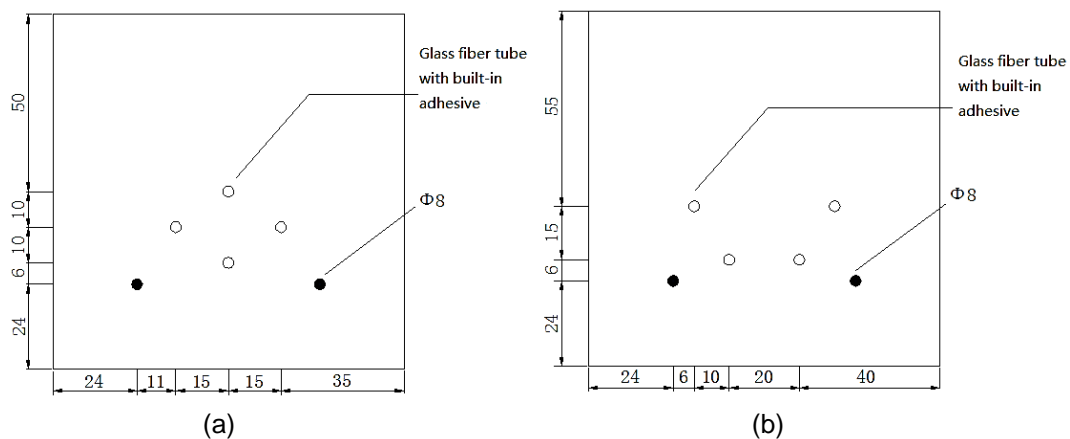


Figure 3. How to place the glass fiber tube in the test piece:(a) the glass tube is placed in a diamond shape (b) the glass tube is placed in an inverted trapezoid.

The external environmental conditions are one of the important factors affecting the self-repairing effect of cracks. China has a vast territory and a large difference in environmental conditions. In order to understand the repair rate of cracks under different environmental conditions, five different self-healing conditions are selected to represent the environmental conditions in different regions of China. The test data obtained can provide theoretical guidance on appropriate environmental conditions or areas for self-repairing concrete. In addition, for cement concrete pavement, at a certain moment, the road surface temperature is affected by three basic heat transfer modes of radiation, convection and heat conduction. It can be seen that the temperature of the road panel changes continuously with the temperature of the air. And cement concrete pavement as a pavement structure with specific thickness, the temperature along the thickness direction is also a certain regularity and constantly changing. The prediction model of temperature field of various cement pavement panels shows that the 22 cm thick cement road panel is taken as an example. The temperature of the pavement surface is nearly 15 °C higher than the temperature at the bottom of the pavement. At the same pavement depth, the highest temperature and the lowest temperature in the same day differ by about 20 °C.

Therefore, in order to make the temperature conditions of the test conditions coincide with the actual middle panel temperature conditions, it is very important to choose the temperature conditions reasonably. The meteorological statistics show that the temperature in Harbin is generally rising from February to June, and the humidity is decreasing. Based on the analysis of temperature and humidity data of various months in Harbin in recent years, and considering the environmental conditions must to a certain extent represent the average temperature conditions in various regions of China as well as the temperature conditions at different panel thicknesses in different seasons in Harbin. Finally, five environmental conditions as shown in Table 2 were selected.

Table 2. Crack self-healing environmental conditions.

| Environmental condition number | Corresponding monthly average temperature (°C) | Description of environmental conditions in the test |
|--------------------------------|--|---|
| 1 | -15 | Outdoor environmental conditions in Harbin in February |
| 2 | 0 | Outdoor environmental conditions in Harbin in March |
| 3 | 10 | Outdoor environmental conditions in Harbin in April |
| 4 | 20 | Outdoor environmental conditions in Harbin from May to June |
| 5 | 30 | 30 °C constant temperature oven |

2.5. Evaluation indicators

Through the monitoring of the cracks during the repair of each test piece, it can be found that the repair of the crack mainly occurs in the first two days, that is, with the repair carrier breaks, the adhesive flows out from the flow and flows to the crack generating portion, and then gradually solidifies, and finally the crack was fixed. Therefore, the crack monitoring results of the first two days of repair rate are the basis for calculation. The calculation formula of the time α used for the repair rate is as shown in Equation 1.

$$\alpha = \frac{l}{t}, \quad (1)$$

where α is repair rate (mm/d);

l is initial crack width (mm);

t is the time taken to complete the crack repair (d).

3. Results and Discussion

3.1. Preparation of test pieces

The filling and sealing of the adhesive in the glass fiber tube is carried out as follows: First, the end of the glass fiber tube is closed. Use GLUE GUN GT-10 hot melt glue gun to inject about 3 mm hot melt adhesive into the glass tube to seal one end of the glass tube. The operation is as shown in Figure 4. The glass tube sealed with hot melt adhesive is shown in Figure 5; After the molten rubber is solidified, the port sealed with hot melt adhesive is applied with epoxy resin AB glue to double seal; Secondly, the adhesive is injected into the glass fiber tube. Since the end of the glass fiber tube is closed, it is difficult to apply the adhesive. The infusion method of the adhesive in this test follows the lifting duct method used for pouring concrete in the bored pile, that is as shown in Figure 6. The syringe shown is used in conjunction with the sheared medical infusion belt for injection, so that the injection of the infusion belt can speed up the injection speed while avoiding the appearance of the air column. Finally, the other end of the glass fiber tube filled with the adhesive is closed. The sealing method is the same as the first step. The steel and the glass fiber tube filled with the adhesive can be placed in the corresponding position when pouring the concrete. The pouring process of the test piece is shown in Figure 7.

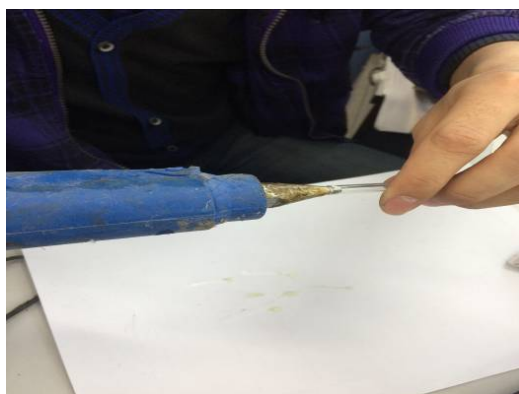


Figure 4. GLUE GUN GT-10 hot melt glue gun.



Figure 5. Hot melt glue closed glass tube.



Figure 6. Adhesive syringe.



Figure 7. Preparation of test piece.

3.2. Test technology route

In order to make the environmental conditions in the crack repair as consistent as possible in the actual environmental conditions, the test was carried out in five separate times, and 12 test pieces were prepared each time, 10 of which were test groups and 2 were control groups. Different degrees of load were applied to the test specimens to cause micro-cracks, and the test specimens were subjected to standard flexural strength tests. That is, when the environmental condition is 30 °C constant temperature oven, a total of 12 test pieces are required, wherein the glass fiber tube is placed in the test piece in a diamond shape, and the inverted test piece is 6 pieces each. Setting the destructive load of specimens placed in the diamond shape and inverted trapezoidal shape to be PA1 and PB1 in the standard flexural test, respectively, and the pre-applied loads of the other 10 specimens are 50 % P_{A1}, 55 % P_{A1}, 60 % P_{A1}, 65 % P_{A1}, 70 % P_{A1} and 50 % P_{B1}, 55 % P_{B1}, 60 % P_{B1}, 65 % P_{B1}, 70 % P_{B1} respectively. The initial cracks of the test pieces under the other four environmental conditions are prefabricated in the same way.

3.3. Analysis of test results

3.3.1. External environmental impact

In order to explore how the repair environment (temperature, humidity) affects the repair rate, the placement of the fiberglass tubes is diamond-shaped, inverted trapezoidal, Under the condition of the initial crack width is 0.4mm, 0.6mm, 1.0mm, 1.5mm, 2.0mm, the test pieces repaired in different repair environments are monitored and analyzed, and the relationship between the repair rate and temperature conditions is shown in Figure 8,9, the temperature unit is °C.

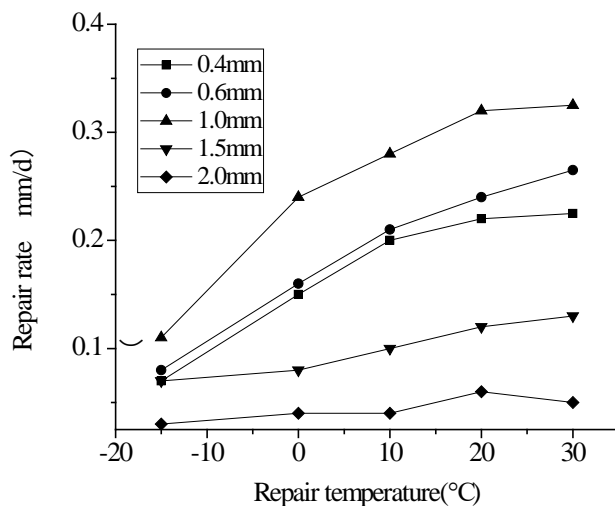


Figure 8. Change of repair rate with temperature when the glass fiber tube is placed in a diamond shape.

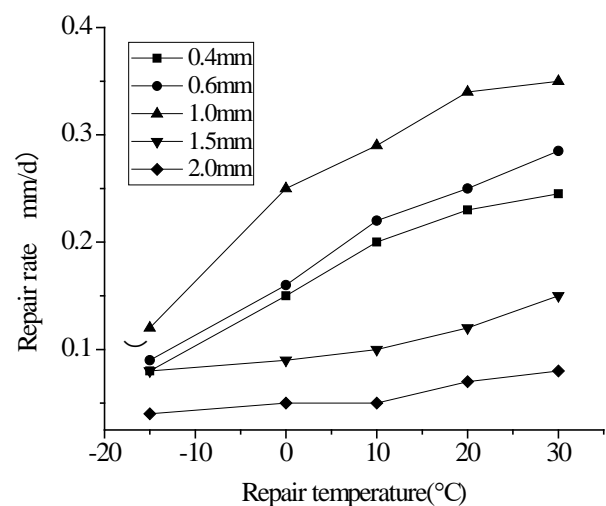


Figure 9. The change of repair rate with temperature when the glass fiber tube is placed in inverted trapezoid.

It can be seen from Figure 8 and 9 that no matter whether the glass fiber tube is placed in a diamond shape or an inverted trapezoidal shape, the repair rate increases with the increase of temperature in a certain temperature range, and the repair rate increases as the temperature increases. The speed gradually decreases. This shows that the change of temperature condition has a great influence on the repair rate. In a certain temperature range, the higher the temperature, the faster the repair rate is.

The above phenomenon occurs because the solidification of the selected adhesive is affected by various factors such as environmental conditions and the shape of the bonding surface etc. With the increase of temperature in the environmental conditions, the selected adhesive filled in the crack can be solidified earlier, and the reinforced concrete is re-established. Forming a solid whole, which in turn allows the crack to be repaired quickly, so the repair rate is higher. The rate of repair rate in each temperature range above 0 °C is significantly less than the growth rate of -15 °C to 0 °C. Due to a certain extent, when the temperature is below 0 °C, the temperature plays a leading role in the improvement of the repair rate. The temperature increases and the repair rate increases rapidly; When the temperature is above 0 °C, temperature is not the dominant factor affecting the repair rate.

3.3.2. Impact of initial crack width

In order to investigate how the initial crack width affects the repair rate, 50, 55, 60, 65 and 70 %, of the failure load of the control specimens are applied respectively under the conditions of the placement of the glass fiber tubes in the shape of diamonds and inverted trapezoids. And the corresponding initial crack widths are respectively 0.4, 0.6, 1.0, 1.5, 2.0mm. The relationship between the repair rate and the initial crack width is shown in Figures 10 and 11 after two days of repair under different curing conditions (temperature, humidity).

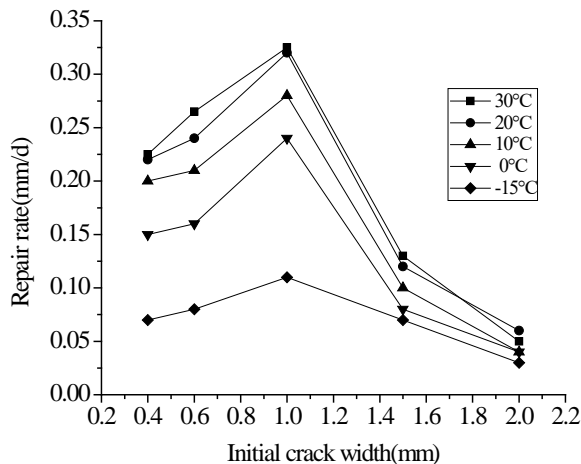


Figure 10. Repair rate as a function of initial crack width (diamond).

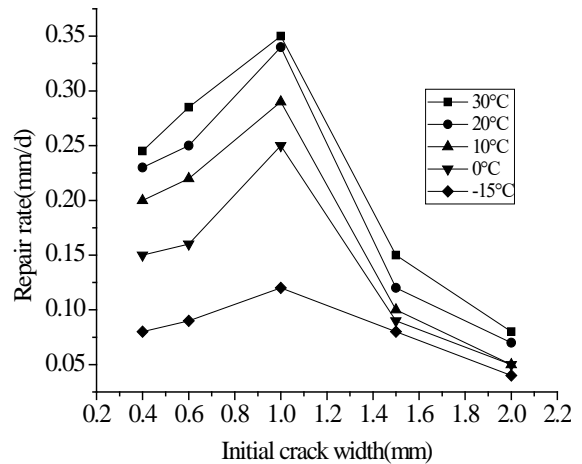


Figure 11. Repair rate as a function of initial crack width (inverted trapezoid).

It can be seen from Figures 10 and 11 that no matter whether the glass fiber tube is placed in a diamond shape or an inverted trapezoid, the repair rate increases first and then decreases with the increase of the initial crack width, and when the initial crack width is about 1.0 mm, the repair rate reached the highest level. Regardless of whether the glass fiber tube is placed in a diamond shape or a trapezoidal shape, the growth rate of the repair rate when the crack width is from 0.4 mm to 0.6 mm is significantly lower than that of the crack width from 0.6 mm to 1.0 mm; and the crack width is from 1.0 mm to the rate of repair rate at 1.5 mm is significantly higher than the rate at which the crack width decreases from 1.5 mm to 2.0 mm.

The occurrence of the above phenomenon is the result of the interaction of the fluidity of the adhesive and the capacity of the adhesive in the carrier. Because the fluidity of the adhesive is affected by the crack size, when the temperature conditions are the same, the fluidity of the adhesive increases with the increase of the crack width, so when the pre-cut crack width is less than 1.0 mm, the volume of the repair adhesive capacity is relatively larger and the fluidity is lower, so it can not flow to the crack better, and the repair rate is lower. As the crack width increases, the fluidity of the adhesive increases, and it can be quickly flowed to the interface of the crack at the crack to repair it. As the crack width is further increased, the adhesive capacity in the repair carrier is received. The limitation of the adhesive is that the viscosity increases and the fluidity increases, and the faster flow to the lower end of the crack, and the upper crack cannot be repaired, so the repair rate is greatly reduced. It can be seen that when the initial crack width is about 1.0 mm, the repair rate of the crack is the highest, and at this time, the capacity of the repair material in the repair carrier and the fluidity of the repair material in the crack are matched.

3.3.3. Influence of glass fiber tube placement

In order to explore how the placement of the glass fiber tube affects the repair rate, under the conditions of the initial crack width and the same curing conditions (temperature, humidity), the glass fiber tube is placed in a variable, placement includes diamonds and inverted trapezoids. The relationship between the repair rate and the initial crack width is shown in Figure 12.

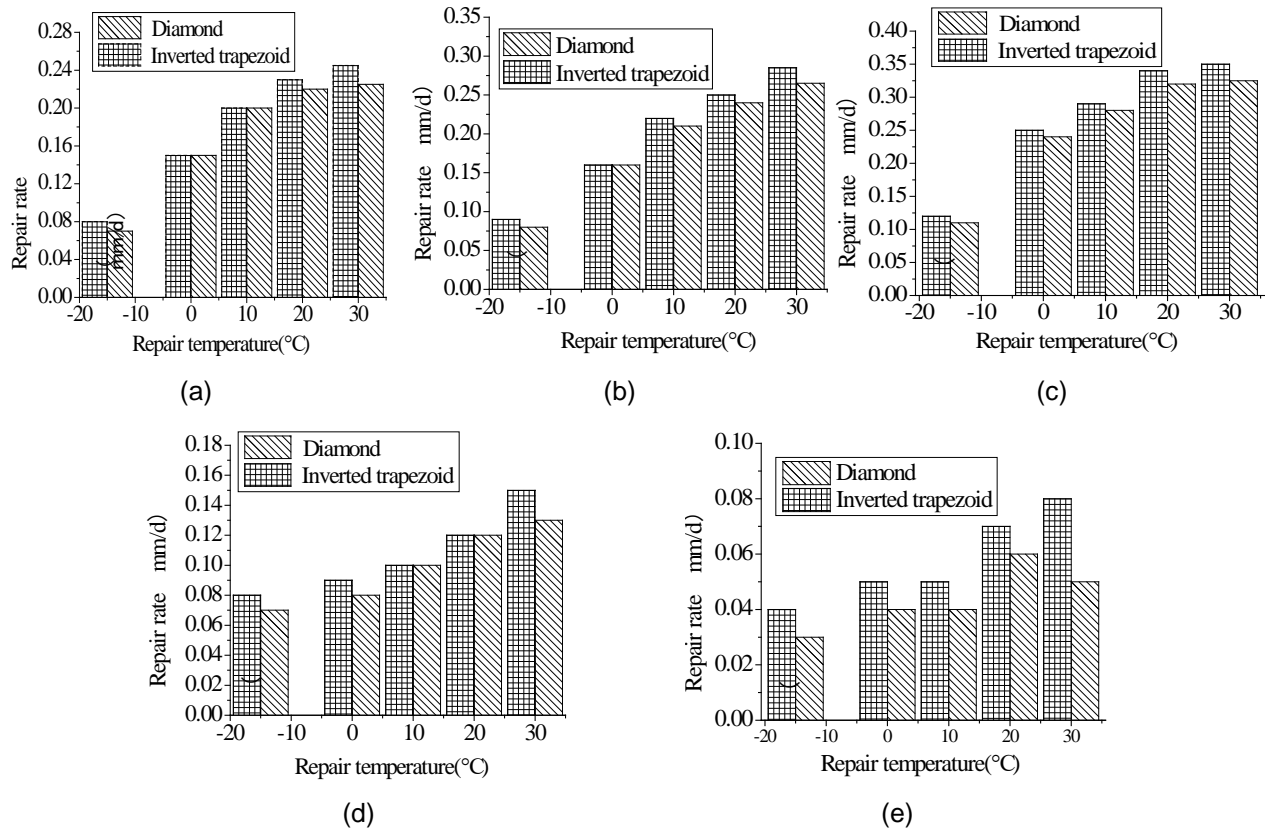


Figure 12. Change in repair rate as the fiberglass tube is placed: a) Initial crack width is 0.4mm; b) Initial crack width is 0.6mm; c) Initial crack width is 1.0 mm; d) Initial crack width is 1.5 mm; e) Initial crack width is 2.0mm.

It can be seen from Figure 12 that when the initial crack width and the temperature condition of the repair are given, the repair rate of the glass fiber tube placed in the inverted trapezoid is slightly better than that of the diamond. When the glass fiber tube is trapezoidal, the glass fiber tube is arranged at the lower part. When the test piece is subjected to an external action, the lower part first generates a crack, and the adhesive which flows out after the lower glass tube is broken can be better. Repair the lower crack, and the position of the glass tube is diamond-shaped, the lower part of the adhesive flows out, the amount of adhesive required for the lower crack can not be guaranteed, and the smaller the crack, the worse the fluidity, part of the adhesive solidifies gradually during the flow and the fluidity is reduced, so the crack cannot be repaired quickly.

According to the comparison with the existing research results, it can be concluded: The change of temperature condition has a great influence on the repair rate. In a certain temperature range, the higher the temperature, the faster the repair rate is. The repair rate increases firstly and then decreases with the increase of the initial crack width, and the repair rate reaches the highest level when the initial crack width is about 1.0 mm. When the initial crack width and the temperature condition of the repair are given, the repair rate of the glass fiber tube is slightly better than that of the diamond when the inverted trapezoid is placed. The initial width of the crack has the greatest influence on the repair rate, followed by the temperature condition and the placement of the fiberglass tube. The corresponding factor levels at the maximum repair rate are 1.0 mm, 30 °C and inverted trapezoids.

4. Conclusion

(1) At $-15\sim 30$ °C, the repair rate increases with the increase of temperature; at $0\sim 30$ °C, the growth rate of repair rate is significantly lower than the growth rate of $-15\sim 0$ °C. When the temperature is below 0 °C, the temperature plays a leading role in improving the repair rate. When the temperature rises, the repair rate increases rapidly; when the temperature is higher than 0 °C, the temperature is not the main factor affecting the repair rate. The above studies have important reference value for temperature-affected repair rate.

(2) When the crack width is 0.4 mm to 0.6 mm, the repair rate is significantly faster than the crack width of 0.6 mm to 1.0 mm. The repair rate of the crack width from 1.0 mm to 1.5 mm is significantly higher than the crack width of 1.5 mm to 2.0 mm. When the initial crack width is about 1.0 mm, the repair rate reaches the highest level. The study shows that as the initial crack width increases, the repair rate increases first and then decreases, which is important for the effect of the initial crack width on the repair rate.

(3) This study shows us that when the initial crack width and repair temperature is $-15\sim 30\text{ }^{\circ}\text{C}$, the repair rate of the glass fiber tube is slightly better than that of the diamond when the inverted trapezoid is placed. It is very valuable to study the effect of the location of the repair material on the repair effect.

(4) The initial width of the crack in this study had the greatest impact on the repair rate, followed by the temperature conditions and the placement of the fiberglass tube. The corresponding factor level under the maximum repair rate is 1.0mm, $30\text{ }^{\circ}\text{C}$ and inverted trapezoid, which is of great significance for the study of the repair effect under the same conditions.

References

1. Shen, A.-Q., Zhu, J.-H., Wang, X.-F., Zhong, J.-C., Fu, Q. Performance and mechanism of polymer modified superfine cement for microcrack mending of concrete structure. China Journal of Highway and Transport. 2006.19(4). Pp. 46–51+58.
2. Wen, W. Key techniques study on cement pavement maintained. Dissertation. South China University of Technology, 2009.
3. Shen, A.-Q. Study on the crack mending materials of cement concrete pavement. Dissertation. Chang'an University. 2005.
4. Yang, Q. The technology research on repairing cracks of prestressed concrete pavement. Dissertation. Changsha University of Science & Technology, 2013.
5. Liu, X., Yao, W., Zheng, X. et al. Experimental study on self-healing performance of concrete. Journal of Building Materials. 2005.No. 2. Pp.184–188.
6. Wang, G. Studies on chemical change type self-healing material for cracks and its influence on durability of concrete. Dissertation. Wuhan University of Technology, 2005.
7. Sahmaran, M., Li, M.V.C. Durability of mechanically loaded engineered cementitious composites under highly alkaline environments. Cement and Concrete Composites. 2008. 30(2). Pp.72–81.
8. Jiao, J., Hongyu, X.U., Han, W.U. Construction theory and key technology of ultra-thick bottom plate of Xinda International Finance Centre. Construction Technology, 2017.
9. Pelletier, M., Bose, A. Self-mending composites incorporating encapsulated mending agents. ACI. 2011.16(3). P.456.
10. Zanotti, C., Borges, P.H.R., Bhutta, A., et al. Bond strength between concrete substrate and metakaolingeopolymer repair mortar: Effect of curing regime and PVA fiber reinforcement. Cement & Concrete Composites. 2017.No. 80. Pp.307–317.
11. Wei, S.S. Application of shallow grouting technology in maintenance and repair of cement concrete pavement of expressway[J]. Construction & Design for Engineering, 2017.
12. Wang, Y., Sun, D., Han, Q. Detection and treatment of corrosion in the side plate and bottom plate of converter gas holder. Metallurgical Power, 2018.
13. Skominas, R., Gurskis, V., Sadzevicius, R. et al. Evaluation of cement mortar suitability for repairing concrete in hydraulic structures. Ksce Journal of Civil Engineering. 2017.No. 6. Pp.1–7.
14. Cheng, P., Wei, Y.. Study on the performance of adhesive in the Self-healing concrete. Science Technology and Engineering. 2017. 17(17). Pp.292–296.
15. Ashofteh, Y.K., Bolhari, B., Sabetmoghaddam, T., et al. Effect of blood exposure on push-out bond strength of four calcium silicate based cements. Iranian Endodontic Journal. 2017. 12(2). Pp.196–200.
16. Jin, M., Feng, X., Feng, L., et al. Superhydrophobic aligned polystyrene nanotube films with high adhesive force. Advanced Materials. 2010. 17(16). Pp.1977–1981.
17. Drass, M., Schwind, G., Schneider, J. et al. Adhesive connections in glass structures—part I: experiments and analytics on thin structural silicone. Glass Structures & Engineering. 2018. 3(1). Pp.39–54.
18. Shen, C. The Research of Self-healing Concrete with PUA Fibers. Dissertation. Chong Qing Jiao Tong University, 2011.
19. Li, J.S., Guo, M.Z., Xue, Q. et al. Recycling of incinerated sewage sludge ash and cathode ray tube funnel glass in cement mortars. Journal of Cleaner Production. 2017. 152. Pp.142–149.
20. Kuang, Y., Ou, J. Experiments and Analyses of the Self-healing of Cracks in Reinforced Concrete Beams with Embedded Fibers Filled with Adhesive[J]. China Civil Engineering Journal. 2005. No. 4. Pp.53–59.
21. Karihaloo, B.L., Keer L.M., Nemat-Nasser, S. Crack kinking under nonsymmetric loading. Engineering Fracture Mechanics. 2016. Vol. 13(4). Pp. 879–888.

Contacts:

Qianqian Zhao, 045188028393; 492954791@qq.com
Peifeng Cheng (Corresponding Author), 13946139402; chengpeifeng@126.com*
Yuwei Wei, 13783869126; weiyuwei1991@qq.com
Jianwu Wang, 13603625185; nihaone@163.com

© Zhao, Q., Cheng, P., Wei, Y., Wang, J., 2019



DOI: 10.18720/MCE.88.6

The modeling method of discrete cracks and rigidity in reinforced concrete

V.I. Kolchunov*, A.I. Dem'yanov,
Southwest State University, Kursk, Russia.
* E-mail: vlik52@mail.ru

Keywords: reinforced concrete, crack fault, bending-torsional coupling, computational models, splitting tensile strength.

Abstract. Cracks can be quite critical for the safety of architectural structures so their investigation is crucial. Excessive crack opening in reinforced concrete structures leads to corrosion of the reinforcement, which significantly reduces their serviceability. An extraordinary problem on the width of crack opening was considered for RC (reinforced concrete) elements under the affects of bending and torsion. Its solution was proposed on the basis of RC theory involving the hypotheses of fracture mechanics. The initial hypotheses about the formation and disclosure of spatial cracks for multilayer RC structures were formulated. These proposals allowed assessing the resistance of concrete in tension and the distance between the cracks, as well as the width of its disclosure. Hence, specific features of a double-cantilever element adjacent to spatial cracks were investigated with both mathematical calculations and experimental studies. The results demonstrated that developed new technique can be used for estimating the width of the spatial cracks for RC elements under the affects of bending and torsion.

1. Introduction

Excessive crack opening in reinforced concrete structures leads to corrosion of the reinforcement, which significantly reduces their serviceability. In addition, the resulting cracks significantly reduce the stiffness of reinforced concrete structures [1–8]. Nevertheless, despite the obvious and urgent need, a calculation model for a satisfactory assessment of the width of crack opening in reinforced concrete has not yet been developed [9–22], it is not very significant for the experiment and in some cases reaches more than 100%. Thus, this task is extraordinary. In this case, parameters, such as the distance between the cracks and resistance of the concrete in tension between the cracks, currently are not amenable to theoretical description. So the first of them changes discretely as the load increases, an extraordinary change of the second clearly requires the opening of some unknown up to the present time to a wide range of domestic and foreign researchers of the effect arising in the process of resistance to reinforced concrete.

The processes of the development and opening of cracks in elements of reinforced concrete structures are a rather complicated phenomenon, for the phenomenological description of which it is necessary to involve a number of hypotheses about the joint work of two materials. Its analysis becomes more complicated by the fact that the main hypothesis of the mechanics of a solid deformable body (the continuity hypothesis) is not applicable here – the integrity is broken with the formation of macro cracks. The use of simplified approaches is also impossible here, since the inaccuracy allowed in this case exceeds the value of the characteristic a_{cr} , measured in experiments using a microscope.

The problem is further complicated by the fact that along with regular cracks in reinforced concrete there are discrete cracks with different criteria for their formation and development [2, 4, 18–21]. Here, the main role is played by the concentration of deformations in places of abrupt changes in geometric dimensions, zones of concentration of force and deformation loading, inter-media concentration. However, to this day, a technique for modeling discrete cracks, including the use of modern computer systems known in the world, has not been developed. Therefore, to date, the task has not been satisfactorily solved.

Kolchunov, V.I., Dem'yanov, A.I. The modeling method of discrete cracks and rigidity in reinforced concrete. Magazine of Civil Engineering. 2019. 88(4). Pp. 60–69. DOI: 10.18720/MCE.88.6.

Колчунов В.И., Демьянов А.И. Неординарная задача о раскрытии трещин в железобетоне // Инженерно-строительный журнал. 2019. № 4(88). С. 60–69. DOI: 10.18720/MCE.88.6



This open access article is licensed under CC BY 4.0 (<https://creativecommons.org/licenses/by/4.0/>)

2. Methods

In order to fill the existing gap in reinforced concrete, the following is the essence of the proposed method for calculating the crack opening width taking into account the effect of discontinuity, incompatibility of deformations of concrete and reinforcement in conditions of complex torsional resistance with bending. At the same time, it was experimentally revealed that the crack has a complex profile, and not a triangular one, as it happens in the kinematic scheme of deformation. The laws of crack formation have been studied (it has been established that there are several of these levels, not just one, as is customary in the theory of V.I. Murashev). introduced a new classification of basic spatial cracks.

It should be noted that the designated research occurs Dilemm 1-alignment values experienced and theoretical parameters. It is important to emphasize the fact that in the development of methods and testing, as a rule, the installation of electrical strain gauges is performed before loading the reinforced concrete structure. In this case, already at the initial loading steps, the formed cracks intersect most of the installed electrical strain gauges and, thus, destroy them. With the advent of the relatively new glue «Cyacrine», the installation of electrical strain gauges can be performed after the formation of macrocracks, in which case it work until the stage of destruction. In this case, the possibility of their installation directly on the banks of the crack appears. The «trap» scheme is also new, which allows to obtain of information about the deformed state of concrete in the vicinity of the crack tip [5–9].

To be fair, it should be noted that, as applied to integral parameters, for example, deflections, the theory of reinforced concrete using the model of averaged section gives quite satisfactory results when comparing experimental and theoretical values. However, considering such a differential parameter as the width of crack opening, this is not observed, the differences can reach 400 % or more.

At first glance, it would seem, everything is clear and simple – the width of the a_{crc} crack opening determines the difference between the deformations of reinforcement and concrete in the area between the cracks:

$$a_{crc} = (\varepsilon_{S,m} - \varepsilon_{bt,m}) \cdot l_{crc} \approx \varepsilon_S \cdot \psi_S \cdot l_{crc}. \quad (1)$$

However, the parameters included in this formula l_{crc} (the distance between the cracks) and ψ_s (the factor of accounting for the work of stretched concrete between the cracks) turned out to be very problematic in their experimental determination.

When solving the designated problem occurs Dilemm 2: either to re-develop the mechanics of reinforced concrete, which will take more than one decade, or rely on the existing provisions of fracture mechanics, which has been developing for a whole century and is studying the stress-strain state in the vicinity of cracks. It is clear that the second way is much more logical. here fore, today, the main focus of scientific research by the authors was to develop two-console elements of fracture mechanics in relation to reinforced concrete, including a crack, so that later using them to build models of reinforced concrete deformation based on hypotheses and fine tools of fracture mechanics.

Discovery of the discontinuity effect [5-9] allowed to reach a completely different level of development of two-console elements for reinforced concrete [2, 4, 6, 7]. The laws of crack formation were studied (it was established that there are several of these levels, and not one, as is customary in the theory of V.I. Murashev [6]). It was established experimentally that the crack has a complex profile, and not a triangular one, as it happens in the kinematic deformation scheme; studied the patterns of deformation in the layers adjacent to the seam between the concrete.

Continuing these studies [1, 4–6], we will proceed from the functional of fracture mechanics, which relates the rate of energy ζ_{bu} release during the formation of new specific surfaces of a spatial crack in the pre-fracture zone:

$$\zeta_{bu} = \lim_{\delta A \rightarrow 0} \left(\frac{\delta W - \delta V}{\delta A} \right) = \frac{dW}{dA} - \frac{dV}{dA}. \quad (2)$$

where δV is decrease in the potential energy of the body during crack propagation by a small increment δA ; δW is additional work done on the body as the crack advances by a small increment δA .

At the same time, the reduction of the potential energy of the body during crack propagation and the additional work accomplished in this case can be expressed through the flexibility of the crack faces by cutting out the double-cantilever element (DCE) including the crack. This approach allows preserving the physical meaning of the dependencies obtained, unlike using the Gursa function with complex numbers [3, 4, 6, 7].

In the case of using a short double-cantilever unit, when h_{crc} is known, the parameters $X_1 = \Delta T$, $X_2 = P_{bt,c}$, ..., X_n can be determined using conventional methods of structural mechanics [4, 7, 8].

A new classification of discrete basic spatial cracks in reinforced concrete structures (including compound ones) is given in [4]. It distinguishes between geometric, force (deformation), inter-media concentration for basic discrete cracks, and a method is proposed for finding adjacent cracks. Additionally, the cracks are divided into three types depending on the conditions of their formation and the intersection of the working reinforcement during their development.

The method of calculating reinforced concrete composite structures for the formation, development and disclosure of spatial cracks (with the ability to estimate the resistance of stretched concrete between cracks, the width of their disclosure and the distance between them) is based on the following working premises:

- for medium deformations of concrete and reinforcement, the hypothesis of flat sections is considered to be valid (in the case of a composite structure, within each of the rods included in the composite rod); stresses in concrete and reinforcement are determined using three- and bilinear bond diagrams σ – ε , respectively;
- the formation of spatial cracks occurs after the main deformations of the elongation of concrete reach their limiting values $\varepsilon_{bt,u}$; in the process of loading several levels of crack formation are distinguished; the distance between the cracks of the next level is within the distance between the cracks of the previous level, dividing it through the parameter η ;
- introduced a classification of discrete basic spatial cracks in reinforced concrete (including composite) structures;
- the connection between the adhesion stress τ and relative conditional mutual displacement of the two concrete $\varepsilon_{q,b}$ and concrete and reinforcement $\varepsilon_g(x)$ is taken in the form: $\tau(x) = G(\lambda)\varepsilon_g(x)$, where $G(\lambda)$ – equivalent modulus of deformation of adhesion between concrete (or reinforcement and concrete)
- additional deformation effect in the crack and change of its profile are considered, which are associated with the violation of material integrity;
- crack opening is the accumulation of relative conditional mutual displacements of reinforcement and concrete in areas located on both sides of the crack, taking into account the features caused by the effect of discontinuity (Figure 1), – the upgraded Thomas hypothesis;
- takes into account distortion of normals to the cross section of concrete element in a location with a crack depending on the distance from the contact surface with reinforcement to the surface of the structure.

From Figure 1 it follows that the relative mutual displacements of reinforcement and concrete are determined from the dependence:

$$\varepsilon_g(y) = \varepsilon_s(y) - \varepsilon_{bt}(y), \quad (6)$$

where $\varepsilon_s(y)$ and $\varepsilon_{bt}(y)$ are relative deformations of reinforcement and relative deformations of concrete in section x , respectively.

Then, after differentiation, the solution of a nonhomogeneous differential equation of the first order is:

$$\varepsilon_g(y) = \left(\varepsilon_{sw} + \frac{\Delta T}{E_{sw}A_{sw}} - \frac{\sigma_{bt,c}}{\nu_b E_b} - \frac{D_{14}}{D_{13} \cdot B} \right) e^{-By} - \frac{D_{14}}{D_{13} \cdot B}. \quad (7)$$

The distance between the cracks l_{crc} is determined using the second prerequisite:

$$l_{crc} = \frac{2(\ln B_4 - Bt_*)}{-B}. \quad (8)$$

Variables $D_{i,j}$, B , B' , B'_4 , entering into formulas (7) and (8), are functions of boundary deformations of concrete elongation, parameters that take into account the effect of concrete discontinuity (ΔT , $P_{bt,c}$), geometric characteristics and characteristics of reinforcement and concrete adhesion [4];

The emergence of a new level of cracking corresponds to the fulfillment of inequality:

$$l_{crc,i} \leq \eta l_{crc,i-1}, \quad (9)$$

where η – the ratio of the distances between the cracks when it is divided at the subsequent level. Having the parameters $\varepsilon_g(y)$ and $\varepsilon_{bt}(y)$ it is easy to write the parameter $\varepsilon_s(y)$.

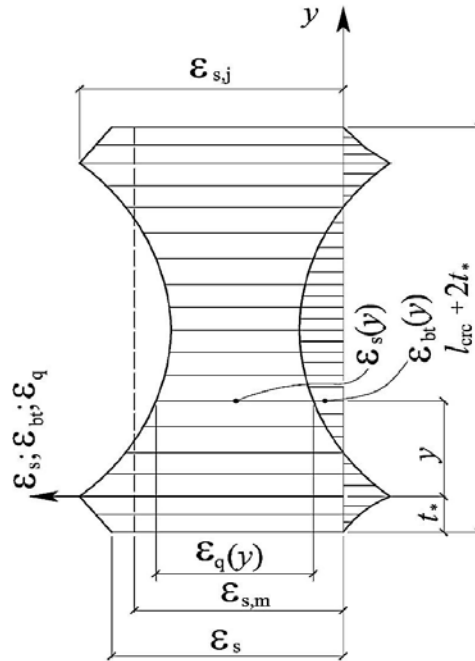


Figure 1. Diagrams of concrete deformations $\varepsilon_{bt}(y)$, reinforce $\varepsilon_s(y)$ and their relative mutual displacements $\varepsilon_g(y)$ in the area between spatial cracks in reinforced concrete structures in torsion with bending

Integration $\varepsilon_s(y)$ within the distance between the cracks l_{crc} allows to obtain the value of the coefficient of the work of the stretched concrete ψ_s by the formula:

$$\psi_s = \frac{2 \cdot K \cdot B_3}{\varepsilon_s \cdot l_{crc} \cdot B} \cdot \left[1 - e^{-B \cdot (0.5l_{crc} - t_*)} \right] + \frac{2}{\varepsilon_s \cdot l_{crc}} \left(\varepsilon_s + \frac{\Delta T}{E_S A_S} - K \cdot B_3 \right) \cdot (0.5l_{crc} - t_*) + \frac{\delta Q \cdot K}{\varepsilon_s \cdot l_{crc} \cdot B \cdot t_*} (0.5l_{crc} - t_*)^2 + \frac{2 \cdot \varepsilon_s \cdot E_S \cdot A_S + \Delta T}{\varepsilon_s \cdot l_{crc} \cdot E_S \cdot A_S} \cdot t_* \quad (10)$$

Thereafter, in accordance with the sixth prerequisite, the task, by definition a_{crc} , is reduced to finding the relative mutual displacements $\varepsilon_g(y)$ of reinforcement and concrete in different areas between cracks:

$$a_{crc} = 2 \int_0^{t_*} \varepsilon_g(y_1) dy_1 + \int_{t_*}^{\eta \cdot l_{crc}} \varepsilon_g(y) dy + \int_{\eta \cdot l_{crc}}^{l_{crc} - t_*} \varepsilon_g(y) dy \quad (11)$$

After integration and algebraic transformations, we obtain:

$$\lambda_3 = - \frac{k_1}{(k_2 - 1)C_2^2 - C_2} \quad (12)$$

When performing practical calculations, one should take into account distortion of normals to the cross section of concrete element depending on the distance of the reinforcement surface to the concrete surface. For this purpose, a cantilever design scheme is used to determine the movements of the crack faces, selected in the zone of the protective layer [6, 7]. Displacements in the zone of the protective layer $y_{pr,l}$ are determined using the method of initial parameters.

In turn, the processing of such data allows to obtain the following dependence:

$$2f_R = \frac{2 \cdot 0,0163 \cdot 100 \cdot \sigma_s \cdot (1 - e^{-0,516 \cdot r}) \cdot 10}{100 \cdot R_s} \quad (13)$$

Here the values σ_s and R_s are accepted in kN/cm^2 , and value f_R in mm.

The ratio of the calculated displacement in the zone of the protective layer $y_{pr,l}$ to the experimental displacements in the zone f_R under consideration shows that if the value of the protective layer differs from the baseline (assumed to be equal to the diameter of the working reinforcement), then before accumulating a sufficient amount of experimental data and carrying out a comparative analysis, it is accepted to include the coefficient $k_{r,dep}$:

$$k_{r,dep} = \frac{y_{pr,l}}{f_R}. \quad (14)$$

Taking into account the noted, the width of the crack opening at the level of the protective layer will be found by the formula:

$$a_{crc,tot} = a_{crc,S} + 2 \cdot \frac{y_{pr,l}}{k_{r,dep}}. \quad (15)$$

Here $a_{crc,s}$ is determined by the formulas obtained with the base value of the protective layer.

The solution of an extraordinary problem of the width of crack opening in reinforced concrete at the modern level of evolution of the theory of reinforced concrete with the involvement of fracture mechanics hypotheses is proposed. Simplified dependences are constructed for the energy functional and the specifics and features of the construction of the double-cantilever element of fracture mechanics in the zones adjacent to spatial cracks are considered, taking into account the discontinuity effect. The dual console element is a link and serves as a transformational element between the dependencies of fracture mechanics and the equations of the theory of reinforced concrete. The developed method makes it possible to estimate the resistances of reinforced concrete structures under various force and deformation effects, including torsion with bending.

4. Conclusions

1. As a result of scientific research, it has been established that the main hypothesis of the mechanics of a solid deformable body (continuity hypothesis) is not applicable when evaluating the resistance of reinforced concrete structures – continuity is broken with the formation of macro-cracks. The use of simplified approaches is also impossible here, since the error allowed in this case exceeds the value of the most sought a_{crc} , characteristic measured in experiments with a microscope. Therefore, to date, the task has not been satisfactorily solved.

2. When conducting research, there are several designated priority dilemmas, Dilemma 1-alignment values experienced and theoretical parameters. Dilemma 2: either to re-develop the mechanics of reinforced concrete, which will take more than one decade, or rely on the existing provisions of fracture mechanics, which has been developing for a whole century and is studying the stress-strain state in the vicinity of cracks. It is important to emphasize the fact that in the development of methods and testing, as a rule, the installation of electrical strain gauges is performed before loading the reinforced concrete structure. In this case, already at the initial loading steps, the formed cracks intersect most of the installed electrical strain gauges and, thus, destroy them. With the advent of the relatively new glue “Cyacrine”, the installation of electrical strain gauges can be performed after the formation of macrocracks, in which case it works until the stage of destruction. In this case, the possibility of their installation directly on the banks of the crack appears. The «trap» scheme is also new, which allows to obtain information about the deformed state of concrete in the vicinity of the crack tip

3. It has been established that, as applied to integral parameters for assessing the strength and deflection of reinforced concrete spatial structures, the use of the average section model yields quite satisfactory results when comparing experimental and theoretical values. However, considering such a differential parameter as the width of crack opening, this is not observed, the differences can reach 400 % or more.

4. The discovery of the discontinuity effect allowed us to reach a completely different level of development of double-cantilever elements for reinforced concrete. It was experimentally revealed that the crack has a complex profile, and not a triangular one, as it happens in the kinematic deformation scheme. The laws of crack formation have been studied (it has been established that there are several levels, not one, as is customary in the theory of V.I. Murashev).

5. It has been established that the decrease in the potential energy of the body during the crack propagation and the additional work accomplished in this case can be expressed in terms of the flexibility of the crack faces by cutting out the double-cantilever element (DCE), including the crack. In this case, displacements in any sections are determined by methods of structural mechanics.

This approach allows us to preserve the physical meaning of the dependencies obtained, in contrast to the use of the Goursat function with complex numbers.

6. As applied to a cut-out double-cantilever element under the influence of a number of forces ΔT , P_1 , P_2 , q , M_{con} , etc.), the functional of fracture mechanics takes on the form suitable for solving the problem of resistance of reinforced concrete structures under torsion with bending. A number of dependencies follow from it, including the connecting tangential force ΔT arising in the immediate vicinity of a crack with the length of its development through a concrete constant ζ_{bu} .

7. Isolation of DCE for reinforced concrete (which is transformational between the dependencies of fracture mechanics and the theory of reinforced concrete) is a very important but difficult task.

First, it must be linked not only with the task of determining the stress-strain state of the cross section of a reinforced concrete element, but also with the task of distributing adhesion between the reinforcement and the concrete, since the appearance of a crack in a solid body can be viewed as a certain deformation effect affecting the features adhesion of reinforcement and concrete in areas adjacent to the crack. It is also important to determine the length of the crack h_{crc} .

Secondly, the efforts in sections that pass at a distance of $t \text{ и } \Delta b$ for the double-cantilever element from the crack must be associated with the desired parameters of the stress-strain state of the reinforced concrete element.

Thirdly, we should not forget about the virtual movements of the dedicated DCE consoles when the neutral axis of the reinforced concrete element is rotated and the angles of rotation of the working reinforcing bar caused by arcing, i.e., the clamping of the consoles on both sides of the DCE may not be completely rigid in some cases.

8. Finding the projection of a spatial crack C is advisable to perform using the Lagrange function and multipliers for many variables. Then, from the condition of extremum of a function of several variables $F_{1,2} = f(q_{sw}, x_B, \sigma_s, x, \sigma_b, \sigma_{s,I}, \sigma_{b,1}, C_2, \dots, \lambda_1, \lambda_2, \lambda_3, \lambda_4, \lambda_5, \lambda_6, \lambda_7, \dots)$, and the equalities resulting from it to zero of the corresponding partial derivatives, the projection of the spatial crack C is sought and the region of the cut DCE specified.

9. The initial hypotheses to calculating reinforced concrete structures, including multilayer, to the formation, development and disclosure of spatial cracks are formulated. These proposals allow to assess the resistance of concrete in tension and the distance between the cracks, the width of its disclosure. This takes into account the additional deformation effect in the crack and the change in its profile associated with the violation of the material continuity. It also takes into account t distortion of normals to the cross section of concrete element in a location with a crack, that depends on the distance from the contact surface with the reinforcement to the external surface of the structure.

10. A new classification of discrete basic spatial cracks in reinforced concrete structures (including composite ones) is introduced, in which geometric, force (deformation), inter-media concentrations for basic discrete cracks are distinguished and a technique is proposed for finding adjacent cracks; Additional cracks are divided into three types depending on the conditions of their formation and the intersection of the working reinforcement during their development.

An extraordinary problem on the width of crack opening in reinforced concrete is considered and its solution is proposed at the modern level of evolution of reinforced concrete theory involving the hypotheses of fracture mechanics. Formulated are working prerequisites for building a methodology for calculating reinforced concrete structures, including compound ones, by education, development and disclosure of spatial cracks (with the possibility of estimating the resistance of concrete in tension and the distance between cracks, the width of their opening). This takes into account the additional deformation effect in the crack and the change in its profile associated with the violation of the integrity of the material; It also takes into account distortion of normals to the cross section of concrete element in a location with a crack, depending on the distance from the contact surface with the reinforcement to the surface of the structure.

The discovery of the discontinuity effect made it possible to reach a completely different level of development of double-cantilever elements for reinforced concrete. Specific features and features of the construction of a double-cantilever element of fracture mechanics in the zones adjacent to spatial cracks with regard to the effect of discontinuity are considered.

The dual console element is a link and serves as a transformational element between the dependencies of fracture mechanics and the equations of the theory of reinforced concrete. The developed method makes it possible to estimate the resistances of reinforced concrete structures under various force and deformation effects, including torsion with bending.

References

1. Fang, G., Yang, Y., Ge, Y. Flutter performance of PK section girders for long-span bridges. *Journal of Vibration and Shock*. 2018. 37(9). Pp: 25–31. DOI: 10.13465/j.cnki.jvs.2018.09.004
2. Emelyanov, S., Nemchinov, Y., Kolchunov, V., Yakovenko, I. Details of large-panel buildings seismic analysis. *Enfoque UTE*. 2016. 7(2). Pp. 120–134. URL: <http://oaji.net/articles/2016/1783-1467383650.pdf>
3. Wang, Z., Fratarcangeli, M., Ruimi, A., Srinivasa, A.R. Real time simulation of inextensible surgical thread using a Kirchhoff rod model with force output for haptic feedback applications. *International Journal of Solids and Structures*. 2017. Vol. 113-114. Pp: 192–208. DOI: 10.1016/j.ijsolstr.2017.02.017
4. Salnikov, A., Kolchunov, V.I., Yakovenko, I. The computational model of spatial formation of cracks in reinforced concrete constructions in torsion with bending. *Applied Mechanics and Materials*. 2015. Vols. 725–726. Pp. 784–789.
5. Kolchunov, V.I., Dem'yanov, A.I. The modeling method of discrete cracks in reinforced concrete under the torsion with bending. *Magazine of Civil Engineering*. 2018. 81(5). Pp. 160–173. doi: 10.18720/MCE.81.16.
6. Stepanov, V.B. The method of corrosion crack opening evaluation for the reinforced concrete structures technical state assessment. *Magazine of Civil Engineering*. 2012. 31(5). Pp. 6-11. (rus). DOI: 10.5862/MCE.31.1.
7. Iakovenko, I., Kolchunov, V.I. The development of fracture mechanics hypotheses applicable to the calculation of reinforced concrete structures for the second group of limit states. *Journal of Applied Engineering Science*. 2017. Vol. 3. Pp. 366–375. Doi:10.5937/jaes15-14662.
8. Iakovenko, I., Kolchunov, V., Lyman, I. Rigidity of reinforced concrete structures in the presence of different cracks. *MATEC Web of Conferences*. 2017. Vol. 116. Pp. 1–12. Doi: 10.1051/mateconf/201711602016
9. Vatin, N.I., Ivanov, A.Yu., Rutman, Y.L., Chernogorskiy, S.A., Shvetsov, K.V. Earthquake engineering optimization of structures by economic criterion. *Magazine of Civil Engineering*. 2017. 76(8). Pp. 67–83. doi: 10.18720/MCE.76.7.
10. Jariwalaa, V.H., Patel, P.V., Purohit, S.P. Strengthening of RC Beams subjected to Combined Torsion and Bending with GFRP Composites. *Procedia Engineering*. 2013. Vol. 51. Pp. 282–289.
11. Rahal, K.N., Collins, M.P. Compatibility Torsion in Spandrel Beams Using Modified Compression Field Theory. *ACI Structural Journal*. 2006. Vol. 103. No. 3. Pp. 328–338.
12. Chandrasekaran, E., Dhanaraj, R., Santhakumar, R. Behaviour of retrofitted reinforced concrete beams under combined bending and torsion: A numerical study. *Electronic Journal of Structural Engineering*. 2007. No. 7. Pp. 1–7.
13. Ehrhardt, D.A., Hill, T.L., Neild, S.A., Cooper, J.E. Veering and nonlinear interactions of a clamped beam in bending and torsion. *Journal of Sound and Vibration*. 2018. Vol. 416. Pp. 1–16.
14. Gil-Martín, L.M., Hernández-Montes, E. Safety levels of the traditional strength design of RC slabs under bending and torsion. *Engineering Structures*. 2016. Vol. 127. Pp. 374–387. Doi: 10.1016/j.engstruct.2016.08.063
15. Hosseini, F., Gencturk, B., Aryan, H., Cadaval, G. Seismic behavior of 3-D ECC beam-column connections subjected to bidirectional bending and torsion. *Engineering Structures*. 2018. Vol. 172. Pp. 751–763. Doi: 10.1016/j.engstruct.2018.06.054
16. Xu, J., Diao, B., Guo, Q., Ye, Y., Mo, Y.L., Chen, H. Interaction of bending, shear and torsion in U-shaped thin-walled RC girders. *Engineering Structures*. 2019. Vol. 179. Pp. 655–669. Doi: 10.1016/j.engstruct.2018.11.011
17. Bernard, L., Michon, G., El Fatmi, R., Castanié, B. Static and dynamic analysis of bending–torsion coupling of a CFRP sandwich beam. *Composite Structures*. 2016. Vol. 145. Pp. 26–36. Doi: 10.1016/j.compstruct.2016.02.055
18. Nie, X., Wang, Y.-H., Li, S., Chen, J. Coupled bending-shear-torsion bearing capacity of concrete filled steel tube short columns. *Thin-Walled Structures*. 2018. Vol. 123. Pp. 305–316. Doi: 10.1016/j.tws.2017.11.026
19. Ogawa, Y., Kawasaki, Y., Okamoto, T. Fracture behavior of RC members subjected to bending shear and torsion using acoustic emission method. *Construction and Building Materials*. 2014. Vol. 67. Pp. 165–169. Doi: 10.1016/j.conbuildmat.2014.05.100
20. Lukina, A.A., Kholopova, I.S., Alpatova, V.Y., Solovieva, A.V. Beams with corrugated web: calculation peculiarities of bending torsion analysis. *Procedia Engineering*. 2016. Vol. 153. Pp. 414-418. Doi: 10.1016/j.proeng.2016.08.143
21. Staupendahl, D., Tekkaya, A.E. The reciprocal effects of bending and torsion on springback during 3D bending of profiles. *Procedia Engineering*. 2017. Vol. 207. Pp. 2322–2327. Doi: 10.1016/j.proeng.2017.10.1002
22. Kashani, M.T., Hashemi, S.M. A finite element formulation for bending-torsion coupled vibration analysis of delaminated beams under combined axial load and end moment. *Shock and Vibration*. 2018. Vol. 2018. Pp: 1348970. DOI: 10.1155/2018/1348970

Contacts:

Vladimir Kolchunov, +79103154850; vlik52@mail.ru

Alexey Dem'yanov, +74712222461; speccompany@gmail.com

© Kolchunov, V.I., Dem'yanov, A.I., 2019



DOI: 10.18720/MCE.88.6

Неординарная задача о раскрытии трещин в железобетоне

В.И. Колчунов*, А.И. Демьянов,

Юго-Западный государственный университет, г. Курск, Россия

* E-mail: vlik52@mail.ru

Ключевые слова: железобетонные конструкции, пространственные трещины, кручение с изгибом, двухконсольная модель, сопротивление растянутого бетона.

Аннотация. Рассмотрена неординарная задача о ширине раскрытия трещин в железобетоне и предложено ее решение на современном уровне эволюции теории железобетона с привлечением гипотез механики разрушения. Сформулированы рабочие предпосылки для построения методики расчета железобетонных конструкций, в том числе составных, по образованию, развитию и раскрытию пространственных трещин (с возможностью оценки сопротивления растянутого бетона и расстояния между трещинами, ширины их раскрытия). При этом учитывается дополнительное деформационное воздействие в трещине и изменение ее профиля, связанные с нарушением сплошности материала; также учитывается депланация бетона в сечении с трещиной в зависимости от расстояния от поверхности контакта с арматурой до поверхности конструкции. Открытие эффекта нарушения сплошности позволило выйти на совершенно иной уровень разработки двухконсольных элементов для железобетона. Тем не менее, до сегодняшнего дня методика моделирования дискретных трещин, в том числе с использованием известных в мире современных вычислительных комплексов не разработана, что не дает возможности эффективного (без излишних запасов) расчета и проектирования железобетонных конструкций в условиях сложного сопротивления – кручения с изгибом с обеспечением необходимой жесткости и антикоррозионной стойкости. Рассмотрены специфика и особенности построения двухконсольного элемента механики разрушения в зонах, прилегающих к пространственным трещинам с учетом эффекта нарушения сплошности. Двухконсольный элемент является связующим звеном и служит в качестве трансформационного элемента между зависимостями механики разрушения и уравнениями теории железобетона. Разработанная методика позволяет оценивать сопротивления железобетонных конструкций в условиях различных силовых и деформационных воздействий, в том числе при кручении с изгибом.

Литература

1. Fang G., Yang Y., Ge Y. Flutter performance of PK section girders for long-span bridges // Journal of Vibration and Shock. 2018. 37(9). Pp: 25-31. DOI: 10.13465/j.cnki.jvs.2018.09.004
2. Emelyanov S., Nemchinov Y., Kolchunov V., Yakovenko I. Details of large-panel buildings seismic analysis // Enfoque UTE. 2016. No. 7(2). Pp. 120–134. URL: <http://oaji.net/articles/2016/1783-1467383650.pdf>
3. Wang Z., Fratarcangeli M., Ruimi A., Srinivasa, A.R. Real time simulation of inextensible surgical thread using a Kirchhoff rod model with force output for haptic feedback applications // International Journal of Solids and Structures. 2017. Vol. 113-114. Pp: 192-208. DOI: 10.1016/j.ijsolstr.2017.02.017
4. Salnikov A., Kolchunov V.I., Yakovenko I. The computational model of spatial formation of cracks in reinforced concrete constructions in torsion with bending // Applied Mechanics and Materials. 2015. Vols. 725–726. Pp. 784–789.
5. Колчунов В.И., Демьянов А.И. Метод моделирования дискретных трещин в железобетоне при кручении с изгибом // Инженерно-строительный журнал. 2018. № 5(81). С. 160–173. doi: 10.18720/MCE.81.16.
6. Степанов В.Б. Методика определения ширины раскрытия коррозионных трещин для оценки технического состояния железобетонных конструкций // Инженерно-строительный журнал. 2012. №5. С. 6–11. DOI: 10.5862/MCE.31.1.
7. Iakovenko I., Kolchunov V.I. The development of fracture mechanics hypotheses applicable to the calculation of reinforced concrete structures for the second group of limit states // Journal of Applied Engineering Science. 2017. Vol. 3. Pp. 366–375. Doi:10.5937/jaes15-14662.
8. Iakovenko I., Kolchunov V., Lymar I. Rigidity of reinforced concrete structures in the presence of different cracks // MATEC Web of Conferences. 2017. Vol. 116. Pp. 1-12. Doi: 10.1051/mateconf/201711602016
9. Ватин Н.И., Иванов А.Ю., Рутман Ю.Л., Черногорский С.А., Швецов К.В. Оптимизация конструкций сейсмостойких сооружений по экономическому критерию // Инженерно-строительный журнал. 2017. № 8(76). С. 67–83. doi: 10.18720/MCE.76.7.
10. Jariwala V.H., Patel P.V., Purohit S.P. Strengthening of RC Beams subjected to Combined Torsion and Bending with GFRP Composites // Procedia Engineering. 2013. Vol. 51. Pp. 282–289.

11. Rahal K.N., Collins M.P. Compatibility Torsion in Spandrel Beams Using Modified Compression Field Theory // ACI Structural Journal. 2006. Vol. 103. No. 3. Pp. 328–338.
12. Chandrasekaran E., Dhanaraj R., Santhakumar R. Behaviour of retrofitted reinforced concrete beams under combined bending and torsion : A numerical study // Electronic Journal of Structural Engineering. 2007. No. 7. Pp. 1–7.
13. Ehrhardt D.A., Hill T.L., Neild S.A., Cooper J.E. Veering and nonlinear interactions of a clamped beam in bending and torsion // Journal of Sound and Vibration. 2018. Vol. 416. Pp. 1-16.
14. Gil-Martín L.M., Hernández-Montes E. Safety levels of the traditional strength design of RC slabs under bending and torsion // Engineering Structures. 2016. Vol. 127. Pp. 374–387. Doi: 10.1016/j.engstruct.2016.08.063
15. Hosseini F., Gencturk B., Aryan H., Cadaval G. Seismic behavior of 3-D ECC beam-column connections subjected to bidirectional bending and torsion // Engineering Structures. 2018. Vol. 172. Pp. 751–763. Doi: 10.1016/j.engstruct.2018.06.054
16. Xu J., Diao B., Guo Q., Ye Y., Mo Y.L., Chen H. Interaction of bending, shear and torsion in U-shaped thin-walled RC girders // Engineering Structures. 2019. Vol. 179. Pp. 655–669. Doi: 10.1016/j.engstruct.2018.11.011
17. Bernard L., Michon G., El Fatmi R., Castanié B. Static and dynamic analysis of bending–torsion coupling of a CFRP sandwich beam // Composite Structures. 2016. Vol. 145. Pp. 26–36. Doi: 10.1016/j.compstruct.2016.02.055
18. Nie X., Wang Y.-H., Li S., Chen J. Coupled bending-shear-torsion bearing capacity of concrete filled steel tube short columns // Thin-Walled Structures. 2018. Vol. 123. Pp. 305–316. Doi: 10.1016/j.tws.2017.11.026
19. Ogawa Y., Kawasaki Y., Okamoto T. Fracture behavior of RC members subjected to bending shear and torsion using acoustic emission method // Construction and Building Materials. 2014. Vol. 67. Pp. 165–169. Doi: 10.1016/j.conbuildmat.2014.05.100
20. Lukina A.A., Kholopova I.S., Alpatova V.Y., Solovieva A.V. Beams with corrugated web: calculation peculiarities of bending torsion analysis // Procedia Engineering. 2016. Vol. 153. Pp. 414-418. Doi: 10.1016/j.proeng.2016.08.143
21. Staupendahl D., Tekkaya A.E. The reciprocal effects of bending and torsion on springback during 3D bending of profiles // Procedia Engineering. 2017. Vol. 207. Pp. 2322-2327. Doi: 10.1016/j.proeng.2017.10.1002
22. Kashani M.T., Hashemi S.M. A finite element formulation for bending-torsion coupled vibration analysis of delaminated beams under combined axial load and end moment // Shock and Vibration. 2018. Vol. 2018. Pp: 1348970. DOI: 10.1155/2018/1348970

Контактные данные:

Владимир Иванович Колчунов, +79103154850; эл. почта: vlik52@mail.ru

Алексей Иванович Демьянов, +74712222461; эл. почта: spesscompany@gmail.com

© Колчунов В.И., Демьянов А.И., 2019



DOI: 10.18720/MCE.88.7

Reducing temperature difference in mass concrete by surface insulation

T.C. Nguyen^{a*}, X.B. Luu^b

^aMoscow State University of Civil Engineering, Moscow, Russia

^bTri Dung Construction Transportation Joint Stock Company, Dong Nai, Vietnam

* E-mail: ntchuc.mta198@gmail.com

Keywords: heat of hydration, temperature gradient, crack, mass concrete, mathematical model, sand-layer insulation.

Abstract. The heat which is produced in the cement hydration is rather high in mass concrete structures like dams, pavements, piers. In fact, it takes a longer time to cool the inner of the mass than its surface. The main reason for this result is that having the temperature difference between the hot inner mass and its cooled surface. Such a gap like that is the cause of appearing a large number of cracks in the surface of the mass concrete at several days age. In this study, the application of using a sand-layer insulation to control mass concrete block cracks at an early age. Specifically, these processes are performed by the program Midas Civil 2017 in cases: without sand-layer insulation, and with the application of using sand-layer insulation have thickness in range of 0–7 cm for heat preservation. In conclusion, the results in this study showed that when using an insulation thickness of 7 cm, it led to that the maximum temperature differences between the surface and the center of mass concrete block is lower than the limitation. The recommendations made as a result of this study is that sand-layer insulation should be used to prevent and limit cracks of the mass concrete block at an early age.

1. Introduction

The increase in temperature during concrete hardening is due to the exothermic hydration reactions of water and cement. This is important for massive elements, in which conditions are close to adiabatic temperature can reach in range of 50–90 °C has been described by ACI Committee [1–3]. The cause affecting the high-temperature rise and its non-uniform distribution between the surface and inside of thick slabs is low thermal conductivity of concrete, which slows down the natural cooling process. In the meantime, the shrinkage deformations are formed during the hydration of concrete as a result of a chemical reaction and the moisture exchange with the environment. According to published study, the result is on the surface of the concrete block in all the cracks [4–6].

There is a variety of methods and different prices to control the temperature of mass concrete such as low-heat materials, pre-cooling of concrete, posts-cooling of concrete. Each method has its advances depend on specific situations [7–9].

Surface heat preservation is an important measure for temperature control and cracks prevention. Many types of insulation materials are available in the world today, and insulation levels can be optimized to meet the required temperature differences in mass concrete. The selection of insulation material types and thicknesses are particularly important. So, based on that information can reduce the difference in temperature between the center and the surface of the concrete block by applying the insulation layer on the surface of the raft foundation, as can be seen in Figure 1.

Nguyen, T.C., Luu, X.B. Reducing temperature difference in mass concrete by surface insulation. Magazine of Civil Engineering. 2019. 88(4). Pp. 70–79. DOI: 10.18720/MCE.88.7

Нгуен Ч.Ч., Лью С.Б. Уменьшение разницы температур в монолитном бетоне за счет поверхностной изоляции // Инженерно-строительный журнал. 2019. № 4(88). С. 70–79. DOI: 10.18720/MCE.88.7



This open access article is licensed under CC BY 4.0 (<https://creativecommons.org/licenses/by/4.0/>)



Figure 1. Different types of insulation materials of the surface [10].

Thermal insulation is often used to warm the concrete surface and reduce the temperature difference, which in turn minimizes the thermal cracking ability. The surface insulation can significantly reduce the cooling rate while its effect on the maximum concrete temperature is not considered in most of the mass concrete pours. Insulation is inexpensive, but the result may be delayed due to by reducing the cooling rate, which can be costly. It is necessary to maintain the insulation for several weeks or longer because its surface could be cooled quickly and cracked when removing it too early. There are many types of insulation materials and its usage can be optimized to adapt to the requirement of temperature differences and maximize the cooling rate has been described by [11–12]. The small and medium-sized projects could also use straw bags and sand layers as insulation. The control of the thickness of the sand layer is conducted to determining the volume ratio on the sand was transported to the surface area of concrete blocks. However, with the structure has an inclined or vertical surface, the use of insulating sand layer is not effective, but in this situation could use polystyrene slab instead of sand insulation. The optimal time of putting or removing the sand layer on the block surfaces should be carefully considered based on the rate of strength development in concrete and the processing of heat of cement hydration. With high wind or heavy rain conditions, shielding methods must be taken to avoid sand erosion as well as undesirable sand thickness changes. Besides that, in order to collect of sand after use on the surface of the concrete is convenient should putting a layer of tarpaulin (or nylon) in advance, then spreading a sand layer on the tarpaulin.

The goal of this paper is to study the application of using sand-layer insulation to control mass concrete block cracks at an early age by finite element method using Midas Civil software 2017. The results show that using sand-layer insulation can considerably reduce maximum tensile stress.

2. Materials and methods

The study of the temperature regime of massive concrete blocks has been devoted to a rather large number of works carried out using modern methods. In this paper, applications by an insulating layer of sand to control the cracks of massive concrete blocks at the age of early days by finite element method using the software Midas civil 2017.

The solution to the temperature problem is based on the solution of the differential equation of the theory of heat conduction can be expressed as [13–16].

$$\frac{\partial}{\partial x} \left(k_x \frac{\partial t}{\partial x} \right) + \frac{\partial}{\partial y} \left(k_y \frac{\partial t}{\partial y} \right) + \frac{\partial}{\partial z} \left(k_z \frac{\partial t}{\partial z} \right) + q_v = \rho c \frac{\partial t}{\partial \tau}, \quad (1)$$

where t is the material temperature ($^{\circ}\text{C}$);

k_x, k_y, k_z are the thermal conductivity coefficients of the material dependent on the temperature in the directions x, y and z , respectively; ($\text{W}/\text{m}\cdot^{\circ}\text{C}$);

q_v is the amount of heat released by internal sources (for example, exothermic heating) to a given moment in time (W/m^3);

c is specific heat ($\text{kJ}/\text{kg}\cdot^{\circ}\text{C}$);

ρ is the density concrete (kg/m^3);

τ is time (day).

Four types of boundary conditions are used to the solution of problems of heat transfer equation (1) as Dirichlet boundary conditions, Neumann boundary conditions, Robin boundary conditions, and Nonlinear, mixed boundary conditions [17].

The solution of problems for determining the temperature regime and the thermally stressed state of concrete massive structures today often obtained using numerical methods (most often the finite element method (FEM)). The value of the temperature of a function at any point in the computational domain in the finite element method is expressed in terms of time and coordinates [18–19].

$$t(x, y, z, \tau) \approx \bar{t} = \sum_{i=1}^n N_i(x, y, z)t_i(\tau) = [N]\{t\}, \quad (2)$$

where N_i is the interpolation function of the shape of the finite element with respect to temperature and coordinates;

n is the number of points in the finite element;

$t_i(\tau)$ is the temperature at each point as a function of time.

In accordance with the Galerkin method, equation (1) is described:

$$\int_V N_i \left[\frac{\partial}{\partial x} \left(k_x \frac{\partial t}{\partial x} \right) + \frac{\partial}{\partial y} \left(k_y \frac{\partial t}{\partial y} \right) + \frac{\partial}{\partial z} \left(k_z \frac{\partial t}{\partial z} \right) \right] dV \{t\} + \int_S h [N] N_i \{t\} dS - \int_S h N_i t_\infty dS + \int_S q N_i dS - \int_V G N_i g V + \int_V \rho c [N] N_i dV \frac{d\{t\}}{d\tau} = 0, \quad (3)$$

where h is the heat transfer coefficient ($W/m^2 \cdot ^\circ C$);

V is volume of element (m^3);

S is the boundary conditions on surface;

q is the heat flux (W/m^3);

G is heat generation within an element (W).

We introduce the notation:

$$[K] = \int_V N_i \left[\frac{\partial}{\partial x} \left(k_x \frac{\partial t}{\partial x} \right) + \frac{\partial}{\partial y} \left(k_y \frac{\partial t}{\partial y} \right) + \frac{\partial}{\partial z} \left(k_z \frac{\partial t}{\partial z} \right) \right] dV + \int_S h [N] N_i dS \quad (4)$$

$$[C] = \int_V \rho c [N] N_i dV, [f] = \int_S h N_i t_\infty dS - \int_S q N_i dS + \int_V G N_i g V,$$

where $[K]$ is conductivity operator;

$[C]$ is capacity operator;

$[f]$ is heat load due to heat hydration.

Then, by introducing equation (4) into equation (3), can be obtained equation (5) as:

$$[C] \frac{d\{t\}}{d\tau} + [K]\{t\} = \{f\}, \quad (5)$$

Applying the method of Galerkin for $t(\tau) = t_i(\tau)N_i + t_j(\tau)N_j$ each element, $N_i = 1 - \frac{\tau}{\Delta\tau}$; $N_j = \frac{\tau}{\Delta\tau}$. At each step, the equation is solved for the time:

$$\left(-\frac{[C]}{2\Delta t} + \frac{[K]}{3} \right) \{t\}_{(n-1)\tau} + \frac{2[K]}{3} \{t\}_{n\tau} + \left(\frac{[C]}{2\Delta t} + \frac{[K]}{6} \right) \{t\}_{(n+1)\tau} = \{f\}, \quad (6)$$

As a result, the solution of equation (6) we obtain the desired temperature field.

To illustrate the process of simulation, a flowchart of the analysis process is shown in Figure 2.

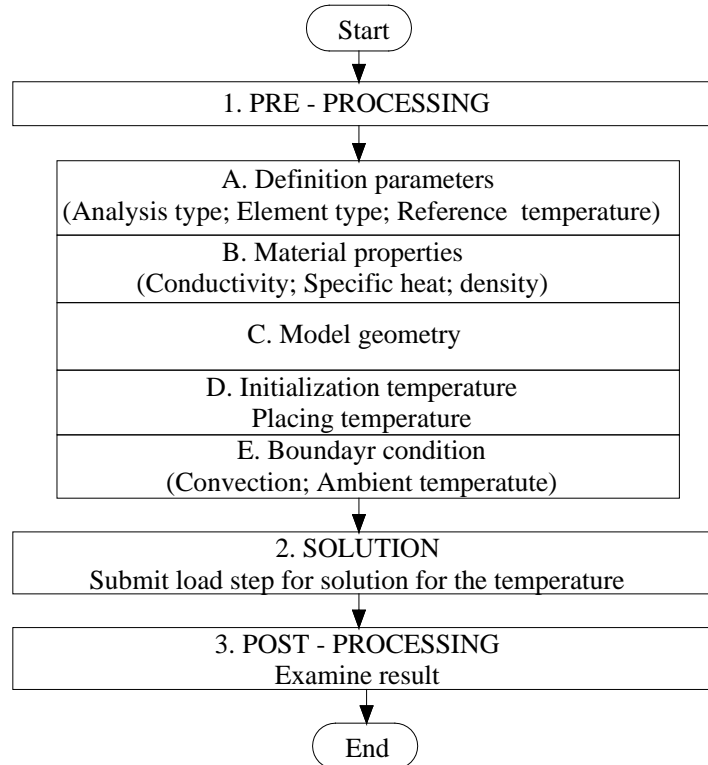


Figure 2. Process analysis of temperature fields, stress in mass concrete block by FEM.

According to the results of studies [20], the ratio between the thermal-stress and temperature in concrete mass is determined by equation (7):

$$\sigma = R \times E(\tau) \times \alpha \times \Delta T, \quad (7)$$

where σ is thermal-stresses (MPa);

R is restraint ($0 < R < 1$), the restraint coefficient which is dependent on the size of the concrete mass and the ratio of elastic module of concrete and foundation: $R \in f(V; E_c/E_f)$ and can be calculated using the computer program Midas Civil;

α is coefficient of thermal expansion ($1/^\circ\text{C}$);

$E(\tau)$ is concrete elasticity modulus (MPa);

ΔT is temperature drop ($^\circ\text{C}$).

The modulus of elasticity $E(\tau)$ of concrete is depend on the age τ , as described by equation (8) [21]:

$$E(\tau) = E_0(1 - e^{-a\tau^b}), \quad (8)$$

where E_0 is concrete elasticity modulus at 28 days age (N/mm^2);

a, b are determined by experiment, $a = 0.4$; $b = 0.34$ [21].

Data for example, according to standards ACI 209.2R-08 "Guide for Modeling and Calculating Shrinkage and Creep in Hardened Concrete». A creep coefficient and an unrestrained shrinkage strain at any time depend on [22]:

- Age of concrete when drying starts, usually taken as the age at the end of moist curing (days);
- Age of concrete at loading (days);
- Curing method;
- Ambient relative humidity expressed as a decimal;
- Volume-surface ratio or average thickness (m);

- Concrete slump (m);
- Fine aggregate percentage (%);
- Cement content (kg/m³);
- Air content of the concrete expressed in percent (%); and
- Cement type.

With the help of software Midas Civil to declare parameters needed to mention creep of concrete at early age days. The creep of mass concrete may be expressed by the following formula (9).

$$J(t, \tau) = \frac{1 + \varphi(t, \tau)}{E(\tau)}, \quad (9)$$

where $J(t, \tau)$ is the creep compliance whose dimension (MPa⁻¹);

$\varphi(t, \tau)$ is the coefficient of creep and is equal to the ratio of creep to elastic strain is shown in Figure 3.

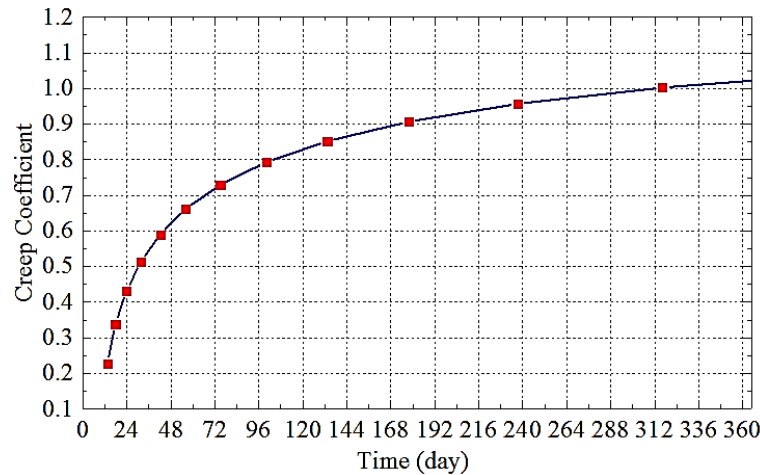


Figure 3. The coefficient of creep at different ages.

Currently, there are many ways to assess the possibility of cracking of mass concrete at an early age. In Russia, in accordance with Russian Construction Norms SP 357.1325800.2017 "Concrete hydraulic structures. Rules of works and acceptance of works" [23], the temperature difference at the center and the outer surface of concrete mass ΔT is allowed no more than (20–25) °C. To describe in more detail the temperature regime of the concrete mass are established on the basis of calculations of temperature fields and the thermal stress state of the concrete mass during construction.

Besides, when the calculated principal tensile stresses exceed the tensile strength of the concrete, cracking is likely to have occurred, which can be assessed by cracking index as described by equation (10) [24].

$$I_{ct} = \frac{f_t(\tau)}{\sigma_t(\tau)}, \quad (10)$$

where I_{ct} is cracking index;

$f_t(\tau)$ is tensile strength;

$\sigma_t(\tau)$ is principal tensile stress.

If $I_{ct} \leq 1$ cracking may occur, and $I_{ct} > 1$ no cracks were formed on the concrete surface.

In this paper, numerical studies of the temperature regime of the mass concrete structure was a pier footing size 6x8x3 m that was placed in the summer weather conditions in Vietnam. There are made and studied the effect of sand layer thickness to control cracked concrete surface. The symmetry of the investigated array was used: a quarter of the concrete block was calculated. The dimensions and the breakdown of the calculation area into the final elements is shown in Figure 4.

The ambient temperature significantly effects on the maximum temperature at the center of the concrete block during the hardening process. This a mass concrete is built with air temperatures are assumed constant

at 28.5 °C, soil temperature is assumed constant at 20 °C and temperature of placed concrete at 30 °C. The mix proportion is shown in Table 1 [25].

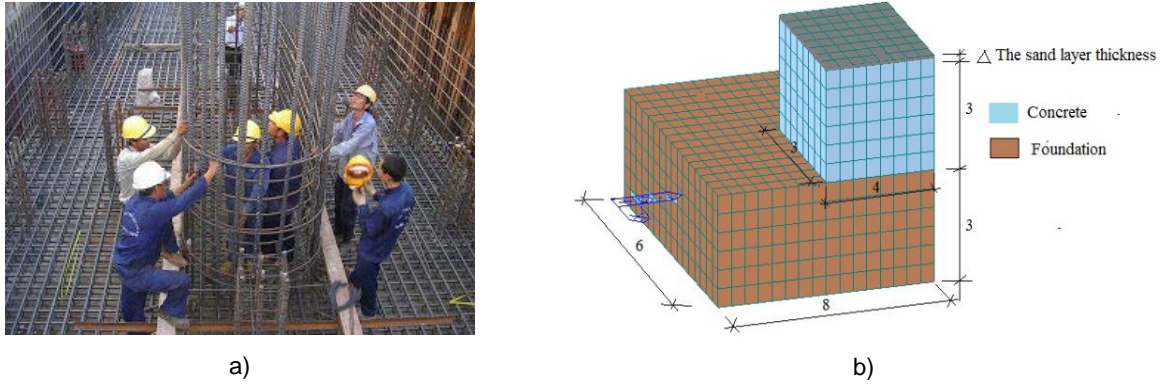


Figure 4. a-A bridge pier footing constructed in Vietnam; b – 3D model for temperature analysis with an insulation layer of sand, unit m.

Table 1. Mix design of concrete.

| Concrete | Ratio Water/ Cement | Materials for 1 m ³ of concrete | | | | |
|----------|------------------------|--|-----------|------------|-----------|-------------------------------|
| | | Cement (kg) | Sand (kg) | Stone (kg) | Water (l) | Additives (super flexible) |
| | 37.5 % | 445 | 829 | 1007 | 167 | (5.12)1.15 % |

The concrete adiabatic temperature is varied by introducing different cement contents. The adiabatic temperature is given by equation (11) [26].

$$t = K(1 - e^{-\alpha\tau}), \tag{11}$$

where t is the adiabatic temperature rise at age τ (°C);

K is the maximum amount of the adiabatic temperature rise from test (°C), $K = 59.6$ °C [26];

α is the reaction factor (°C/h), $\alpha = 1.113$ [26].

Thermal insulators are meant to reduce the rate of heat transfer by conduction, convection, and radiation. The main purpose of surface insulation is not to restrict the temperature rise, but to regulate the rate of temperature drop in order to lower the stress differences due to steep temperature gradients between the concrete surface and the interior [27-28]. This research paper, a bridge pier footing was placed with surrounding surfaces covered by formwork, then inserted by sand around the foundation. Therefore, the authors tend to study the thermal behavior of massive concrete blocks with sand-layer insulation to control the cracks at the surface of massive concrete blocks at the age of early days. The properties of the material elements used in the analysis are presented in Table 2.

Table 2. Material properties in temperature behavior analysis.

| Physical characteristics | Insulation (sand) | Concrete | Foundation |
|--|--------------------|-----------------------|--------------------|
| Thermal conduction coefficient (W/(m.°C)) | 0.27 | 2.90 | 1.96 |
| Specific heat (kJ/kg.°C) | 0.84 | 1.05 | 0.85 |
| Density (kg/m ³) | 1602 | 2400 | 1800 |
| Convection coefficient (W/m ² .°C) | 50 | 13.95 | 14.5 |
| Modulus of elasticity (N/m ²) | 80×10 ⁶ | 3.52×10 ¹⁰ | 2×10 ¹⁰ |
| Thermal expansion coefficient (1/°C) | 1×10 ⁻⁵ | 1×10 ⁻⁵ | 1×10 ⁻⁵ |
| Poisson's ratio | 0.2 | 0.2 | 0.2 |
| Maximum heat of hydration of cement at 28 days (kJ/kg) | – | 320 | – |

3. Results and Discussion

The breakdown of the concrete block and the foundation of the array on the final elements of the three – dimensional model is shown in Figure 2. With the help of the computer program Midas Civil 2017, the maximum temperature in the mass concrete with insulation thickness in differences (0–7) cm as shown in Figure 5.

Temperature distribution in the concrete mass with an insulation thickness of sand 7 cm is shown in Figure 6.

Results analysis: analyzing the results it can be noted that surface insulation by sand does not appreciably increase the maximum concrete temperature. The maximum temperature and temperature difference in the concrete with sand layers of different thickness are shown in Table 3.

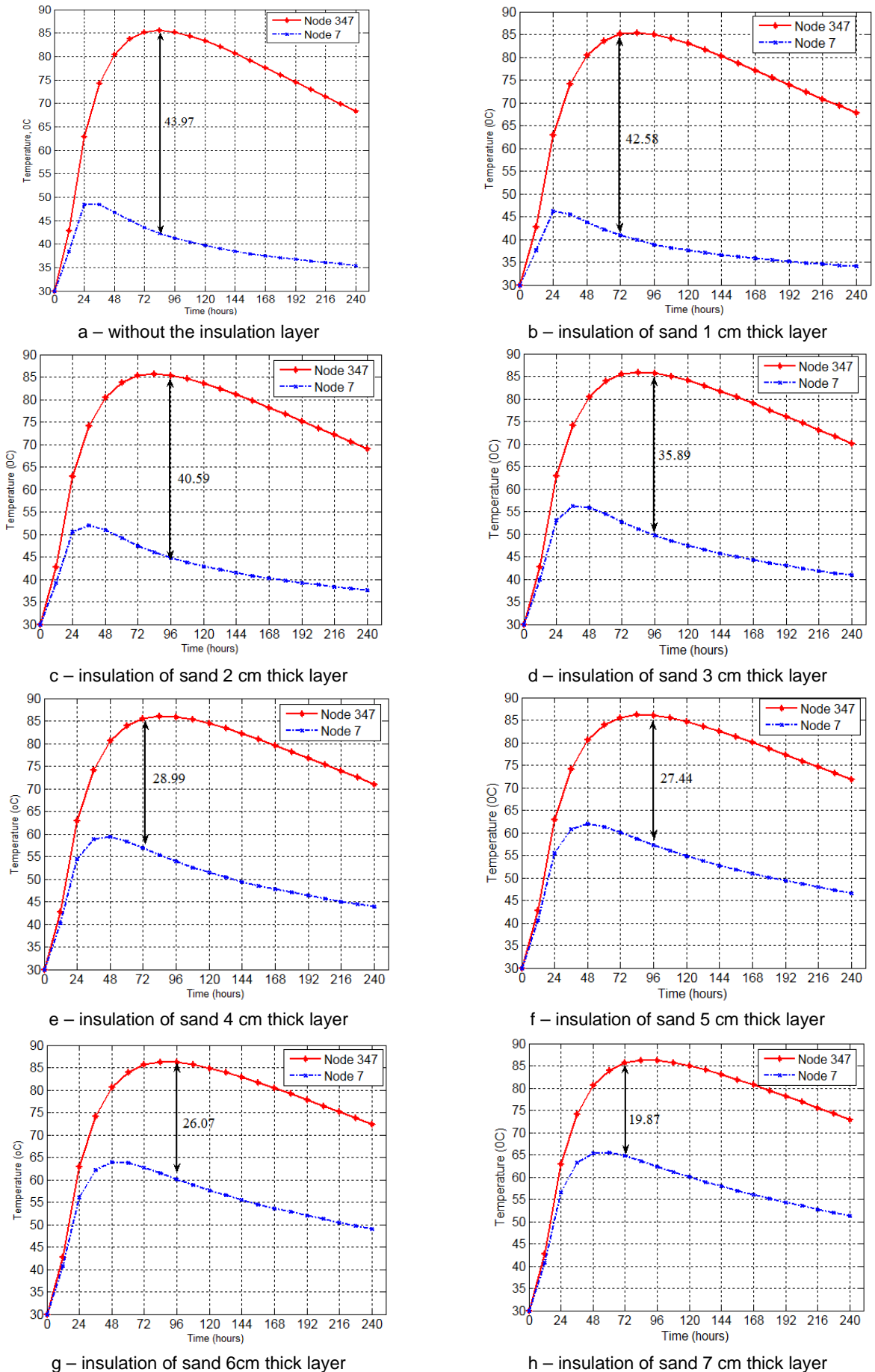


Figure 5. Temperature changes at the center (node 347) and at the surface (node 7) of massive concrete blocks.

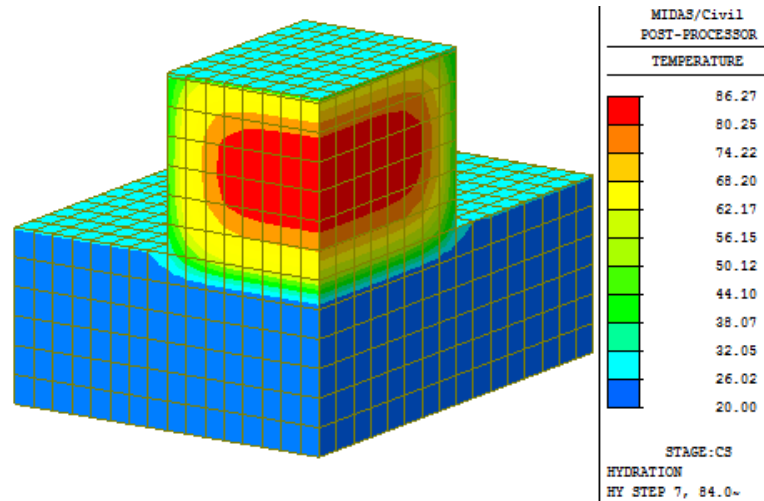


Figure 6. Temperature distribution in the concrete mass through 84 hours after laying.

Table 3. The maximum temperature and temperature difference in the concrete.

| No | Insulation thickness of sand (cm) | | | | | | | |
|----------------------------|-----------------------------------|-------|-------|-------|-------|-------|-------|-------|
| | 0 | 1 | 2 | 3 | 4 | 5 | 6 | 7 |
| Maximum temperature, °C | 85.55 | 85.75 | 85.86 | 85.91 | 86.05 | 86.15 | 86.20 | 86.27 |
| Temperature difference, °C | 43.97 | 42.58 | 40.59 | 35.89 | 28.99 | 27.44 | 26.07 | 19.87 |

Figure 7 shows that the performance of the concrete improves as the insulation of sand thickness increases. Because when increasing the insulation thickness (0 – 7) cm, the temperature gap is reduced.

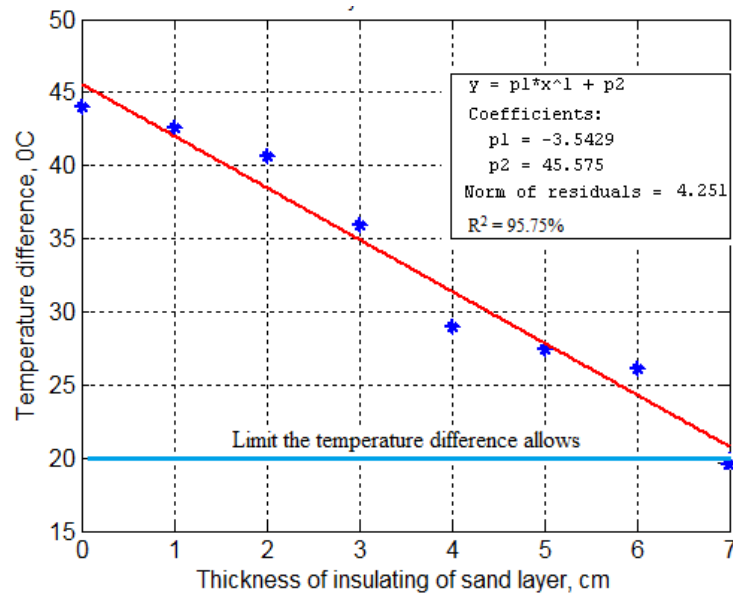


Figure 7. The relationship between the temperature difference and the thickness of the sand insulation.

Surveying range of sand thickness from 0 to 7 cm show the relation among them, and the temperature difference in the concrete mass as a function is shown in Figure 7. The correlations from the linear regressions of temperature difference vs the thickness of the sand insulation ($y = -3.5x + 46$) R -value is $R^2 = 95.75\%$, respectively. Therefore, it has a very good relationship.

It is worth noting that in the case of sand with a thickness of 7 cm the temperature difference between the inside and the surface not exceeds 20 °C. Besides, Figure 8 shows the stress development of the two feature points (at the center – node 347 and at the surface – node 7) with two cases: case 1 – without the insulation, case 2 – insulation of sand 7 cm in the concrete mass.

Figure 8 shows that, in the case of the concrete mass without the insulation layer, at the node 7 of the investigated mass to 168 hours of hardening the concrete, the tensile principal stress value exceeds its permissible value, leading to the formation of cracks on the surface of the concrete mass. Whereas, In the

case of a concrete mass with insulation of sand 7 cm, the tensile principal stress was less than the ultimate tensile principal strength of concrete, which avoids able in forming cracks.

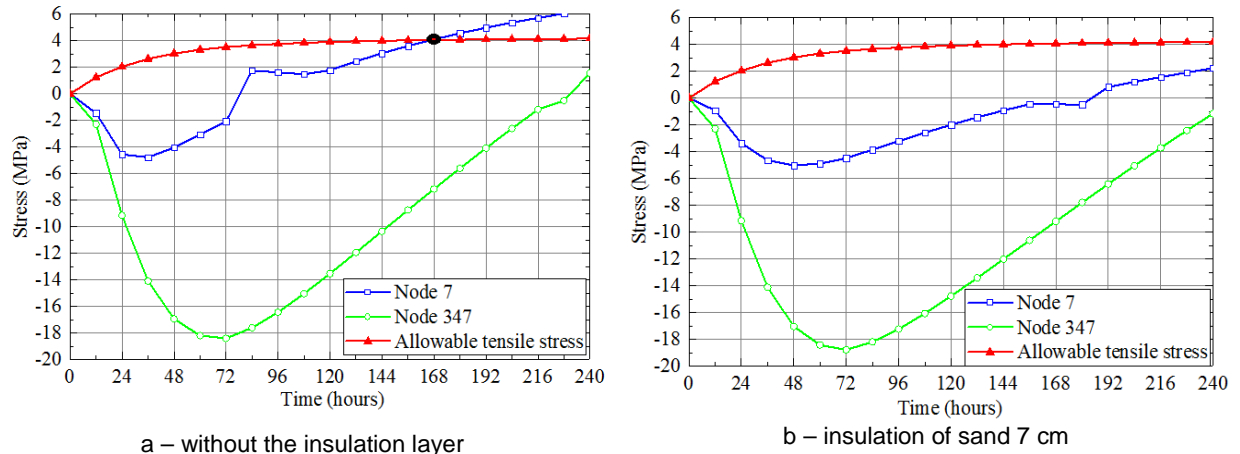


Figure 8. The principal stresses development of the two points (node 347 and node 7) in the concrete mass, a – without the insulation layer; b – insulation of sand 7 cm.

4. Conclusions

Based on the results of the study lead to the following conclusions:

1. The program Midas Civil 2017 is quite an effective tool for calculating the temperature regime and the thermal stress of concrete structures during their construction.
2. Although increasing the sand-layer insulation thickness, its effects on the maximum temperature differences between the surface and the center of the mass concrete block are not considerable.
3. The thickness of the insulation is inversely proportional to the maximum temperature difference between the center and the surface of the mass concrete. The largest temperature gap is 43.97 °C in the case without insulation sand-layer, while those gaps for (0–7) cm insulation thickness are gradual decrease. In the case of sand-layer insulation have a thickness of 7 cm –the temperature gap is 19.87 °C. In addition, the relationship between the temperature differences and the thickness of the sand insulation is given by the formula $y = -3.5x + 46$ with precision $R^2 = 95.75\%$.
4. In case one the development of cracks may happen to the mass concrete block when the largest temperature gap is 43.97 °C and it exceeds the maximum allowable temperature difference which is 20 °C. By contrast, this phenomenon will not happen with the preservation of insulation have a thickness of 7 cm when the maximum temperature gap is lower than the limitation. As a result, this effective technique should be used to prevent cracks of the mass concrete block at an early age.
5. And future work: It is necessary to study theory in combination with the experiment to accurately evaluate the effectiveness of using insulating sand layer, avoid cracking at the face in the concrete mass at the early age. In addition, it is possible to produce sand insulation in modules. Those modules are convenient not only for construction process but also for preservation and removal process, which is applied to solve a variety of problems, such as concrete block shape, rainy and windy weather conditions.

References

1. ACI Committee 207. 207.1R-05 Guide to Mass Concrete, American Concrete Institute. 2005. Farmington Hills, Mich.
2. Tian, Y., Jin, X., Jin, N. Thermal cracking analysis of concrete with cement hydration model and equivalent age method. Computers and Concrete. 2013. Vol. 11. No. 4. Pp. 271-289. DOI: 10.12989/cac.2013.11.4.271
3. Zhang, C., Zhou, W., Ma, G., Hu, C., Li, S. A meso-scale approach to modeling thermal cracking of concrete induced by water-cooling pipes. Computers and Concrete. 2015. Vol. 15. No. 4. Pp. 485-501. DOI: 10.12989/cac.2015.15.4.485
4. Fangyuan, L., Yin, S. Full-scale test of the hydration heat and the curing method of the wet joints of a precast segmental pier of a bridge. European Journal of Environmental and Civil Engineering. 2015. Vol. 29. No. 3. Pp.348–370 [Online]. URL: <https://doi.org/10.1080/19648189.2015.1119063>
5. Song, S.-J., Yoo, S.-G., Park, J.-W., Kim, E.-K. A study for control of thermal cracking by heat of hydration in subway concrete box structure. Journal of the Korean Society for Railway. 2009. Vol. 12. Pp. 1024–1029.
6. Struchkova, A.Y., Barabanshchikov, Yu.G., Semenov, K.S., Shaibakova, A.A. Heat dissipation of cement and calculation of crack resistance of concrete massifs. Magazine of Civil Engineering. 2018. 78(2). Pp. 128–135. DOI: 10.18720/MCE.78.10
7. Aurich, M., Filho, A.C., Bittencourt, T.N., Shah, S.P. Finite element analysis of concrete cracking at early age. Structural Engineering and Mechanics. 2011. Vol. 37. No. 5. Pp. 459–473 [Online]. URL: <https://doi.org/10.12989/sem.2011.37.5.459>

8. Bushmanova, A.V., Videnkov, N.V., Semenov, K.V., Barabanshchikov, Yu.G., Dernakova, A.V., Korovina, V.K. The thermo-stressed state in massive concrete structures. Magazine of Civil Engineering. 2017. 71(3). Pp. 51–60. DOI: 10.18720/MCE.71.6
9. Bushmanova, A.V., Barabanshchikov, Yu.G., Semenov, K.V., Struchkova, A.Ya., Manovitsky, S.S. Thermal cracking resistance in massive foundation slabs in the building period. Magazine of Civil Engineering. 2017. 76(8). Pp. 193–200. DOI: 10.18720/MCE.76.17
10. Zhang, X., Li, S., Li, Y., Ge, Y., Li, H. Effect of superficial insulation on roller-compacted concrete dams in cold regions. Advances in Engineering Software. 2018. Vol. 42. No. 11. Pp. 939–943. DOI:10.1016/j.advengsoft.2011.06.004
11. Tu, D.A., Adrian, M.L., Mang, T., Anh, P.N. Importance of insulation at the bottom of mass concrete placed on soil with high groundwater. Transportation Research Record Journal of the Transportation Research Board. 2013. Vol. 2342. No. 1. Pp. 113–120.
12. Bamforth P.B. Early-age thermal crack control in concrete. 2017. London.
13. Lam, T.V., Chuc, N.T., Boris, B., Michael, J.B. Composition and early-age temperature regime in a massive concrete foundation. 2018. MATEC Web of Confer. Vol.196. 8p. [Online]. URL: <https://doi.org/10.1051/mateconf/201819604017>
14. Patil, A. Heat of hydration in the placement of mass concrete. International Journal of Engineering and Advanced Technology (IJEAT). 2015. Vol. 4. No. 3. 4p.
15. Lee, M.H., Chae, Y.S., Khil, B.S., Yun, H.D. Influence of casting temperature on the heat of hydration in mass concrete foundation with ternary cement. Applied Mechanics and Materials. 2014. Vol. 525. Pp. 478–481. DOI: 10.4028/www.scientific.net/AMM.525.478
16. Li, B., Wang, Z., Jiang, Y., Zhu, Z. Temperature control and crack prevention during construction in steep slope dams and stilling basins in high-altitude areas. Advances in Mechanical Engineering. 2018. Vol. 10. No. 1. 15p. DOI: 10.1177/1687814017752480
17. Klemczak, B., Knoppik-Wrobel, A. Early age thermal and shrinkage cracks in concrete structures-Description of the problem. Architecture Civil Engineering Environment. 2011. Vol. 3. Pp. 55–70.
18. Van Lam, T., Nguyen, C.C., Bulgakov, B.I., Anh, P.N. Composition calculation and cracking estimation of concrete at early ages. Magazine of Civil Engineering. 2018. 82(6). Pp. 136–148. DOI: 10.18720/MCE.82.13
19. Akin, J.E. Finite element for analysis and design. Texas, USA. 1994. 548p.
20. Abeka, H., Agyeman, S., Adom-asamoah, M., Hussain, R.R. Thermal effect of mass concrete structures in the tropics: experimental, modelling and parametric studies. Journal Cogent Engineering. 2017. Vol. 4. No. 1. Pp. 185–192.
21. Zhu, B. Thermal stresses and temperature control of mass concrete. Published by Elsevier Inc. 2014. 497p.
22. ACI 209.2R-08. Guide for modeling and calculating shrinkage and creep in hardened concrete. American Concrete Institute. 2008. 48p.
23. SP 357.1325800.2017. Konstruktsii betonnyye gidrotekhnicheskikh sooruzheniy [Concrete constructions hydraulic structures. Rules of production and acceptance of work].
24. Noorzaei, J., Bayagoob, K.H., Thanoon, W.A., Jaafar, M.S. Thermal and stress analysis of kintarcc dam. Journal Engineering Structures. 2006.No. 28. Pp. 1795–1802.
25. ACI 318-2005. Building Code Requirements for Structural Concrete. American Concrete Institute, Farmington Hills, Mich. 2005. 31 p.
26. Khoa, H.N, Cong, V.C. Analyzing temperature field and thermal stress in massive concrete by finite element method. Journal of Science and Technology building. 2012. No. 14(12). Pp. 17–27.
27. Chuc, N.T., Lam, T.V., Bulgakov, B.I. Designing the composition of concrete with mineral additives and assessment of the possibility of cracking in cement-concrete pavement. Materials Science Forum. 2018. Vol. 931. Pp. 667–673[Online]. URL: <https://doi.org/10.4028/www.scientific.net/MSF.931.667>
28. Korotchenko, I.A., Ivanov, E.N., Manovitsky, S.S., Borisova, V.A., Semenov, K.V., Barabanshchikov, Yu.G. Deformation of concrete creep in the thermal stress state calculation of massive concrete and reinforced concrete structures Magazine of Civil Engineering. 2017. 69(1). Pp. 56–63. DOI: 10.18720/MCE.69.5

Contacts:

*Trong Chuc Nguyen, +7(966)3319199; ntchuc.mta198@gmail.com
Xuan Bach Luu, +84979940455; xuanbachmta@gmail.com*

© Nguyen, C.T., Luu, X.B., 2019



ПОЛИТЕХ
Санкт-Петербургский
политехнический университет
Петра Великого

Инженерно-строительный институт
Центр дополнительных профессиональных программ

195251, г. Санкт-Петербург, Политехническая ул., 29,
тел/факс: 552-94-60, www.stroikursi.spbstu.ru,
stroikursi@mail.ru

Приглашает специалистов проектных и строительных организаций,
не имеющих базового профильного высшего образования
на курсы профессиональной переподготовки (от 500 часов)
по направлению «Строительство» по программам:

П-01 «Промышленное и гражданское строительство»

Программа включает учебные разделы:

- Основы строительного дела
- Инженерное оборудование зданий и сооружений
- Технология и контроль качества строительства
- Основы проектирования зданий и сооружений
- Автоматизация проектных работ с использованием AutoCAD
- Автоматизация сметного дела в строительстве
- Управление строительной организацией
- Управление инвестиционно-строительными проектами. Выполнение функций технического заказчика

П-02 «Экономика и управление в строительстве»

Программа включает учебные разделы:

- Основы строительного дела
- Инженерное оборудование зданий и сооружений
- Технология и контроль качества строительства
- Управление инвестиционно-строительными проектами. Выполнение функций технического заказчика и генерального подрядчика
- Управление строительной организацией
- Экономика и ценообразование в строительстве
- Управление строительной организацией
- Организация, управление и планирование в строительстве
- Автоматизация сметного дела в строительстве

П-03 «Инженерные системы зданий и сооружений»

Программа включает учебные разделы:

- Основы механики жидкости и газа
- Инженерное оборудование зданий и сооружений
- Проектирование, монтаж и эксплуатация систем вентиляции и кондиционирования
- Проектирование, монтаж и эксплуатация систем отопления и теплоснабжения
- Проектирование, монтаж и эксплуатация систем водоснабжения и водоотведения
- Автоматизация проектных работ с использованием AutoCAD
- Электроснабжение и электрооборудование объектов

П-04 «Проектирование и конструирование зданий и сооружений»

Программа включает учебные разделы:

- Основы сопротивления материалов и механики стержневых систем
- Проектирование и расчет оснований и фундаментов зданий и сооружений
- Проектирование и расчет железобетонных конструкций
- Проектирование и расчет металлических конструкций
- Проектирование зданий и сооружений с использованием AutoCAD
- Расчет строительных конструкций с использованием SCAD Office

П-05 «Контроль качества строительства»

Программа включает учебные разделы:

- Основы строительного дела
- Инженерное оборудование зданий и сооружений
- Технология и контроль качества строительства
- Проектирование и расчет железобетонных конструкций
- Проектирование и расчет металлических конструкций
- Обследование строительных конструкций зданий и сооружений
- Выполнение функций технического заказчика и генерального подрядчика

По окончании курса слушателю выдается диплом о профессиональной переподготовке
установленного образца, дающий право на ведение профессиональной деятельности

